ABSTRACT

HUANG, JINGJING. Measurement and Quasi-classical Modeling of Spin Density Evolution and Spin Correlation in a Fermi Gas. (Under the direction of John Thomas).

In this dissertation, I present a systematic experimental study of spin density evolution and spin correlation in a weakly interacting ^{6}Li Fermi gas. The cloud is nearly collisionless and behaves as a large spin lattice in energy space with tunable, reversible Hamiltonian and effective long-range interactions, providing a powerful platform to study classical and quantum dynamics in a quasi-continuous system.

The experiments are implemented by manipulating radiofrequency pulse sequences and time-dependent scattering lengths. By inverting the sign of the Hamiltonian, I developed a model-independent method to find the zero-crossing magnetic field, B_0, where the scattering length vanishes. An accurately measured B_0 is essential for a proper Hamiltonian reversal, which is widely used in dynamical decoupling pulse sequences for decoherence and correlation studies.

I used a perturbed quantum rewinding sequence based on Hamiltonian reversal to elucidate the effects of RF detunings on the system and measurements to test a quasi-classical spin model by comparing it to the measurements. The model reported in this dissertation is in quantitative agreement with measurements of the ensemble-averaged energy-resolved spin density in the experiments for short evolution times, confirming that this system is evolving classically. However, the model does not predict the observed behavior for long evolution times, suggesting multi-mode behavior that will be investigated in future experiments.

To measure multi-shot averaged energy-space transverse spin correlations, I developed new data selection methods based on the evaluation of product operators. I applied these methods to observe the flow of correlations in energy space, revealed the connection between the evolution of the macroscopic magnetization of a system and the localization or spread behavior of correlations. I highlighted energy-space correlation as a new observable in quantum phase transition studies, decoding the microscopic features of spin dynamics that are hidden in macroscopic measurements.

Measurement and Quasi-classical Modeling of Spin Density Evolution and Spin Correlation in a Fermi Gas

by
Jingjing Huang

A dissertation submitted to the Graduate Faculty of
North Carolina State University
in partial fulfillment of the
requirements for the degree of
Doctor of Philosophy

Physics

Raleigh, North Carolina
2023

APPROVED BY:

Ilya Arakelyan	Kenan Gundogdu
Lubos Mitas	Thomas Theis

John Thomas
Chair of Advisory Committee

BIOGRAPHY

Jingjing Huang was born in China in 1995. She attended University at Albany and received her B.S. degrees in Physics and Mathematics in 2018. She attended Tufts University and obtained Master's degree in physics in 2020. In the same summer, she started working in Prof. John E. Thomas's research group at NC State University. Her research at NCSU focused on engineering the Hamiltonian of degenerate quantum gas and studying the evolution of spin density and the emergence of spin correlations in a many-body spin system. She received her Ph.D. in physics in 2023.

ACKNOWLEDGEMENTS

The work presented in this dissertation was funded by the Air Force Office of Scientific Research (FA9550-22-1-0329), the National Science Foundation (PHY-2006234 and PHY-2307107), NC State University Provost's Doctoral Fellowship, Provost Doctoral Supplement and Sayers Fellowship (the last two are provided by physics department).

I am grateful to the principal investigator Prof. John E. Thomas for allowing me to conduct research in his laboratories and for providing all the help for my career development. I would like to thank the members of my dissertation committee: Prof. Kenan Gundogdu, Prof. Lubos Mitas, and Prof. Thomas Theis, for their useful comments and inspiring questions. Thanks should also go to my colleagues, Xiang Li, Saeed Pegahan, Camen A. Royse, Xin Wang, and De-Chao Zhang. I also very much appreciate the graduate program coordinator Bennett Rhonda for helping me with all the paperwork.

I thank my friend Ilya Arakelyan, who was helping and advising me during these years. Just as he often says, nothing is easy, it is always painful; Ну и что ж! Вы — успокоительное сознание прочного убежища, неизменной защиты, бессмертного покровительства внутри меня. Lastly, I thank myself for self-possession and self-restraint.

CONTENTS

LIST OF TABLES

LIST OF FIGURES

CHAPTER

1

INTRODUCTION

Weakly interacting Fermi gases provide a powerful platform to study the out-of-equilibrium dynamics and critical dynamics across quantum phase transitions. Because of the low energy property of ultracold Fermi gases, two-body interactions are dominated by s-wave scattering. Hence by preparing a sample containing atoms with two opposite spins, the s-wave interaction is allowed and the interaction is uniquely described by the s-wave scattering length. Using a Feshbach resonance to tune to the weakly interacting regime, close to the zero-crossing magnetic field where the scattering length vanishes, both strength and sign of interaction can be controlled by tuning the magnetic field.

The trapped cloud behaves as a spin-lattice in energy-space with effective long-range interactions (Du et al. 2008, 2009; Ebling et al. 2011; Pegahan et al. 2019; Piéchon et al. 2009; Natu and Mueller 2009; Deutsch et al. 2010; Smale et al. 2019; Koller et al. 2016; Gärttner et al. 2017; Eisert et al. 2015). For the scattering lengths of several bohr that are used throughout this dissertation, the collision rate is extremely small. As an example, at a median scattering length adopted for the study displayed in this dissertation, $5.19\,a_0$, the classical collision rate is $\gamma_c \propto |a|^2 \approx 0.003\,/s$ (Gehm et al. 2003), which means that over evolution times on the order of seconds, the probability of a collision is negligible. Therefore, both the energy and the energy state of a single particle are conserved over the experimental cycle and each fixed energy is considered as an energy lattice site. Thus, a weakly interacting Fermi gas containing $N \simeq 10^5$

atoms with a tunable, reversible Hamiltonian enables the study of coherence, entanglement, and correlation in time-reversible many-body synthetic lattice (Hazzard and Gadway 2023), broadly impacting the understanding of quantum measurement and information processing (Lewis-Swan et al. 2019; Eisert et al. 2015; Kaufman and et al. 2016).

The experiments presented in this dissertation are performed in degenerate Fermi gases, consisting of 6.2×10^4 ^{6}Li atoms. The cloud is confined in an optical trap and cooled to temperature $T\approx0.3\,T_F$, where the Fermi temperature $T_F\approx0.73\,\mu$K. The ratio between radial and axial trap frequencies is ~27, allowing a quasi-1D approximation during modeling. A superposition of the two lowest hyperfine-Zeeman states, which are denoted by $|1\rangle\equiv|\uparrow_z\rangle$ and $|2\rangle\equiv|\downarrow_z\rangle$, is prepared by a coherent RF (radiofrequency) pulse at the beginning of experimental cycle.

The collision rate is controlled to be negligible during each cycle by tuning the bias magnetic field B to provide a sufficiently small scattering length $a(B)$. Therefore, in such a weakly interacting regime, the energy and the energy state of each particle are conserved, allowing us to simulate the system as a 1D lattice in energy space. Each lattice site "i" represents the i^{th} harmonic oscillator state along the axial direction of the sample, with an energy $E_i=(n_i+1/2)\,h\,\nu_x$ and dimensionless collective spin vector $\vec{s}(E_i)\equiv\vec{s}_i$. This synthetic lattice can be described by a Heisenberg Hamiltonian:

$$\frac{H(a)}{\hbar}=\sum_{i,j\neq i}g_{ij}\,\vec{s}_i\cdot\vec{s}_j+\sum_i\Omega' E_i\,s_{zi}+\Delta(t)S_z. \tag{1.1}$$

The first term in the Hamiltonian above is the site-to-site interaction, proportional to the s-wave scattering length a and to the overlap of the harmonic oscillator probability densities for colliding atoms. In a WKB approximation, $g_{ij}\propto1/\sqrt{|E_i-E_j|}$, which is an effective long-range interaction in the energy-space lattice. For a zero temperature Fermi gas, the average interaction energy (in rad/s) is $\bar{g}=6.8\,n_0\hbar a/m$, where n_0 is the peak density. In our system, the average $g_{ij}(a)$ is $\bar{g}(a=5.2\,a_0)\approx1.7$ Hz $\times2\pi$.

The second term in the Hamiltonian is an effective site-dependent Zeeman energy, arising from the quadratic spatial variation of the bias magnetic field along x, which produces a spin-dependent harmonic potential. As $\omega_r/\omega_x=26.6$, the corresponding effect on the radial motion is negligible, enabling a 1D approximation, where all atoms at site i have the same Zeeman energy. $\Omega'=-\delta\omega_x/(\hbar\omega_x)$, with $\delta\omega_x/2\pi=14.21$ mHz. For the mean energy $\bar{E}_x\simeq k_B T_F/4$, $\Omega'\,\bar{E}_x/2\pi\simeq2.0$ Hz. The statistical standard deviation of $\Omega'\,E_x$ is calculated to be $\sigma_{\Omega_z}\approx1.4$ Hz and determines the spread in the spin-precession rates.

The last term in the Hamiltonian arises from the time-dependent global detuning $\Delta(t)$, which plays a central role in the analysis of the data. Here, $S_z=\sum_i s_{zi}$. Fluctuations in the bias magnetic field and magnetic tuning of the scattering length cause $\Delta(t)$ to change at 5 kHz/G

for $|1\rangle$-$|2\rangle$ superposition states.

The ratio of the first and second terms in Eq. 1.1 determines the behavior of the system during evolution. For this reason, a dimensionless interaction strength is defined: $\zeta \equiv \bar{g}(a)/(\sqrt{2}\sigma_{\Omega_z})$. Here, larger ζ represents a stronger mean-field interaction, and for small ζ, the system is dominated by the spread in Zeeman precession.

With the Hamiltonian shown in Eq. 1.1, Heisenberg's equation for spin operator $\dot{\vec{s}}_i = i/\hbar[\hat{H}, \vec{s}_i]$ has the form:

$$\dot{\vec{s}}_i = [\vec{\Omega}' E_i + \Delta(t)] \times \vec{s}_i + \sum_{j \neq i} g_{ij} \vec{s}_j \times \vec{s}_i. \tag{1.2}$$

In a quasi-classical approximation, $\vec{s}$ is treated as a classical vector, ignoring the quantum correlation in $\vec{s} \times \vec{s}$ term. Solving this equation of motion Eq. 1.2, the emergence of spin waves is predicted. The formation of a spin wave leads to spin segregation phenomenon: for positive scattering length, the local maximum in spatial density of the spin state with higher energy moves outward and the local maximum in spatial density of the spin state with lower energy remains at the center of the trap. This effect is depicted in Fig. 1.1 at different evolution times. The top two rows with yellow background color are the absorption images of two states measured at different times relative to the initial coherent excitation RF pulse. Immediately after this pulse, two spin states have identical images. After a 200 ms evolution, one spin state moves toward the center of the magnetic bowl while the other moves toward the edge. Then at 440 and 640 ms evolution time, the two spins move in different directions. As shown in the images, two spins are spatially segregated while the system evolves. The bottom row is obtained by subtracting the absorption images of two spin states and integrating them over radial direction. The normalized result is directly proportional to s_z, the z component of the collective spin vector.

The degree of segregation is quantified by measuring the value of s_z at center of sample, namely, central spin density. Understanding the spin segregation behavior is essential for the study of collective quantum dynamics and correlated spin current in this system.

Spin waves as shown in Fig. 1.1 have been observed and explained by several models (Ebling et al. 2011; Piéchon et al. 2009; Natu and Mueller 2009; Deutsch et al. 2010; Koller et al. 2016; Pegahan et al. 2019). Various simplifying assumptions have been employed to model the large spin lattice systems. For example, an all-to-all coupling treatment is adopted to approximate the spin waves in Dicke basis to the first order of perturbation theory, yielding a semi-quantitative agreement with the measurements (Koller et al. 2016). More precise agreement is obtained by a 1D quasi-classical spin evolution model that uses the exact energy-dependent couplings (Pegahan et al. 2019; Huang et al. 2023).

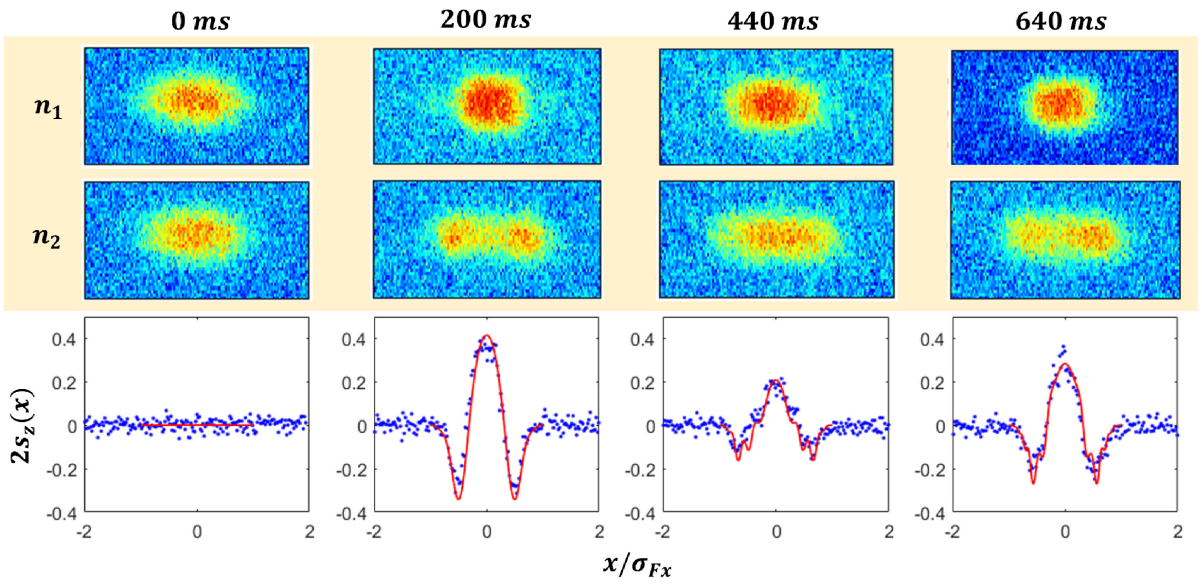

Figure 1.1: Top two rows with yellow background are the absorption images of states 1 and 2 taken at different evolution times relative to the initial coherent excitation pulse. The bottom row is the axial profile of the collective spin vector s_z. Blue dots are from single shot data and the red curve is predicted by the equation of motion Eq. 1.2, which will be derived in detail in Ch. 3.

1.1 Significance of the current work

This dissertation mainly consists of two facets of the spin dynamics study in a weakly interacting Fermi gas, which has a tunable, reversible Hamiltonian and effective long-range interactions. First, I present a precise, systematic test of a modified quasi-classical spin model of this large spin-lattice in energy space with three experiments: spin segregation, quantum rewinding, and perturbed quantum rewinding (Huang et al. 2023). Second, I develop a new data analysis method to observe the energy-resolved, ensemble-averaged transverse spin correlation at a microscopic level, enabling a deeper look into the signatures of macroscopic "phase transitions" and the origins of macroscopic magnetization (Huang and Thomas 2023).

1.1.1 Tests of the quasi-classical spin model

Classical and quantum dynamics in large spin systems is currently of great interest (Schubert et al. 2021; Das et al. 2019; Lakshmanan et al. 1976; Ball 2021). In many cases, it is not clear if the spin system would evolve classically or quantum mechanically. The 1D quasi-classical spin model was found to be in good agreement with spin-density profiles measured for the evolution

of an initially x-polarized spin sample with limited evolution time. However, unexplained decay of the spin-wave amplitude was observed for long time evolution. It also appeared that this model failed to explain out-of-time order correlation measurements, where an RF pulse rotates the entire spin system by an angle ϕ_x about the x axis as a perturbation in between forward and backward evolutions in a quantum rewinding process. In a quantum picture, the ϕ_x rotation changes the relative phases of the superposed total angular momentum states that describe the system, i.e., $|S, M_x\rangle \rightarrow e^{-iM_x\phi_x}|S, M_x\rangle$ for each state, leading to ϕ_x-dependent coherence amplitude between states differing in M_x (Gärttner et al. 2017, 2018; Pegahan et al. 2021). To fit the data, a scattering length of ≈ 2.5 times the measured value was needed in the previous model adopted in Ref. Pegahan et al. (2021). These disagreements question the adequacy of the quasi-classical model.

In this dissertation, I present a study to understand the capability of a modified quasi-classical spin evolution model for describing a many-body spin system and propose possible missing pieces of this model.

I performed my first experiments as an attempt to explain the unpredicted decay in spin current amplitude at long evolution time. By comparing the distribution of central spin density measured from experiments with that predicted by the quasi-classical model, I conducted the first statistical study on this topic with a large sample size. In Ref. (Pegahan et al. 2019), it was believed that this decay arises from averaging over a number of shots with finite variation in initial conditions, cloud size and atom number, which affects the evolution rate. However, the result from my statistical study rejects this hypothesis: it suggests the existence of multi-modes in the experimental system which is not predicted in the mean-field model. The missing piece incapacitates the model from predicting system behavior at a long evolution time. This experiment also sets a benchmark of the time range where the model is still valid.

In my study, the unperturbed and perturbed quantum rewinding experiments are utilized to test a quasi-classical spin evolution model. Before implementing the perturbed quantum rewinding experiment, the unperturbed one is performed in advance to prove that the system is able to be reversed properly without model-dependent fits. The Hamiltonian reversal experiment, which is an unperturbed quantum rewinding experiment, inverts the sign of Hamiltonian of the system using a combination of a radiofrequency (RF) π pulse and magnetic field sweep to flip the scattering length from a to $-a$ after a forward evolution time τ. In the Hamiltonian reversal experiment, I examine the reversal behavior of the system at different experimental conditions (scattering lengths and evolution times) and find possible multi-mode explanations for the failing mechanism of the model in describing evolution at long times. In these experiments, it is essential to carefully calibrate the bias magnetic field B_0 at which the s-wave scattering length vanishes. I precisely find B_0 by quantifying the reversal results using

different magnetic fields. This method is independent of fitting models and less sensitive to the initial conditions. My measurements yield a result of $B_0 = 527.15$ G, which is 30 mG lower than reported previously (Pegahan et al. 2019). With the updated zero-crossing magnetic field value, the Hamiltonian reversal protocol is realized properly. Fig. 1.2 illustrates the agreement in normalized spatial profiles measured from the sample for forward and backward evolution. This set of data is taken at $8.05\,a_0$, with Hamiltonian reversed at $\tau_f = 280$ ms.

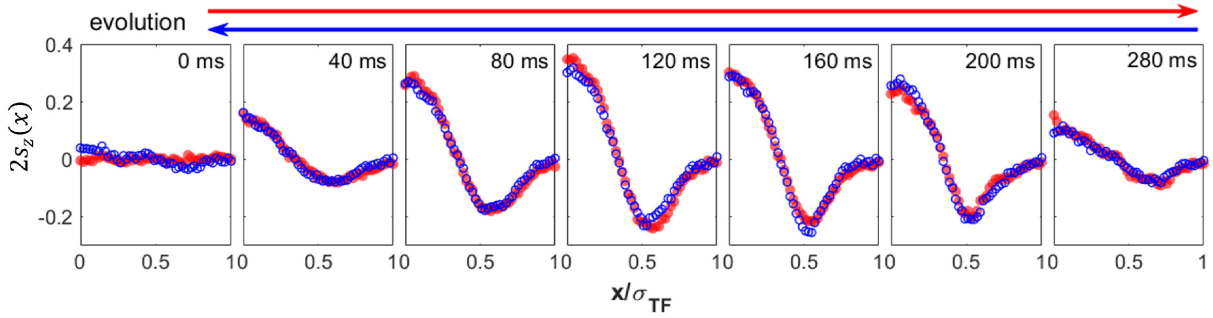

Figure 1.2: Comparing forward (red) and backward (blue) evolution s_z spatial profiles at different evolution times. This set of data is obtained from an experiment performed at $8.05\,a_0$ and Hamiltonian reversed at 280 ms.

With the understanding of system reversibility using different experimental parameters, I conduct the perturbed quantum rewinding experiments with conditions that give reasonably good Hamiltonian reversal results. Previously, a major discrepancy between the model and data was observed in Ref. Pegahan et al. (2021). The model adopted in his work assumed a controllable RF detuning and required a fitting scattering length to be 2.5 times the measured value to make this model fit the data. In contrast, I modify the model such that it contains the randomness in RF detunings properly. The modified model is able to quantitatively fit the data obtained from my perturbed quantum rewinding experiments using measured experimental parameters as shown in Fig. 1.3.

In this study of perturbed quantum rewinding, ensemble-averaged energy-space operators are measured in a single shot, avoiding multi-shot averages with imperfectly controlled experimental parameters. This method enables quantitative comparison between a quasi-classical spin vector model and single-shot data, which suggests that the system behaves classically. The model reported here points the way to new multi-shot average correlation measurement methods that are insensitive to fluctuations in the experimental parameters, avoiding probabilistic methods in data analysis (Smale et al. 2019) and not highly dependent on fitting model. The new method is applied to measure the transverse spin correlations, which has been challenging

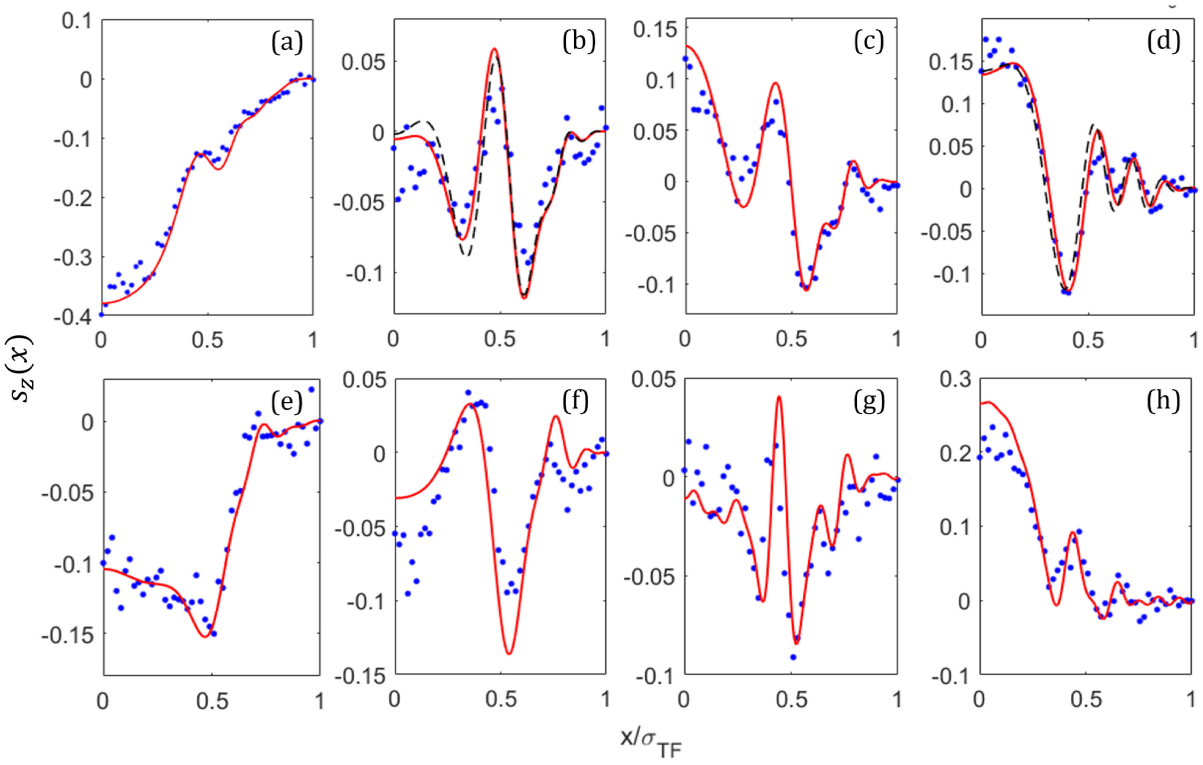

Figure 1.3: Single-shot spin density spatial profiles for perturbed quantum rewinding experiment with different perturbation pulses ϕ_x. (a,b,c,d) measured scattering length $a = 5.19\,a_0$, $\tau = 200$ ms; (e,f) measured scattering length $a = 8.05\,a_0$, $\tau = 200$ ms; (g,h) measured scattering length $a = 5.19\,a_0$, $\tau = 400$ ms. Blue dots are measured spatial profiles. Red curves are predicted by the modified quasi-classical model using measured scattering length. Black-dashed curves in (b) and (d) are generated by the model adopted in Ref. Pegahan et al. (2021) using about two times the measured scattering length.

historically because of the accumulated RF phase problem.

1.1.2 Measurements of transverse spin correlation

The collective spin dynamics encoded in the transverse spin correlation are incredibly rich, and play a central role in spin-lattice models such as Heisenberg models of quantum magnetism (Auerbach 1994), Anderson pseudo-spin models of superconductivity (Anderson 1958), and Richardson-Gaudin models of pairing (Dukelsky et al. 2004). These models have been simulated in discrete systems, including ion traps (Richerme et al. 2014; Joshi et al. 2020; Gärttner et al. 2017), quantum gas microscopes (Cheuk et al. 2015), and cavity-QED experiments (Swingle et al. 2016), which achieve single-site resolution. In contrast, in this thesis, I implement the transverse correlation study in a quasi-continuous system, which simulates a collective Heisenberg Hamiltonian. This system behaves as a long-lived synthetic lattice in energy space, preserving the energy and energy state for single particles. Therefore, energy-resolved correlation measurement is particularly suitable for investigating this large energy lattice.

In this many-body spin-lattice, the interplay between the site-dependent energy and site-to-site interactions leads to a spin-locked state, which was observed by Ref. (Smale et al. 2019) and referred to as a transition between dynamic phases. In my transverse spin correlation measurements, this transition is observed both via microscopic energy-resolved correlation and the macroscopic magnetization calculated from it. My measurements enable the observation of correlation flow among the energy partition pairs, and connect the correlation evolution to the system magnetization at different interaction strengths.

Fig. 1.4 shows the macroscopic magnetization at different interaction strengths and the trend of corresponding transverse spin correlation flow (insets of each panel). The insets show the transverse spin correlation between energy partition pairs E_i and E_j, normalized by atom numbers in each energy group: $\boldsymbol{c}^{\perp}_{ij} = \frac{1}{2}\langle s_{xi}s_{xj} + s_{yi}s_{yj}\rangle/(N_iN_j/4)$. The macroscopic magnetization is calculated from the correlation using: $\mathscr{M}^2_{\perp} \equiv S^2_x + S^2_y = \sum_{i,j}(s_{xi}s_{xj} + s_{yi}s_{yj})$. These new measurements microscopically observe the emergence of strong correlations between transverse spin components in localized low-energy and high-energy subgroups and the spread of these correlations throughout the energy lattice as interaction strength increases. These observations highlight energy-space correlation as a new observable in quantum phase transition studies, decoding system features that are hidden in macroscopic measurements.

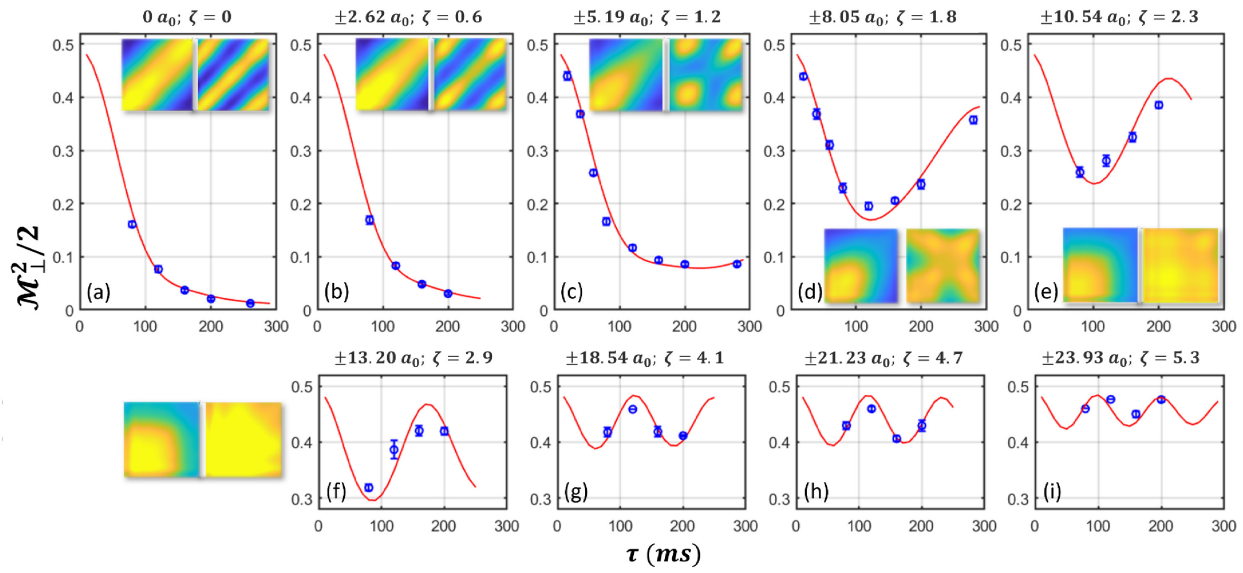

Figure 1.4: Time-dependent magnetization with different interaction strengths. Blue circles are averaged data after data selection method. In setts in each panel shows $\boldsymbol{c}_{ij}^{\perp}$ with corresponding ζ at $\tau = 80$ ms (left and 200 ms (right). For the insets, only $E_i, E_j \in [0, 0.7]E_F$ are shown. The $\boldsymbol{c}_{ij}^{\perp}$ plots on the bottom row correspond to panel (f). As the qualitative behavior of $\boldsymbol{c}_{ij}^{\perp}$ is very similar to (f) for higher scattering length, the correlation figures are not shown for (g-i).

1.2 Dissertation Organization

In Ch. 2, I introduce the electronic structure of ^{6}Li atoms and the hyperfine states adopted to implement experiments in this dissertation. I will introduce magnetically controlled Feshbach resonance which allows tunable two-body scattering interactions. Then I overview the laser cooling setup and procedures adopted by our research group.

In Ch. 3, I present the derivation of the system Hamiltonian, which describes both the effects of the trap potential on atoms and the collisional interaction between atoms. With the Hamiltonian derived, I introduce the quasi-classical spin vector evolution model and explain the modifications I make to this model compared to its previous version. I also present the numerical values of parameters that go into the model in real units so that readers can get a sense of which term in the model dominates for different experimental parameters. At the end of the chapter, I describe the method of characterizing the trap potential, which are critical parameters in the model.

In Ch. 4, I overview the concept of spin segregation and describe the experimental procedure to observe this effect in a coherently excited ^{6}Li sample near the zero-crossing magnetic field where scattering length vanishes. An anomalous phenomenon is observed in this experiment, which is not predicted by the model at long evolution times suggesting the existence of missing

pieces in the mean-field model introduced in the last chapter. I present a statistical attempt to study this.

In Ch. 5, to study the reversibility of the Hamiltonian for this experimental system, I perform quantum rewinding experiments systematically at different scattering lengths with different forward evolution times. I describe the experimental procedures to implement the quantum rewinding experiments and introduce a method to quantify the reversal result. I utilize this quantification method to find the zero-crossing magnetic field precisely. By observing the reversal behavior, I propose possible explanations for the anomalous phenomenon observed in last chapter. With the understanding of reversibility of the system with different experimental parameters, I make decisions on the experimental conditions to adopt for perturbed quantum rewinding measurements, discussed in the next chapter.

In Ch. 6, I describe perturbed quantum rewinding experiments to examine the adequacy of the quasi-classical model discussed in Ch. 3. Also, I describe the protocol to implement this experiment and illustrate the effect of different RF detunings during different evolution periods on the system and measurements, resolving an outstanding conflict observed in a previous study of our research group. The data obtained from perturbed quantum rewinding show quantitative agreement with the modified quasi-classical spin vector model.

In Ch. 7, I present the study of correlation of spin vectors between atoms with different energies. By measuring the $s_{zi}s_{zj}$ correlation, I show that the system is not quantum correlated. With the understanding of time-dependent RF detuning, I demonstrate a data selection method to ensure an RF phase shift distribution across the whole data set, enabling the ensemble-averaged correlation measurement of transverse components of spin vector $s_{xi}s_{xj} + s_{yi}s_{yj}$ based on energy-resolved operator products. I use this data selection method to observe the transverse spin correlation distribution as a function of time and interaction strength and associate the local correlation behavior with the evolution of the macroscopic magnetization.

In Ch. 8, I summarize the conclusions drawn from the work presented in this dissertation and suggest possible future experiments.

In Appendix A, I present the data processing procedures to minimize the imaging and fitting artifacts and experimental defects for all experiments implemented in this thesis.

In Appendix B, I describe the method of Abel inversion to extract energy space information from spatial profiles.

CHAPTER

2

BACKGROUND

All experiments presented in this dissertation are implemented with ^{6}Li Fermi gas. In this chapter, I will overview background knowledge about ^{6}Li, the alkali adopted in our system, and basic concepts about laser cooling and interaction tuning techniques. I describe the electronic structure of ^{6}Li atoms first. With this basic knowledge, I will introduce the concept of Feshbach resonance, which allows the tuning of interactions. In the second section, I will describe the atom capture and cooling apparatus and procedure.

2.1 Tunable interaction of ^{6}Li gas

In the past, the hyperfine structures of some alkali metal atoms have been utilized to realize the Fermi model which has SU(2) symmetry. In our experimental system, the alkali metal adopted is an isotope of Lithium, ^{6}Li.

2.1.1 ^{6}Li hyperfine structure

^{6}Li atom has three protons, three neutrons and three electrons, giving a neutral charge in total. The unpaired valence electron and a nuclear spin of 1 make ^{6}Li atom a fermion. Its ground state, $1s^2 2s^1$, has a nuclear spin, $I = 1$, electronic spin $S = 1/2$, and orbital angular momentum

$L = 0$. Hence, the allowed values for total atomic angular momentum are $F = 3/2$ and $F = 1/2$ by angular momentum addition, corresponding to the two hyperfine states of $^2S_{1/2}$ shown at the bottom in Fig. 2.1. D_1 and D_2 label the transition between ground states and the first excited state. D_2 transition is used in two-level atom trapping and cooling, which will be introduced in Sec. 2.2 with more detail. Without external magnetic fields, the total angular momentum $\mathbf{F} = \mathbf{I} + \mathbf{S}$ is conserved. For the ground state, $F = 1/2$ manifold allows $m_F = \pm 1/2$, yielding 2-fold degeneracy and $F = 3/2$ manifold allows $m_F = \pm 3/2, \pm 1/2$ yielding 4-fold degeneracy.

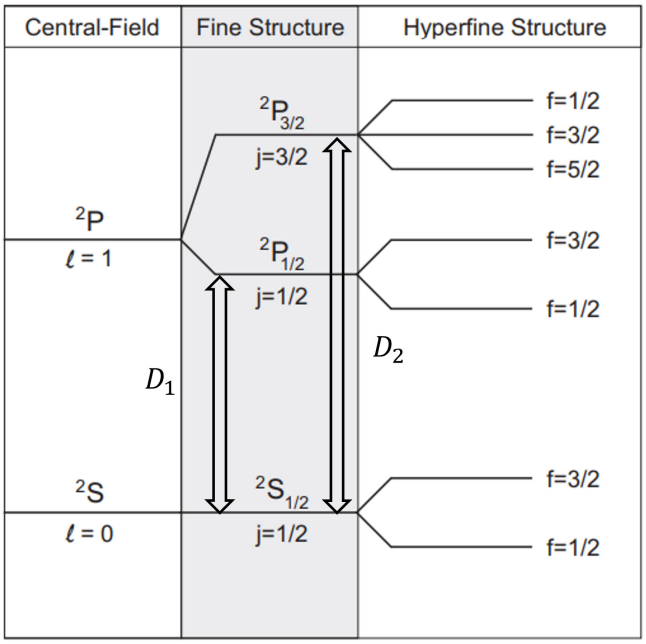

Figure 2.1: Atomic structure of ^{6}Li without the presence of magnetic field. D_1 and D_2 are transitions from ground state to excited state. (Figure drawn by S. R. Granade in his thesis (Granade 2002))

With the presence of high magnetic field, the degeneracy is broken by the interaction described by the following Hamiltonian for the combined hyperfine and Zeeman interaction (Houbiers et al. 1998):

$$H_{int} = \frac{a_{hf}}{\hbar^2}\mathbf{S}\cdot\mathbf{I} - \frac{\mu_B}{\hbar}(g_I\mathbf{S} + g_I\mathbf{I})\cdot\mathbf{B}, \tag{2.1}$$

with constants:

$a_{hf}/h = 152.14$ MHz:	hyperfine interaction constant;
μ_B:	Bohr magneton;
$g_J = -2.002$:	total electronic g-factor for ground state ^{2}Li atom (Arimondo et al. 1977);
$g_I = 0.000448$:	total nuclear g-factor (Arimondo et al. 1977).

Six eigenstates of the Hamiltonian are labeled from $|1\rangle$ to $|6\rangle$ in the order of increasing energy. As the magnetic field magnitude grows larger, the Zeeman shift starts to dominate the hyperfine interaction. The hyperfine energy shift becomes linear and is approximately -1.4 MHz/G for states $|1\rangle$, $|2\rangle$ and $|3\rangle$.

In experiments presented in this dissertation, a mixture of state $|1\rangle$ and $|2\rangle$ is adopted. As the magnetic field changes, the energy difference between states $|1\rangle$ and $|2\rangle$ varies, corresponding to the resonance frequency of RF pulse for the atomic transition between these two states. The atomic transition frequency is a monotonic function of the magnetic field. Hence, the magnetic field can be measured precisely using RF spectra as described in Sec. 4.3.2.

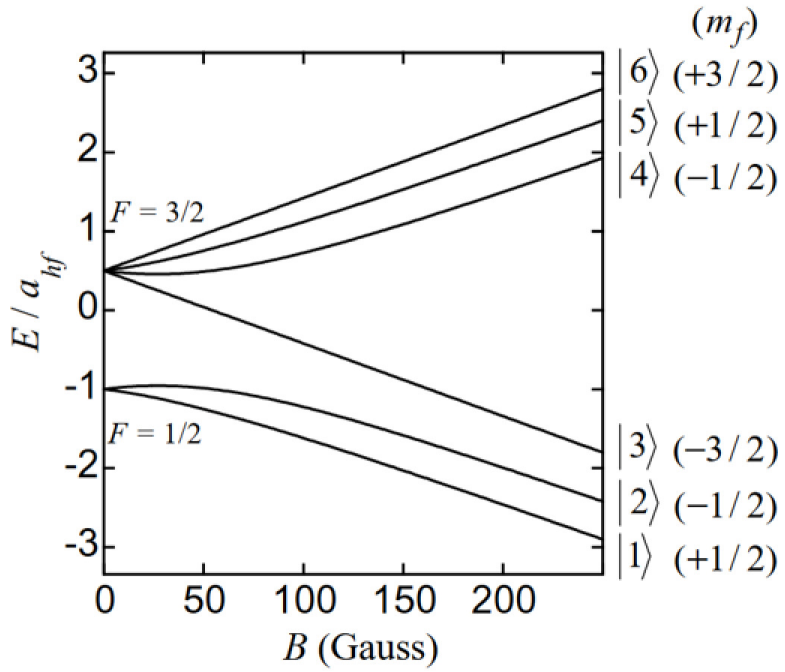

Figure 2.2: Energy tuning of hyperfine ground states of ^{6}Li with external magnetic fields. (Figure drawn by S. R. Granade in his thesis (Granade 2002))

There are two main reasons to implement the experiments with the mixture of $|1\rangle$ and $|2\rangle$ states. First, this mixture is energetically stable. It is stable against collisional decay. Higher

energy mixtures may have open elastic collision channels which allow changes in internal states of atoms. During this process, the atoms release energy and cause other atoms to leave the trap. Therefore this kind of mixture doesn't have a long lifetime. Another reason is the symmetry in the states consisted by $|1\rangle$ and $|2\rangle$ mixture: they are mirror images of one another which only differ in the sign of the magnetic quantum number. This property makes the $|1\rangle$-$|2\rangle$ mixture an ideal system to study quantum coherence.

2.1.2 s-wave scattering

For the ultracold ^{6}Li atomic gas, the interatomic potential range r for the colliding pair is on the order of 1 nm, and the thermal de Broglie wavelength $\lambda \approx 700$ nm. According to the Bohr relationship:

$$l_n \hbar = \frac{nh}{2\pi},$$

where $n = 2\pi r/\lambda$, the quantized angular momentum $l_n \sim 10^{-3}$. Therefore in such a sample, only $l = 0$ term in the partial wave amplitude matters, which means that the quantum scattering process is dominated by s-wave. The s-wave radial wavefunction in Schrödinger equation has the form:

$$\left[\frac{d^2}{dr^2} + \frac{2\mu_m}{\hbar^2}(E - V(r))\right] u(r) = 0, \tag{2.2}$$

with $\mu_m = m/2$ for two identical atoms of mass m. $u(r) = rR(r)$ where $R(r)$ is full radial wave function. Since the potential term goes to zero as $r \to \infty$, neglecting the potential term in Eq. 2.2 yields the asymptotic solution:

$$\begin{aligned} u(r) &= A\sin(kr + \delta) \\ &= A[\sin(kr)\cos(\delta) + \cos(kr)\sin(\delta)]. \end{aligned}$$

Since the system is at the low energy limit, k is extremely small. Apply small angle approximation to the equation above and get:

$$u(r) \approx A[kr\cos(\delta) + \sin(\delta)]$$

$$u(r) = A\sin(\delta)\left[\frac{kr}{\tan(\delta)} + 1\right]. \tag{2.3}$$

The s-wave scattering length a_s is defined as the place where $u(r)$ intersect with r-axis:

$$u(a_s) = A\sin(\delta)\left[\frac{ka_s}{\tan(\delta)} + 1\right] = 0$$

$$\Rightarrow \qquad a_s \equiv -\frac{\tan(\delta)}{k}. \tag{2.4}$$

With the definition shown in Eq. 2.4, the physical meaning of scattering length is the phase shift in the particle wavefunction by the scattering potential (Sakurai 1993). Positive scattering length indicates a repulsive interaction and negative scattering length indicates an attractive interaction. A large absolute value in the scattering length means strong interparticle interaction.

The s-wave scattering cross-section has a form (Sakurai 1993)

$$\begin{aligned}\sigma_c &= \frac{4\pi}{k^2}\sin^2(\delta) \\ &= \frac{4\pi}{k^2}\frac{\tan^2\delta}{1+\tan^2(\delta)}\end{aligned}$$

which can also be written in terms of scattering length:

$$\sigma_c = \frac{4\pi a_s^2}{1+(ka_s)^2} \approx 4\pi a_s^2 \tag{2.5}$$

at the low energy limit for small k.

2.1.3 Feshbach resonance

Feshbach resonance is illustrated by this Fig. 2.3 for two potentials. Consider two atoms separated by a distance R, with a background potential $V_{bg}(R)$ (black) that is lower than the potential $V_c(R)$ (red) as can be achieved by tuning interactions. $V_{bg}(R)$ connects two free atoms states when they collide. This is called the entrance channel or open channel. When the total energy E of this colliding pair is in between two potentials at infinitely large R, then $V_c(R)$ is called the closed channel because it is energetically inaccessible. Since the closed potential has a minimum at small R, a bound state is allowed. Assume there is a bound state with energy E_c. When $E = E_c$, Feshbach resonance happens and the two channels have strong coupling. When the bound state in the closed channel has a different magnetic moment from the scattering state in the open channel, the energy difference between E and E_c can be tuned by the magnetic field. This way, magnetic field controlled Feshbach resonance is achieved.

During the collision of two ground state ^{6}Li atoms, two valence electrons can form spin singlet state with $s = s_1 + s_2 = 0$ or spin triplet state with $s = s_1 + s_2 = 1$. The triplet potential threshold for $|1\rangle$-$|2\rangle$ collision is lower than the singlet one. Thus in the case of this ^{6}Li $|1\rangle$-$|2\rangle$ mixture, the triplet potential is the open channel and the singlet state is the closed channel. The spins in triplet state are parallel to each other, so the total energy tunes with the magnetic field

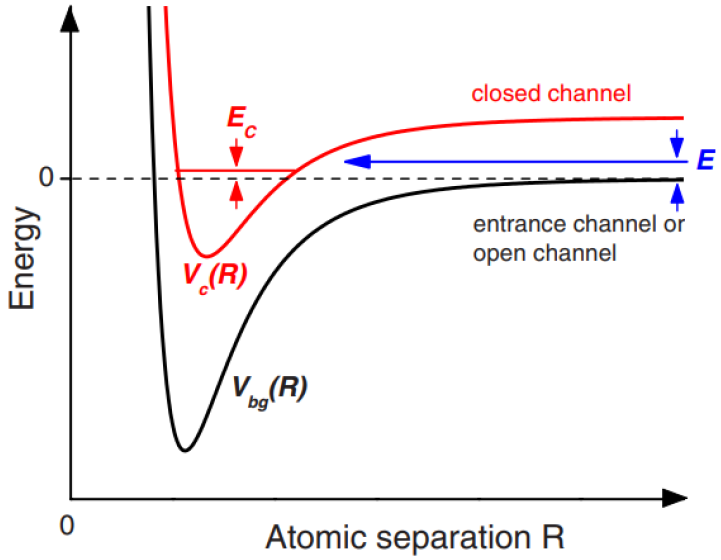

Figure 2.3: Two-channel model for Feshbach resonance. (Figure taken from Chin et al. (2010))

at a rate of $-2\mu_B$. The spins in singlet state are antiparallel to each other, so they tend to resist the effect of external magnetic field as energy change for each spin is equal but with opposite sign. Therefore, the total energy of the colliding pair in the open channel is tuned by applying an external magnetic field to resonate with the molecular bound state in the closed channel, giving Feshbach resonance. Under this condition, the scattering length of the colliding pair diverges, enhancing the interaction strength.

For ^{6}Li $|1\rangle$-$|2\rangle$ pair the Feshbach resonance is at 832.2 G. Fig. 2.4 shows the change of scattering length around this magnetic field. In this dissertation, experiments are implemented near the magnetic field where s-wave scattering length goes to 0, about 527.15 G circled in Fig. 2.4. In this region, by tuning the magnetic field, not only the strength of interaction can be controlled, but also the sign of the interaction.

2.2 Laser cooling

In this chapter, I will briefly introduce the standard laser cooling procedure that brings the sample from its vaporization temperature to degeneracy. Initially, the sample is vaporized in the oven at $\sim 395^\circ C$. First, the sample is precooled by a Zeeman slower so that it can be captured and cooled further by a magneto-optical trap (MOT). Then the cloud is loaded into a CO_2 laser optical dipole trap and undergoes two evaporative procedures at the Feshbach resonance magnetic field. In the end, the sample reaches degeneracy in the combined trap of

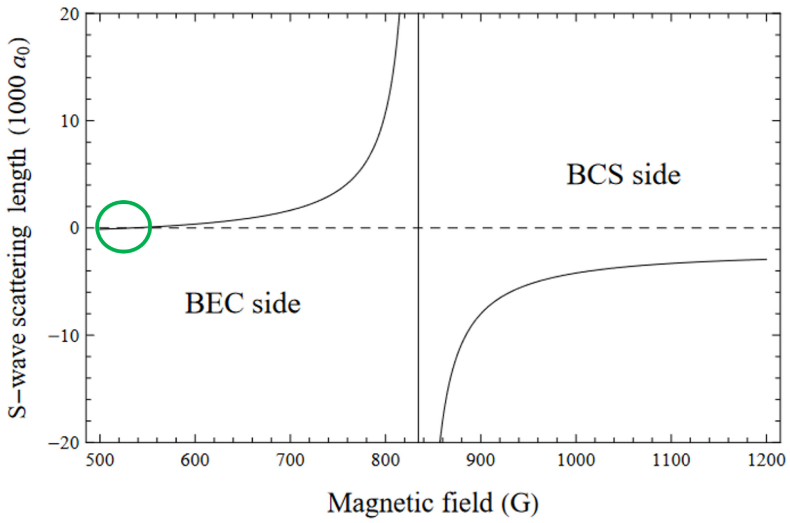

Figure 2.4: s-wave scattering length for ^{6}Li $|1\rangle$-$|2\rangle$ collision as a function of magnetic field. (Figure taken from Zhang (2013))

CO_2 laser and magnetic bowl arising from the bias magnetic field curvature.

Since laser cooling has been a very standard procedure in ultracold atom/molecule studies for decades, I will only briefly show the basic physics of radiation pressure and how it is utilized in our experimental system. To learn more details about numerical calculations and equipment model numbers adopted by our group, I strongly recommend readers to refer to the dissertation of Ken O'Hara (O'Hara 2000).

2.2.1 Radiation pressure

Both Zeeman slower and MOT cool atoms with radiation pressure. In the precooling stage, the momentum of atom is much larger than the momentum of a photon that it absorbs. Thus, the atoms can be slowed precisely by controlling the propagation direction of photons that they absorb. When the photon frequency resonates with the frequency of two-level transition in an atom, the atom absorbs the photon, changing its momentum. Then the atom spontaneously decays back to its ground state and emits a photon in a random direction. So the emission process does not affect the average momentum of a group of atoms. Only considering the absorption process, the atom experiences the average force from a beam with wave vector k:

$$F = \hbar k \frac{\Gamma}{2} \frac{I/I_0}{1 + I/I_0 + (2\delta/\Gamma)^2}. \tag{2.6}$$

Γ is the natural linewidth of the atomic emission spectra ($1/\Gamma$ is the excited state lifetime), I is the intensity of the cooling beam, saturation intensity I_0 is defined by $I_0 \equiv c\pi h\Gamma/3\lambda^3$, and δ is the detuning of the laser frequency from two-level resonance frequency.

Experimentally, the atoms at a specific position can be slowed at a specific rate by controlling the detuning with Doppler effect and Zeeman effect. Doppler effect is related to the atom velocity:

$$\delta = \delta_0 - \mathbf{kv}. \tag{2.7}$$

δ_0 is the difference between transition frequency and cooling beam frequency. The Zeeman effect arises from the Zeeman splitting with the presence of magnetic field. By designing and arranging the magnetic field spatially, Zeeman effect is utilized to control the cooling effect for atoms locate at a specific position.

2.2.2 Zeeman slower

The temperature in the oven can reach $395°C$. This temperature is too high for a magneto-optical trap to capture the atoms. Hence, the atoms need to be precooled before they enter the experiment chamber. The collimated atomic beam is directed through a long path at the center of a device (Zeeman slower) shown in Fig. 2.5, counter-propagating against a laser beam (cooling beam) and experiencing a radiation pressure force Eq. 2.6 from the cooling beam. The Zeeman slower provides a magnetic field whose magnitude changes along the direction of atom motion. While the atoms are slowed, the Doppler shift changes. The magnetic field in the Zeeman slower changes in strength to cancel the Doppler shift, forcing the atoms to resonate with the cooling beam throughout the whole slowing region. This way, the atoms are slowed continuously.

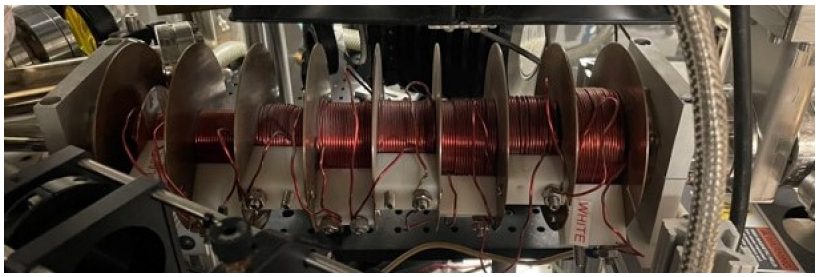

Figure 2.5: Picture of Zeeman slower.

With the presence of a varying magnetic field in a 1D motion (as in Zeeman slower shown

in Fig. 2.5), the detuning δ_0 in Eq. 2.7 has the form:

$$\delta = \delta_0 - kv - \frac{\mu_B B}{\hbar}.$$

If assume the atoms are slowed at a constant acceleration a and their initial velocity is v_i, then at the spatial position x along the direction of atoms motion, its velocity is $v = \sqrt{v_i^2 - 2ax}$. To guarantee the resonance between atoms and the cooling beam, the magnetic field is calculated:

$$B(x) = \frac{\hbar\delta_0}{\mu_B} + \frac{\hbar k}{\mu_B}\sqrt{v_i^2 - 2ax}.$$

With this equation for the required magnetic field as a function of displacement of the atoms, the coil on Zeeman slower can be designed.

In our system, the atomic beam enters the Zeeman slower with a speed of $\sim 10^3$ m/s and exists with a speed of 30 m/s.

2.2.3 Magneto-optical trap

After entering the main experiment chamber, the atoms are confined and cooled by three pairs of retroreflected orthogonal beams and a magnetic field as shown in Fig. 2.6. Red beams are MOT beams that intersect at the center of the ultrahigh vacuum chamber. The orange coils provide a quadrupole gradient magnetic field that is only used for cooling procedures in MOT. The main magnetic field used to tune the interaction strength of the system is provided by a separate pair of coils which are concentric with the MOT coils but with thicker wire as they need to handle much higher current (up to 120 A). Due to the configuration of this pair of MOT coils, the magnetic field has its minimum strength in between the two coils and increases in all directions linearly from the center. Thus the energy shift also varies spatially from the center point. The cooling mechanism provided by Zeeman shifts and Doppler shifts are nominally the same as the Zeeman slower, but the cooling and confinement effects are in all six directions.

The two-level system (cooling states) used for cooling in our system are ground state ($J = 1/2$) $F = 3/2$ and excited state ($J = 3/2$) $F = 5/2$, corresponding to the D_2 transition shown in Fig. 2.1. The optical pump beams (MOT beams) are circularly polarized such that they resonate with the transition between two cooling states as shown in Fig. 2.7. Therefore, the optical pump beams keep most atoms in the cooling cycle between the two-level state. Note that, a repump beam is needed, too. When the atomic beam comes out from the Zeeman slower, it also contains a ground state $J = 1/2$, $F = 1/2$. Also, due to the spontaneous emission (the wavy arrows in Fig. 2.7), electrons can deexcite into the ground state $J = 1/2$, $F = 1/2$, since this is also a hyperfine state of the ground state. To keep as many atoms as possible in

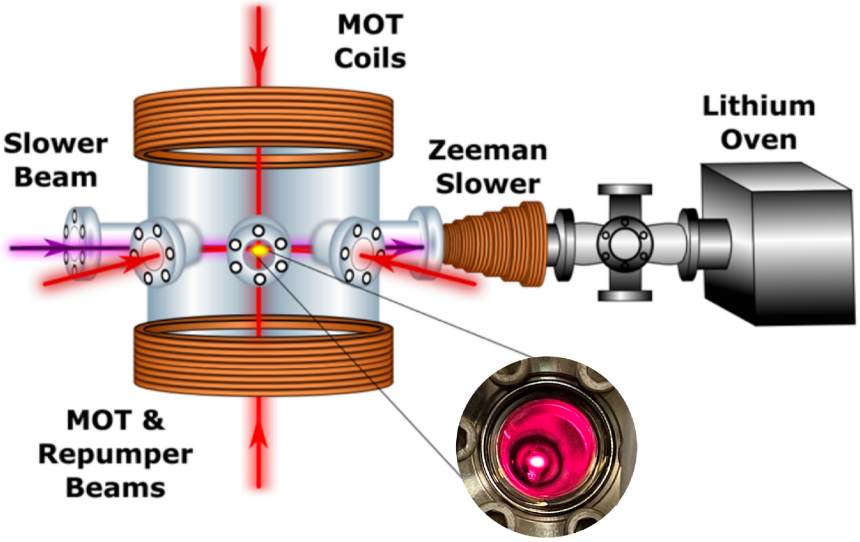

Figure 2.6: Experimental setup for laser cooling. Red beams are MOT and repumper beams. Purple beam is the slower beam. Orange coils on top and bottom demonstrate the coils generate rather low magnetic field which only serves the purpose of MOT (the main magnet which generates bias magnetic field to tune interaction strength is not depicted in this figure). The orange coil on the right of the chamber is a part of Zeeman slower described in Sec. 2.2.2. The inset picture is real picture of a sample fluorescence in MOT. (Illustration figure except for the inset is taken from Kangara (2018))

the two-level system cycle, a repump beam is applied, whose frequency corresponds to the transition between $J = 1/2$, $F = 1/2$ and $J = 3/2$, $F = 5/2$ as shown in Fig. 2.7. With the repump beam, once the atom decays to $F = 1/2$ ground state, it is excited to $F = 5/2$ excited state again.

Therefore, for this cooling procedure, three frequencies are needed. A beam with a wavelength near the D_2 resonance (~ 671 nm) is generated by a dye laser and split into three beams: slower, optical pump, and repumper. The slower beam has its own beam path to go into Zeeman slower while MOT and repump beams share the same beam paths as shown in Fig. 2.6 with purple and red colors respectively.

The lowest temperature that the MOT can achieve is limited by the recoil momentum of spontaneously emitted photons is referred to as the Doppler limit and is gien by:

$$T_D = \frac{h\Gamma}{2k_B} \approx 140\,\mu\text{K}$$

for our system, and the average velocity is about 0.6 m/s.

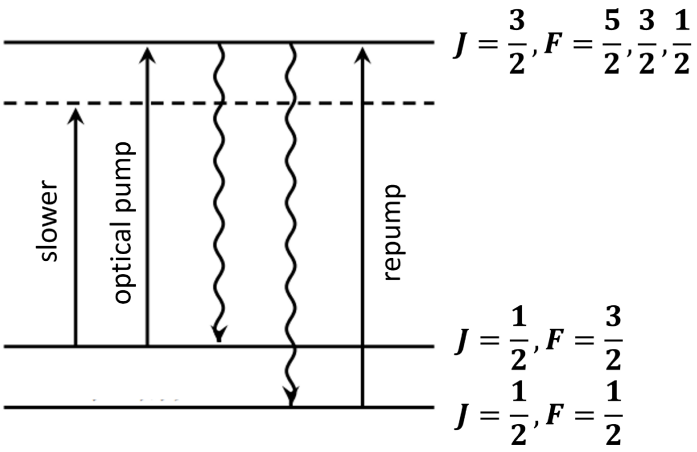

Figure 2.7: Two-level states for cooling.

2.3 Evaporative cooling

To achieve degeneracy, evaporative cooling is required, which consists two processes: free evaporation and forced evaporation. During these processes, the cloud is confined in optical dipole trap created by a high power CO_2 laser and magnetic bowl potential close to Feshbach resonance magnetic field ($\sim$ 832.2 G).

2.3.1 Far-off-resonance trap

A CO_2 laser provides an attractive far-off-resonance trap (FORT). The CO_2 laser power is about 140 W at output and its wavelength is 10.6 μm. The beam is focused to $w = 50\,\mu$m $1/e^2$ radius and the Rayleigh length is calculated by $z_0 = \pi w^2/\lambda \approx 741\,\mu$m. The laser frequency ω is far below the resonance frequency ω_0. Using above information, atoms in this trap experience a potential from dipole interaction:

$$V = -\frac{2\pi}{c}\underbrace{\frac{a_0\omega_0^2}{\omega_0^2-\omega^2}}_{\alpha(\omega)}\underbrace{\frac{I_0}{1+(z/z_0)^2}e^{-2r^2/w^2}}_{I(z)},$$

where $\alpha(\omega)$ is the polarizability of ^{6}Li with laser frequency ω and static polarizability for frequencies far below resonance $a_0 = 2\mu_{eg}^2/\hbar\omega_0$. $I(z)$ is the laser intensity at axial position z. With this equation, one can see that the atom in this potential is attracted to the focus of the beam since $\omega << \omega_0$.

With atoms confined in the FORT, a bias magnetic field is applied to tune the atoms to strongly interacting regime, close to Feshbach resonance. The magnetic field is supplied by

a pair of coils located concentrically with the MOT coils on top and bottom of the vacuum chamber. In this regime, atoms collide frequently. During the collisions, atoms with higher energy escape from the trap and those with lower energy remain. This way, the cloud is cooled after rethermalization. This passive procedure is called free evaporation and it can cool the cloud down to $\sim 50\,\mu$K. After free evaporation is done, the power of CO_2 laser is gradually lowered over a few seconds to about 0.015% of its maximum power. The varying trap depth keeps the evaporation process happening continuously. This process is called forced evaporation. At the end, the cloud reaches a temperature of order 10 nK.

At this point, the atom cooling procedure is completed for my experiment. Further preparation procedures to create a sample with coherent 50-50 superposition state will be described in Sec. 4.1 and protocols for different experiments will be described in the corresponding chapters.

CHAPTER

3

QUASI-CLASSICAL SPIN MODEL

In this dissertation, all experiments are implemented in the weakly interacting regime, where there is no energy-exchanging collisions during experimental cycles. The experiments start from samples with coherent superposition state $|1\rangle$ and $|2\rangle$, which are the two lowest hyperfine states described in Sec. 2.1. The interaction strength and sign are tuned near the zero-crossing magnetic field by main magnet and an extra pair of low-inductance coils. This many-spin system simulates spin lattices in energy space with effective long-range interactions

In this chapter, I present the derivation of a quasi-classical spin model describing such system. First, I will derive both non-interacting and interacting terms of the Hamiltonian for many-body spin dynamics, and then I will list the experimental parameters in real units and their measurement methods. With these quantities, each term in the Hamiltonian will be assigned a number in real units so that one can see what are the conditions to switch from one term dominated regime to another term nominated one. This way, the model can be studied in different regimes by adopting different experimental parameters.

3.1 System Hamiltonian

Because of the strong radial confinement of CO_2 laser trap, the cloud has a cigar shape, whose axial (x) dimension is much larger than the radial (ρ) one. In this section, the sample is treated

as a $1D$ cloud because of its geometry, and the combined trapping potential from magnetic bowl and optical trap is spin-dependent along x-axis of the cloud.

Before deriving the equations, I'd like to define useful notations in this section:

$\|1\rangle \equiv \|\uparrow\rangle$	: spin up, the lowest hyperfine state.
$\|2\rangle \equiv \|\downarrow\rangle$	: spin down, the second lowest hyperfine state.
$\omega_{x\uparrow}$ and $\omega_{x\downarrow}$	: the harmonic oscillation frequencies for two spin states.
$\delta\omega_x \equiv \omega_{x\downarrow} - \omega_{x\uparrow}$	: difference between oscillation frequencies for two states
$\overline{\omega}_x \equiv (\omega_{x\downarrow} + \omega_{x\uparrow})/2$	: mean oscillation frequency
ω_{HF}	: hyperfine resonance frequency for two states $\|\uparrow\rangle$ and $\|\downarrow\rangle$, such that the rest energy difference between two states is $\hbar\omega_{HF}$.
$\omega_{res} \equiv \omega_{HF} + (n+\frac{1}{2})\delta\omega_x$	: the resonance frequency for the transition from $\|\uparrow\rangle$ to $\|\downarrow\rangle$ of oscillating atom in state $\|n\rangle$.

The system Hamiltonian consists of two parts:

$$H = H_0 + H_I.$$

H_0 is the Hamiltonian for non-interacting atoms, describing the spin-dependent effect of axial trap potential on atoms. H_I is the interacting term, describing the collisional effect between atoms in two spin states.

3.1.1 Non-interacting term

The non-interacting Hamiltonian for this system describes the effect of trap potentials on atoms.Since the cloud is treated as a 1D sample, the axial motion of the atoms is of interest, which is described by the non-interacting Hamiltonian:

$$H_0 = \sum_{n,\sigma} |n\rangle\langle n| \left[(n+\frac{1}{2})\hbar\omega_{x,\sigma} |\sigma\rangle\langle\sigma| \right], \tag{3.1}$$

where $|\sigma\rangle$ represents the spin state, and n is the energy level. With $\overline{\omega}_x$ and $\delta\omega_x$ defined at the beginning of this section, the terms in the Hamiltonian can be rearranged:

$$H_0 = \sum_{n} |n\rangle\langle n| \left[(n+\frac{1}{2})\hbar\overline{\omega}_x (|\uparrow\rangle\langle\uparrow| + |\downarrow\rangle\langle\downarrow|) - (n+\frac{1}{2})\hbar\delta\omega_x \frac{(|\uparrow\rangle\langle\uparrow| - |\downarrow\rangle\langle\downarrow|)}{2} \right] \tag{3.2}$$

Since the system is regarded as an energy space spin-lattice, where the single-particle energy conserves during experimental cycle, it is convenient to describe the system in energy representation.

Define:

$E \equiv (n+\frac{1}{2})\hbar\overline{\omega}_x$: mean energy with mean oscillation frequency for spins in n^{th} energy level

$s_z \equiv \frac{1}{2}(|\uparrow\rangle\langle\uparrow| - |\downarrow\rangle\langle\downarrow|)$: the single particle spin operator.

The non-interacting Hamiltonian becomes

$$H_0 = \sum_E |E\rangle\langle E| \left[\sum_\sigma E|\sigma\rangle\langle\sigma| - (n+\frac{1}{2})\hbar\delta\omega_x s_z(E) \right]. \tag{3.3}$$

The last term is the effect of precession caused by the bias magnetic field and the different magnetic moments for two spins. Define the energy-dependent precession Ω'_E in term of oscillation frequencies,

$$\Omega'_E \equiv -(n+\frac{1}{2})\hbar\delta\omega_x = -\delta\omega_x \frac{E}{\hbar\overline{\omega}_x}, \tag{3.4}$$

then the Hamiltonian has the form:

$$H_0 = \sum_E |E\rangle\langle E| \left[\sum_\sigma E|\sigma\rangle\langle\sigma| + \hbar\Omega'_E s_z(E) \right]. \tag{3.5}$$

With field operator $\hat{\psi}$ in energy representation

$$\hat{\psi} \equiv \sum_{E,\sigma} \hat{a}^\sigma_E |E\rangle|\sigma\rangle, \tag{3.6}$$

the many-body Hamiltonian is written as

$$\hat{H}_0 \equiv (\hat{\psi}^\dagger H_0 \hat{\psi})_{E,\sigma}, \tag{3.7}$$

where $(...)_{E,\sigma}$ represents the inner products for energy and spin state for a single atom. Adopting the definition of number operators in terms of creation and annihilation operators $\hat{n}^\sigma_E = a^{\sigma\dagger}_E a^\sigma_E$, the many-body Hamiltonian becomes:

$$\hat{H}_0 = \sum_{E,\sigma} E\,\hat{n}^\sigma_E + \sum_E \hbar\Omega(E)\hat{s}_z(E), \tag{3.8}$$

while similar to $s_z(E)$, the many-body spin operator $\hat{s}_z(E)$ in Schrödinger picture is defined to be

$$\hat{s}_z(E) \equiv \left(\hat{\psi}^\dagger |E\rangle s_z(E) \langle E|\hat{\psi}\right)_{E,\sigma} = \frac{1}{2}(\hat{n}^\uparrow_E - \hat{n}^\downarrow_E) \tag{3.9}$$

3.1.2 Interaction term

The quantum scattering process at low temperature is dominated by s-wave collisions. The effective Hamiltonian that describes such interaction between two atoms of different spin at $\vec{x}_1$ and $\vec{x}_2$ has the form:

$$H_I(\vec{x}_1,\vec{x}_2)=\frac{4\pi\hbar^2 a_s}{m}\delta^3(\vec{x}_1-\vec{x}_2), \tag{3.10}$$

where a_s is scattering length. Summing over all pairs, the many-body Hamiltonian can be written as

$$\hat{H}_I=\frac{1}{2}\int d^3\vec{x}_1 d^3\vec{x}_2\hat{\psi}^\dagger(\vec{x}_2)\hat{\psi}^\dagger(\vec{x}_1)H_I(\vec{x}_1,\vec{x}_2)\hat{\psi}(\vec{x}_1)\hat{\psi}(\vec{x}_2), \tag{3.11}$$

the $\frac{1}{2}$ is included to avoid double counting of interaction between atom pairs. Plug Eq. 3.10 into this equation, the many-body operator has the form:

$$\hat{H}_I=g\int d^3\vec{x}\,\hat{\psi}^{\uparrow\dagger}(\vec{x})\hat{\psi}^{\downarrow\dagger}(\vec{x})\hat{\psi}^{\downarrow}(\vec{x})\hat{\psi}^{\uparrow}(\vec{x}), \tag{3.12}$$

for convenience, define coupling constant:

$$g\equiv\frac{2\pi\hbar^2 a_s}{m}. \tag{3.13}$$

Because of the geometry of the cloud, the effect of potential curvature on the oscillation frequency is negligible along radial (ρ) direction compared to axial (x) one. Apply separation of variables to the field operator:

$$\hat{\psi}^\sigma(\vec{x})=\mathrm{P}(\rho)\hat{X}^\sigma(x),$$

where ρ denotes radial direction and x denotes axial direction, and $P(\rho)$ is a function of ρ and $\hat{X}^\sigma(x)$ is a function of x. Radial direction integral in Eq. 3.12 can be evaluated by treating radial probability density $\int 2\pi\rho\,d\rho|P(\rho)|^2=1$. Defining the radial density:

$$n_\perp(\rho)=|P(\rho)|^2,$$

then the effective mean radial density can be calculated by integration:

$$\overline{n}_\perp=\int 2\pi\rho\,d\rho(n_\perp(\rho))^2 \tag{3.14}$$

Plug the definitions in Eq. 3.13 and Eq. 3.14 into Hamiltonian operator in Eq. 3.12:

$$\hat{H}_I = g\overline{n}_\perp \int d\,x \hat{X}^{\uparrow\dagger}(x)\hat{X}^{\downarrow\dagger}(x)\hat{X}^{\downarrow}(x)\hat{X}^{\uparrow}(x), \tag{3.15}$$

Use the position representation of the field operator of Eq. 3.6,

$$\hat{\psi}(x) = \sum_{E,\sigma} \hat{a}_E^\sigma \phi_E(x)|\sigma\rangle \equiv \sum_\sigma \hat{X}^\sigma(x)|\sigma\rangle \tag{3.16}$$

to write the Hamiltonian:

$$\hat{H}_I = g\overline{n}_\perp \sum_{p,q,p',q'} \int d\,x \underbrace{\phi^*_{p'}(x)\phi^*_{q'}(x)\phi_q(x)\phi_p(x)}_{I} \times \underbrace{\hat{a}^{\uparrow\dagger}_{p'}\hat{a}^{\downarrow\dagger}_{q'}\hat{a}^{\downarrow}_q\hat{a}^{\uparrow}_p}_{II}, \tag{3.17}$$

where p, q, p', q' represent energies. For convenience, label the two parts inside the integral as I and II, and evaluate them separately. Again, adopting the mean-field approximation, the operator product in Eq. 3.16 Term II is evaluated by taking the thermal average. Apply the corollary of Wick's theorem so that the n-point correlators can be represented by several 2-point correlators:

$$\langle gs|A_1 ... A_{2n}|gs\rangle = \sum (-1)^P \langle A_{i_1}A_{j_1}\rangle \cdots \langle A_{i_n}A_{j_n}\rangle,$$

where P is the permutation, and the sum is over all partitions of $\{1,\cdots,2n\}$ to pairs $\{(i_1,j_1),\cdots,(i_n,j_n)\}$ for all $i<j$. Expectation value of II for a reference state becomes:

$$\langle II\rangle = \langle \hat{a}^{\uparrow\dagger}_{p'}\hat{a}^{\downarrow\dagger}_{q'}\rangle\langle \hat{a}^{\downarrow}_q\hat{a}^{\uparrow}_p\rangle - \langle \hat{a}^{\uparrow\dagger}_{p'}\hat{a}^{\downarrow}_q\rangle\langle \hat{a}^{\downarrow\dagger}_{q'}\hat{a}^{\uparrow}_p\rangle + \langle \hat{a}^{\uparrow\dagger}_{p'}\hat{a}^{\uparrow}_p\rangle\langle \hat{a}^{\downarrow\dagger}_{q'}\hat{a}^{\downarrow}_q\rangle.$$

The first term is for the Cooper pairs of Fermions $|BCS\rangle = \prod_{\vec{k}}(u_{\vec{k}} + v_{\vec{k}}\hat{a}^{\uparrow\dagger}_{\vec{k}}\hat{a}^{\downarrow\dagger}_{-\vec{k}})|vac\rangle$, it is negligible in the weakly interacting regime, so it's dropped. To the first order approximation, the thermal average takes the form

$$\begin{aligned}\langle II\rangle \simeq &-\langle \hat{a}^{\uparrow\dagger}_{p'}\hat{a}^{\downarrow}_q\rangle\hat{a}^{\downarrow\dagger}_{q'}\hat{a}^{\uparrow}_p - \langle \hat{a}^{\downarrow\dagger}_{q'}\hat{a}^{\uparrow}_p\rangle\hat{a}^{\uparrow\dagger}_{p'}\hat{a}^{\downarrow}_q \\ &+ \langle \hat{a}^{\uparrow\dagger}_{p'}\hat{a}^{\uparrow}_p\rangle\hat{a}^{\downarrow\dagger}_{q'}\hat{a}^{\downarrow}_q + \langle \hat{a}^{\downarrow\dagger}_{q'}\hat{a}^{\downarrow}_q\rangle\hat{a}^{\uparrow\dagger}_{p'}\hat{a}^{\uparrow}_p.\end{aligned}$$

For the purpose of describing spin evolution, thermal average on the Heisenberg operator will be needed again, which means only terms with $p=p'$ and $q=q'$ will remain, otherwise they

go to 0. Therefore, let $E = p = p'$, $E' = q = q'$, and Term I in Eq. 3.16 becomes:

$$I = |\phi_E(x)|^2 |\phi_{E'}(x)|^2$$

and the reduced Hamiltonian is only the sum over E and E':

$$\begin{aligned}\hat{H}_{I,red} = g\overline{n}_\perp \sum_{E,E'} \int dx |\phi_E(x)|^2 |\phi_{E'}(x)|^2 \\ \times \left[-\langle \hat{a}_E^{\uparrow\dagger} \hat{a}_{E'}^{\downarrow} \rangle \hat{a}_{E'}^{\downarrow\dagger} \hat{a}_E^{\uparrow} - \langle \hat{a}_{E'}^{\downarrow\dagger} \hat{a}_E^{\uparrow} \rangle \hat{a}_E^{\uparrow\dagger} \hat{a}_{E'}^{\downarrow} + \langle \hat{a}_E^{\uparrow\dagger} \hat{a}_E^{\uparrow} \rangle \hat{a}_{E'}^{\downarrow\dagger} \hat{a}_{E'}^{\downarrow} + \langle \hat{a}_{E'}^{\downarrow\dagger} \hat{a}_{E'}^{\downarrow} \rangle \hat{a}_E^{\uparrow\dagger} \hat{a}_E^{\uparrow} \right].\end{aligned}$$

After factorization, the interaction Hamiltonian is written in terms of number operators and spin operators:

$$\hat{H}_{I,red} = 2g\overline{n}_\perp \sum_{E,E'} \int dx |\phi_E(x)|^2 |\phi_{E'}(x)|^2 \times \left[\frac{1}{4} N_{E'} \hat{n}_E - \vec{s}(E') \cdot \hat{\boldsymbol{s}}(E) \right]. \tag{3.18}$$

Note that, in this equation, notations are defined this way: N_E and $\vec{s}(E)$ are thermal averaged results for operators $\hat{n}_E$ and $\hat{\boldsymbol{s}}(E)$, respectively. The collective spin operators are defined as:

$$\begin{aligned}\hat{s}_x(E) \equiv \left(\hat{\psi}^\dagger |E\rangle s_x(E) \langle E| \hat{\psi}\right)_{E,\sigma} = \frac{\hat{a}_E^{\uparrow\dagger} \hat{a}_E^{\downarrow} + \hat{a}_E^{\downarrow\dagger} \hat{a}_E^{\uparrow}}{2}. \\ \hat{s}_y(E) \equiv \left(\hat{\psi}^\dagger |E\rangle s_y(E) \langle E| \hat{\psi}\right)_{E,\sigma} = \frac{\hat{a}_E^{\uparrow\dagger} \hat{a}_E^{\downarrow} - \hat{a}_E^{\downarrow\dagger} \hat{a}_E^{\uparrow}}{2i},\end{aligned} \tag{3.19}$$

and $\hat{s}_z(E)$ is defined in Eq. 3.9.

3.2 Numerical Implementation

In this work, the system is treated as a collection of classical spins, and the quantum correlation is assumed to be negligible. While doing calculation, the initial condition is set to be: x-component of total spin vector $S_x = \frac{1}{2}\frac{N}{2}$, and the evolution of the system is described by solving differential equations for $\vec{s}_z$.

3.2.1 Formalism

Because of the anticommutation relations of creation and annihilation operators:

$$\{\hat{a}_E^\sigma, \hat{a}_{E'}^{\sigma'\dagger}\} = \delta(E - E')\delta^{\sigma\sigma'}, \tag{3.20}$$

and Leibniz rules for commutators and anti-commutators,

$$[\hat{a}^{r'\dagger}_{p'}\hat{a}^{r}_{p},\hat{a}^{s'\dagger}_{q}]=\hat{a}^{r'\dagger}_{p'}\delta(p-q)\delta^{r,s'}$$
$$[\hat{a}^{r'\dagger}_{p'}\hat{a}^{r}_{p},\hat{a}^{s}_{q}]=-\hat{a}^{r}_{p}\delta(p'-q)\delta^{r',s}$$

the commutation relations among spin operators defined in Eq. 3.9 and Eq. 3.19 has this cyclic form:

$$[\hat{s}_i(E'),\hat{s}_j(E)]=i\epsilon_{ijk}\hat{s}_k(E)\delta(E'-E). \tag{3.21}$$

With the commutation relation above and both terms for Hamiltonian Eq. 3.8 and Eq. 3.18 derived, apply Heisenberg equation of motion and then take thermal average, the evolution of spin vector $\vec{s}(E)\equiv\langle\hat{\boldsymbol{s}}(E)\rangle$ has the form:

$$\begin{aligned}\dot{\vec{s}}(E,t)&=\frac{i}{\hbar}[\hat{H}_0+\hat{H}_I,\vec{s}(E,t)]\\&=\vec{\Omega}(E,t)\times\vec{s}(E,t)+\sum_{E'}\frac{2g\overline{n}_{\perp}}{\hbar}\underbrace{\int dx|\phi'_E(x)|^2|\phi_E(x)|^2}_{I(E',E)}\vec{s}(E',t)\times\vec{s}(E,t).\end{aligned} \tag{3.22}$$

The integral in Eq. 3.22 is the probability density for the collision between atoms with energy E and E', which is denoted as $I(E',E)$. For convenience, a matrix $g(E',E)$ is defined to describe the coupling between atoms with two energies:

$$g(E',E)=-\frac{2g\overline{n}_{\perp}}{\hbar}I(E',E). \tag{3.23}$$

With these notations, the equation of motion for spin vector $\vec{s}(E,t)$ can be written as:

$$\dot{\vec{s}}(E,t)=\vec{\Omega}(E,t)\times\vec{s}(E,t)+\sum_{E',E}g(E',E)\vec{s}(E',t)\times\vec{s}(E,t), \tag{3.24}$$

and simplified Hamiltonian has the form:

$$\frac{H}{\hbar}=\sum_{E}\Omega_z(E)s_z(E)+\sum_{E,E'\neq E}g(E',E)\vec{s}(E')\cdot\vec{s}(E). \tag{3.25}$$

Here, Zeeman term only has z-component, the reason will be described in Sec. 3.2.3.

Since the single particle energy is much larger than the energy spacing between harmonic oscillator states, the de Broglie wavelength is short compared to the sample dimensions. There-

fore, WKB approximation can be applied to evaluate the integrant:

$$|\phi_E(x)|^2 \approx \frac{\Theta\left[\sqrt{\frac{2E}{m\overline{\omega}_x^2}}-|x|\right]}{\pi\sqrt{\frac{2E}{m\overline{\omega}_x^2}-x^2}}. \tag{3.26}$$

By variable substitution, the integral $I(E',E)$ is evaluated:

$$\begin{aligned} I(E',E) &= \sqrt{\frac{m\overline{\omega}_x^2}{2\pi|E'-E|}}\int_{-\frac{\pi}{2}}^{\frac{\pi}{2}} \frac{d\theta}{\sqrt{1+\frac{E_<}{|E'-E|}\cos^2\theta}} \\ &= \sqrt{\frac{m\overline{\omega}_x^2}{2\pi(E_<+|E'-E|)}}\,K\left(\sqrt{-\frac{E_<}{E_<+E'-E}}\right) \\ &= \sqrt{\frac{m\overline{\omega}_x^2}{2\pi|E'-E|}}\,\mathrm{EllipticK}\left(-\frac{E_<}{|E'-E|}\right) \end{aligned} \tag{3.27}$$

where $E_<$ is the smaller one of E and E'; EllipticK(k) is a variant of the first kind complete elliptic integral $K(k)$ which has a power series form in terms of Legendre polynomials P_i:

$$K(k) = \frac{\pi}{2}\sum_{n=0}^{\infty}(P_{2n}(0))^2 k^{2n}. \tag{3.28}$$

The coupling matrix $g(E',E)$ has the form

$$g(E',E) = -\frac{4g\overline{n}_\perp}{\pi^2\hbar}\sqrt{\frac{m\overline{\omega}_x^2}{2\pi|E'-E|}}\,\mathrm{EllipticK}\left(-\frac{E_<}{|E'-E|}\right) \tag{3.29}$$

with diagonal elements being 0.

3.2.2 Initial condition

From the Fermi physics, the occupation number has a general form:

$$n_\sigma(E_{3D}) = \int dE_{3D}\,\frac{1}{e^{(E_{3D}-\mu)\beta}+1}\sum_{E_x,E_y,E_z}\delta(E_{3D}-E_x-E_y-E_z), \tag{3.30}$$

at low temperature limit, the Fermi distribution becomes a step function $\Theta(E_F - E)$. For a 1D approximation, atom density in terms of energy can be written as:

$$n_\sigma(E) = \frac{3}{E_F}(1 - \frac{E}{E_F})^2 \Theta(E_F - E). \tag{3.31}$$

Here, Fermi energy $E_F = (6N)^{1/3}\hbar\overline{\omega}$, $\overline{\omega}$ is the mean oscillation frequency of the harmonic trap, and N is total atom number. With the initial condition created (described in Sec. 4.1), all atoms are in $|2\rangle$, so $N = N_2$, and spin density in z-direction is the same as total density of two spins.

$$n_{tot}(E, 0) = s_z(E, 0), \tag{3.32}$$

has the distribution shown in Eq. 3.31. Total density profile $n_{tot}(E, t)$ is conserved for all energy E since there are no energy exchange interactions during the experimental cycle. Therefore, $n_{tot}(E, t)$ always has the form in Eq. 3.31 during the evolution.

3.2.3 Precession around z-axis

In equation of motion Eq. 6.17 derived earlier, the first term only has z component due to the geometry of the magnetic field. It consists two parts:

$$\vec{\Omega}(E, t) = [\Omega'_E + \Delta(t)]\hat{z}. \tag{3.33}$$

Ω'_E represents energy dependent Zeeman tuning, arising from the magnetic field curvature and the difference in magnetic moments for two spin states. It is defined by Eq. 3.4:

$$\Omega'_E = -\delta\omega_x \frac{1}{\hbar\overline{\omega}_x} E.$$

First, evaluate $\delta\omega_x$ with known constants: ω_B is the magnetic field frequency, $\overline{\omega}_x$ is the axial trap frequency (measurement shown in Sec. 3.3.2), ω'_{12} is the tuning rate of the transition between state $|1\rangle$ and state $|2\rangle$, and $g_j\mu_B$ is the Zeeman tuning rate of an electron around

zero-crossing:

$$\delta\omega_x \approx \frac{\omega_B^2}{\overline{\omega}_x}\frac{\hbar\omega'_{12}}{g_j\mu_B}$$

$$\omega_B = (2\pi \times 20.5\,\mathrm{Hz})^2 \frac{B[G]}{834}$$

$$\omega'_{12}[527G] = 2\pi \times 3.61\,\mathrm{kHz/G}$$

$$g_j\mu_B = -2\pi \times 2.8\,\mathrm{MHz/G}$$

$$\overline{\omega}_x = \frac{2\pi}{41}\,\mathrm{kHz}$$

$$\Rightarrow \delta\omega_x \approx -2\pi \times 14.21\,\mathrm{mHz},$$

Therefore,

$$\Omega'_E = \frac{0.583 \times 10^{-3}}{\hbar}E.$$

Consider the expectation value of energy $\overline{E} = E_F/4$. Fermi energy E_F sets the characteristic energy of the sample. By direct integration of Eq. 3.30, it has the form:

$$E_F = (6N\overline{\omega})^{\frac{1}{3}}\hbar.$$

The characteristic size of the sample is defined as the excursion of a particle with the total energy E_F in the harmonic trap, and has the form:

$$\sigma_{Fx} \equiv \sqrt{\frac{2E_F}{m\overline{\omega}_x^2}}.$$

In the experiment, σ_{Fx} can be obtained by fitting the measured axial spatial profile of samples with Thomas-Fermi profile, so it's convenient to calculate E_F from measured σ_{Fx}:

$$E_F = \frac{m\overline{\omega}_x^2\sigma_{Fx}^2}{2}$$

$$\approx 1.280 \times 10^{-22},$$

where a typical number for σ_{Fx} in my experiment is about $330\,\mu m$. Then the approximate scale of Zeeman term is:

$$\Omega'_{\overline{E}} \approx 17.66\,\mathrm{rad/s}$$

The other part in the precession term, $\Delta(t)$, is a time dependent global detuning. It is changing at a rate of 5 kHz/G for $|1\rangle$-$|2\rangle$ superposition states because of the fluctuations in the bias magnetic field and magnetic tuning of the scattering length. For the typical evolution time $\tau = 200$ ms, $\Delta(t)$ has an order of 0.4 Hz. This global detuning $\Delta(t) = \omega_{HF}(t) - \omega_{RF}(t)$ plays a central role in understanding perturbed quantum rewinding experimental results in Ch. 6. The detuning causes the components of spin vectors in the Bloch frame to rotate relative to the RF-frame by generally different angles $\varphi = \int_\tau d\,t\,\Delta(t)$. Here, the RF frame is defined by x_{RF} and y_{RF} axes that rotate about the z-axis at the instantaneous RF frequency, $\omega_{RF}(t)$, tracking the total phase of the RF field. In this work, the rotation axes for all of the RF pulses are defined in the RF frame, i.e., $x \equiv x_{RF}$ and $y \equiv y_{RF}$. The Bloch frame is defined by x_B and y_B axes that rotate at the instantaneous hyperfine resonance frequency $\omega_{HF}(t)$ for an atom of axial energy $E = 0$. There is no direct way to measure $\Delta(t)$ or φ, I evaluate φ by fitting experimental data with corresponding model that includes a unique detuning explicitly for each evolution period.

Note that, in all experiments with RF excitations, the unstable detuning exists since it is extremely hard to control the magnetic field at sub-mG level. However, since the detuning only has z-component, the evolution of s_z is not affected. Any measurement of s_z is insensitive to the detuning, this property enables the studies of central spin density evolution (in Ch. 4) and reversibility of a system Hamiltonian (in Ch. 5).

3.2.4 Mean-field term

The second term in Eq. 6.17, lead by $g(E', E)$, is the site-to-site coupling between energy site E' and E. It arises from the collisions between atoms with energy E and E', and describes the rotation of the spin vector of atoms with energy E'. After summation over all atoms in the system, $\tilde{g} \equiv \frac{N}{2} g(E', E)$, and evaluating $\tilde{g}$ numerically can provide an idea about whether the energy-dependent Zeeman tuning or collisional interaction term dominates the Hamiltonian.

Define

$$\Omega_{Fg} \equiv -\frac{N}{2} \frac{4g\overline{n}_\perp}{\pi^2 \hbar} \sqrt{\frac{m\overline{\omega}_x^2}{2E_F}} \tag{3.34}$$

such that

$$\tilde{g}(E', E) = \frac{\Omega_{Fg}}{\sqrt{|E - E'|}} \text{EllipticK}(-\frac{E_<}{|E - E'|}).$$

For low temperature limit $T \to 0$, the radial density of the cloud has the form (derivation shown

in Appendix B.2):

$$n_{\perp}(\rho) = \frac{3}{\pi\sigma_{F\rho}^2},$$

so the mean radial density is calculated by integrating $n_{\perp}(\rho)$ over ρ: $\overline{n}_{\perp} = \frac{9}{5\pi\sigma_{F\rho}^2}$. The radial Fermi radius $\sigma_{F\rho}$ is calculated from measured axial Fermi radius σ_{Fx}, axial and radial frequencies of the harmonic trap (measurement for radial trap frequency is shown in Sec. 3.3.2 and for radial trap frequency is shown in 3.3.1)

$$\begin{aligned}\sigma_{F\rho} &= \sigma_{Fx}\frac{\omega_x}{\omega_\rho} \\ &\approx 12.39\,\mu\text{m}.\end{aligned}$$

Note that, by comparing the axial and radial width of the cloud, it's confirmed that the sample geometry allows the 1D approximation when modeling.

With the measured $\omega_\rho = 2\pi\times 650$ Hz, typical atom number $N \approx 60\,000$, and typical scattering length I work at, $a_s = 5\,a_0$, the mean-field term has the nominal magnitude of $\Omega_{Fg} \approx 18.25$, which is similar to Zeeman term obtained in Sec. 3.2.3.

According to the numerical calculation in this section, scattering length $a_s \approx 5\,a_0$ is a regime where Zeeman term and mean-field term have comparable magnitudes, therefore, it is a regime where the system is not dominated by either term: two terms have comparable contribution during the evolution. Since $g(E', E) \propto a_s$, I work at $3\,a_0$ to study the Zeeman dominated regime and work at $8\,a_0$ to study the mean-field dominated regime.

3.3 Trap characterization

To characterize the trap, the cloud is cooled to degeneracy by evaporative cooling, $T/T_F \approx 0.3$. Then the magnetic field is ramped up by the main magnet coils to a weakly interacting place where $B \approx 1200G$ so that spin state $|1\rangle$ can be eliminated with an imaging pulse. Right after this imaging pulse, the magnetic field is swept down to close to zero-crossing, where $B = 528.803$ G and the corresponding scattering length $a = 5.19\,a_0$. This procedure will be described with more detail in Sec. 4.1.

All experiments presented in this dissertation are implemented close to this magnetic field (~ 529 G). To ensure the degeneracy while avoiding loose too many atoms, I set the lowest point of CO_2 laser trap during forced evaporation at about 0.015% of the largest CO_2 laser power. Then the cloud is recompressed by 2% maximum CO_2 laser power. I characterize the trap with

these parameters in this section.

Radial and axial frequencies are measured using different methods. In the following parts, I present two methods for trap frequency measurements.

3.3.1 Radial frequency

The CO_2 laser trap is parameterized by the $1/e$ intensity radii of the beam waist and potential depth, and they are determined by trap oscillation frequencies for all directions. The standard method to measure an optical trap oscillation frequency is parametric resonance. After the sample is prepared as described at the beginning of this section, CO_2 laser power is raised up to 2% of its maximum power, and it is modulated at a known frequency, which is equivalent to modulating the harmonic trap spring constant. The atoms are parametrically excited when the modulation frequency doubles the trap frequency, and the size of the cloud is noticeably bigger. With this property, the radial trap frequency can be measured.

The procedure described above is repeated with different modulation frequencies in random order, for each frequency, I take six shots. After the cloud is imaged, I fit the radial profile with a Gaussian function, and record the Gaussian width of the cloud as a function of modulation frequency. Fig. 3.1 shows the radial Gaussian width of the cloud changing with the modulation frequency. It suggests that $2\nu_\rho = 1\,300$ Hz, which means that the radial trap frequency $\omega_\rho = 2\pi \times 650$ Hz.

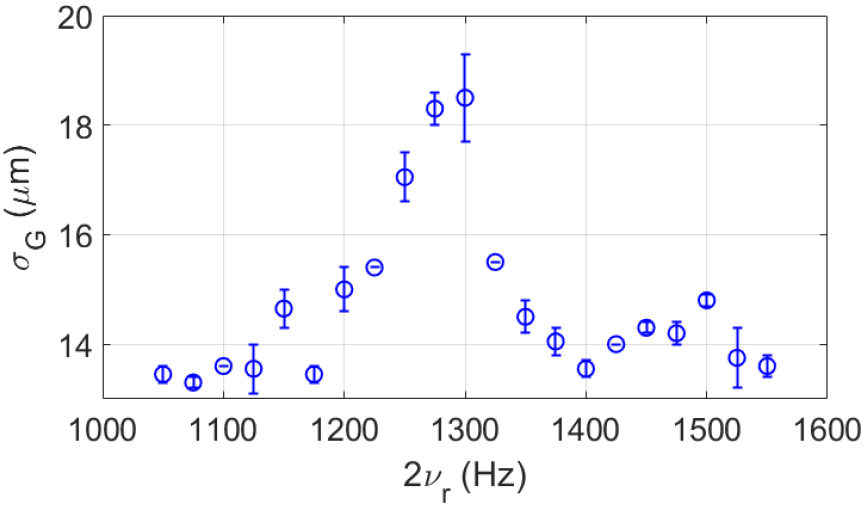

Figure 3.1: Radial width (fitted with Gaussian function) of the sample as a function of parametric excitation frequency. This data set is averaged over six shots for each point.

3.3.2 Axial frequency

For the apparatus described in Ch. 2, the axial trap potential is dominated by the magnetic field, and its frequency is very low compared to the radial one which is dominated by the optical trap. Hence, only modulating CO_2 laser power and keeping magnetic field potential fixed cannot modulate the axial harmonic trap spring constant efficiently, so parametric resonance is not able to measure the axial trap frequency in this case. Instead, it is measured with the help of another infrared laser with 1064 nm wavelength. Here, I call it 1064. The sample is prepared the same way described at the beginning of this section, and then it's transferred into the attractive potential created by 1064 trap, which is misaligned from the center of the magnetic bowl on purpose. Then 1064 laser is turned off, and the cloud is released from the 1064 trap and allowed to oscillate freely along axial direction under the effect of a combination of magnetic bowl potential and CO_2 laser dipole trap at experimental condition ($B \approx 528G$, CO_2 laser power $= 2\%$).

After being released from 1064 trap, the cloud is imaged at different times, and I fit both Gaussian profile and zero-temperature Thomas-Fermi profile to the cloud to extract the position of its center. The position is recorded as a function of time in Fig. 3.2, blue circles are the position of the cloud fitted by zero-temperature Thomas-Fermi profile to the cloud, and green crosses are the position fitted by Gaussian profile. Two fitting models yield the same result, which determine the oscillation frequency $\omega_x = 2\pi \times 24.4$ Hz.

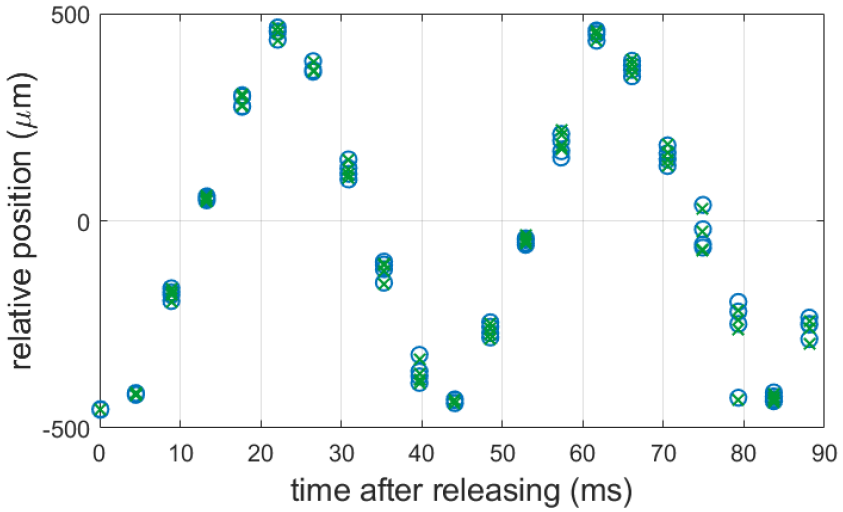

Figure 3.2: Cloud center position as a function of time after releasing from 1064 nm infrared laser.

CHAPTER

4

SPIN SEGREGATION

With the coherently prepared 2-state Fermi gas, spin wave is formed leading to the spin segregation effect, where the local density maxima for two spin states are spatially separated. In this chapter, I describe the experimental procedure and basic calibrations required for an experiment to observe spin segregation. The initial measurement of spin segregation is an essential first step for undertaking the experiments presented in Ch. 5, 6 and 7. By conducting this experiment, I probe the capability of the mean-field model and calibrate and characterize this experimental system. With these understandings, I am able to implement experiments in the next three chapters and utilize the model in a proper way to study correlation and information spreading.

Previously, the spin density evolution in weakly interacting Fermi gasses has been studied by our group (Du et al. 2008; Pegahan et al. 2019), however, investigating the adequacy of the mean-field model wasn't their main goal. The study presented in this chapter suggested that the energy-dependent collective spin-rotation model is sufficient in predicting the system status for a limited length of evolution time, however, at a longer time, the model breaks. Here, I systematically measure the degree of spatial segregation of two spin states as a function of evolution time to probe the model and propose explanations for the model deviations.

4.1 Experimental procedure

Fig. 4.1 shows the time sequence for the spin segregation experiment. A standard laser cooling procedure described in Sec. 2.2 is used to prepare all samples the same way initially. It is shown in red block labeled as region 1 in the figure, and the total time for this procedure is about 8 s.

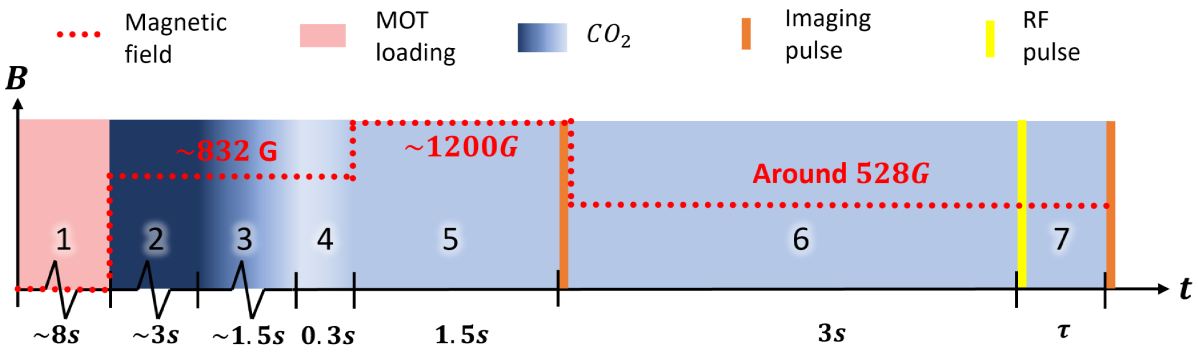

Figure 4.1: Time sequence for spin segregation experiment. Red dashed line shows the magnitude of magnetic field. Red block represents the initial trapping and cooling procedure. Blue block represents the CO_2 dipole trap, darker color corresponds to higher CO_2 laser power. Orange bars represent the imaging pulses, and yellow bar represents the coherent excitation RF pulse that starts the evolution.

After the sample is loaded to FORT, the magnetic field is raised to Feshbach resonance (around 832 G) so that the cloud can be cooled further using two evaporative processes: free evaporation (region 2) and forced evaporation (region 3). In region 2, full power CO_2 laser (output power 140 W) is used to create a dipole trap as introduced in Sec. 2.3.1, the intensity at beam focus is on an order of 10^6 W/cm^2. Because of the large Rayleigh length of this beam (~ 1 cm), the radial confinement of this trap is much larger than the axial one. At the end of free evaporation, the sample is a 50-50 incoherent mixture of two lowest hyperfine states $|1\rangle$ and $|2\rangle$, containing about 6×10^5 atoms per state. Region 3 shows the forced evaporation. In this process, the power of CO_2 laser is lowered adiabatically (denoted as lighter blue in Fig. 4.1) to about 0.015% from its maximum power, and atoms with higher energy escape from the trap during collisions, resulting in a very cold sample.

By that point, a degenerate Fermi cloud has been formed as an incoherent mixture of two spin states. To keep the atoms confined in the trap, CO_2 laser power is raised slowly up to 2% of its maximum value during region 4. All experiments of this chapter are conducted at this trap depth for different values of the magnetic field. To bring the sample down to the zero-crossing

magnetic field, one spin must be eliminated to avoid sample heating and atom loss when the magnetic field is swept through Feshbach resonance magnetic field. The elimination is done at ~ 1200 G, where the atoms are weakly interacting. I destroy all atoms in state $|1\rangle$ with a $17\,\mu$s imaging pulse shown at the end of region 5, which is on resonance with spin state $|1\rangle$. The calibration of this procedure is described in Sec. 4.3.1.

Now with only one spin state in the sample, the magnetic field is swept close to zero-crossing (527.15 G) so that both magnitude and sign of scattering length can be tuned during the experiment. As measured in Ref. Pegahan et al. (2019), scattering length changes with magnetic field at a rate of $\sim 3.14\,a_0$/G, which means that conducting experiments around zero-crossing requires decent stability in magnetic field. Therefore, after dropping the command current for the main magnet to change the magnetic field from ~ 1200 G to ~ 527 G, I wait for 3 s for the magnetic field to stabilize. This time is selected by monitoring the change of current in the main magnet powerline, which determines the magnetic field magnitude, over time. To measure the current, a Hall sensor is set up on the power cord which supplies the current to the main magnet coil, to measure current during experimental cycle in steps of 5 ms. Recording the current value for each experimental cycle allows to detect instabilities in the magnetic field if any.

After the magnetic field is stabilized at the value of interest, a coherent excitation RF $(\frac{\pi}{2})_y$ pulse (0.5 ms), resonant with $|2\rangle$ to $|1\rangle$ transition, is applied to the system to create a x-polarized sample. With the coherent mixture of these two states, the system starts to evolve under the effect of s-wave scattering. At this point, the cloud comprises about 3.2×10^4 atoms per spin state. After a desired evolution time, τ, absorption images of each spin are taken, separated by 10μm. With these images, integration across radial direction yields axial spatial profiles $n_1(x)$ and $n_2(x)$. With the technique of Abel inversion (introduced in Appendix B), the energy space profiles $n_1(E)$ and $n_2(E)$ of two spins are obtained from the measured spatial profiles.

The procedure described above is defined to be a complete experimental cycle that I refer to a single shot. When the spins are imaged, they are destroyed by the imaging pulses, and therefore, in each series of experiments, clouds will be prepared, destroyed, and the sequence repeated to average. To obtain ensemble averaged measurement of spatial density profiles, averaging over single shots is required. Note that, the spatial profiles have finite resolution, which means that the corresponding energy space profiles have finite resolution ΔE. In each energy group, ΔE is small enough such that all the atoms in this group evolve in a nearly identical way. Therefore, for each shot, the operator s_{zi} defined in Eq. 3.9 is measured for an ensemble of atoms in a selected energy group $E_i \in [E, E+\Delta E]$. With this understanding, it is clear that each single shot measurement of the spin density profiles yields the ensemble average of the spin operator s_{zi} on a system state, $\langle\psi|s_{zi}|\psi\rangle$.

4.2 Spin density evolution

In weakly interacting regime, the total spin density profile $n_1(x)+n_2(x)$ is expected to remain the same, but two spins evolve differently, since they have different magnetic moments. With the gradient of magnetic bowl potential along the longitudinal axis of the cloud, the oscillation frequencies of two spins differ by $\delta\omega_x$. This difference produces Zeeman precession and it causes the spin vectors for different energy groups to rotate at different rates around z-axis. In addition, the s-wave collision drives a rotation around the total collective spin vector $\vec{S}(E)$, and its evolution is represented by the coupling matrix $\tilde{g}(E',E)$, which is proportional to the mean field frequency Ω_{Fg}. The two terms in the system Hamiltonian resulting in these effects are called Zeeman term and mean-field term respectively. At the scattering length $a = 5\,a_0$, the magnitudes of these two terms are comparable. The detailed mathematical derivation and numerical scale are shown in Ch. 3.

4.2.1 Spin segregation

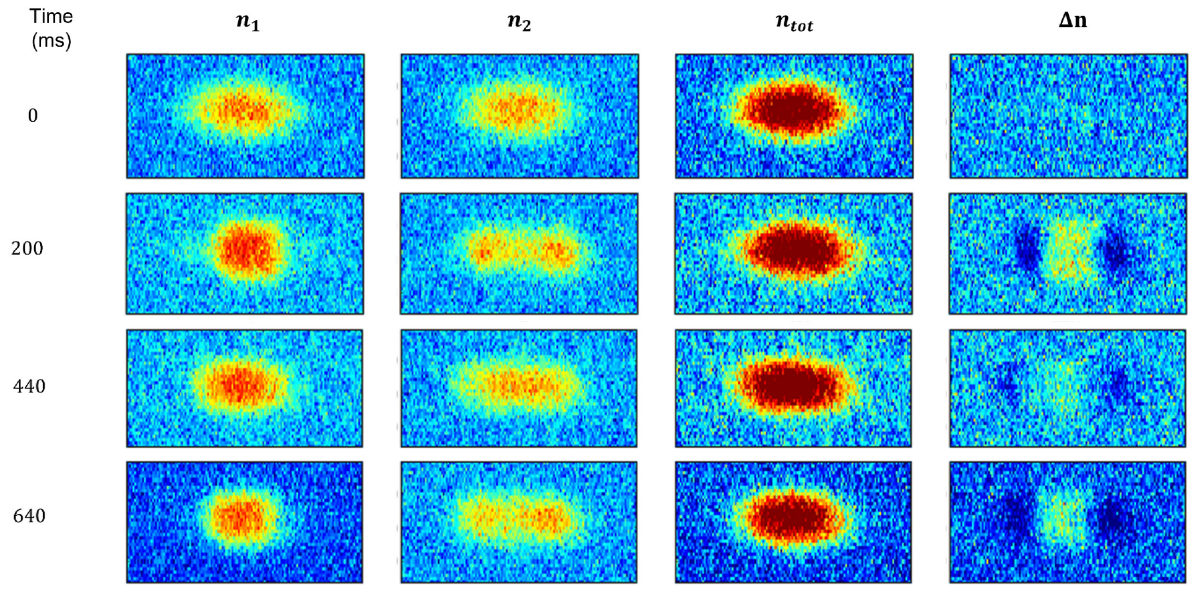

Figure 4.2: Spin evolution at $5\,a_0$ imaged at 0, 200, 440 and 640 ms evolution time relative to the coherent excitation pulse. The aspect ratio in this figure is adjusted to show the cloud shapes clearly, the real ratio of axial and radial size of the cloud is $\sim 26:1$. All panels share same color bar scale.

During the evolution described above, at a scattering length a, one spin state moves toward the edge of the harmonic trap, and the other spin state moves toward the center; with a flipped scattering length $-a$, the movement direction for each state is interchanged. This effect is called spin segregation, it was first observed in Ref. Du et al. (2008). Spin segregation is a result of the long-range coupling between atoms in energy space, and its evolution rate is proportional to the magnitude of scattering length.

Immediately after the coherent superposition state is created, spin segregation starts. In Fig. 4.2, time is relative to the $(\frac{\pi}{2})_y$ pulse. The four rows show the absorption images taken at different evolution times, and four columns show the spatial density for spin 1, n_2, spin 2, n_2, sum of them, $n_{tot} = n_1 + n_2$, and difference between them, $\Delta n = n_1 - n_2$. In the first row, where the system just started evolving, the profiles for two spins are identical, and the difference between them is, of course, zero. The second row, at 200 ms, is when two spins reach the most segregated stage for this scattering length. During evolution, two spins are less segregated at 440 ms and more segregated at 640 ms again. Note that, the total spatial profile n_{tot} remains the same, independent of the directions that the spins of atoms move spatially. This is a piece of strong evidence that there is no energy exchange happening, which means that the system is evolving in weakly interacting regime.

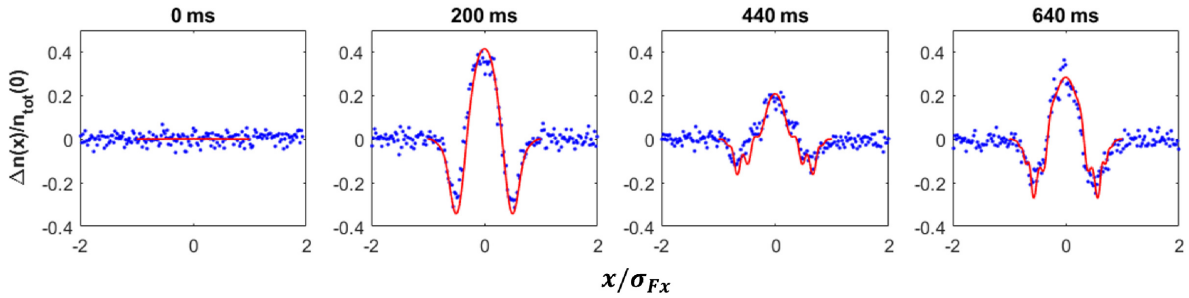

Figure 4.3: Normalized density difference, $\Delta n(x)/n_{tot}(0)$, at different evolution times. Blue dots are axial spatial profiles obtained by integrating density plots at corresponding evolution times in Fig. 4.2 over radial direction. Red curve is predicted by the mean-field model introduced in Ch. 3.

Since the axial size of the sample is about 26 times of the radial size, it is treated as a 1D cloud. To study the spin density, the axial profiles are of interest. Fig. 4.3 shows the normalized axial spatial profile $\Delta n(x)/n_{tot}(0)$ at corresponding evolution times in Fig. 4.2. Blue dots are obtained by integrating the density at all pixels over radial direction. Red curve is generated by the model with numerical values derived in Ch. 3. This normalized density difference is

directly proportional to z-component of the spin vector: $s_z = \frac{1}{2}\Delta n/n_{tot}(0)$. Normalization is done by dividing the density by the peak total density $n_{tot} = n_1(0) + n_2(0)$. The axial dimension of the cloud, x, is scaled by dividing the Thomas-Fermi width, $x/\sigma_{Fx} \in [0,1]$: $x/\sigma_{Fx} = 0$ at the center of the cloud and $x/\sigma_{Fx} = 1$ at the cutoff of Thomas-Fermi fit for total density profile $n_1(x) + n_2(x)$. A more detailed description of data processing procedure will be given in Appendix A.

To quantify the degree of segregation of the system at different evolution times, a concept of "central spin density" is defined as the value of $\Delta n(0)/n_{tot}(0)$ at cloud center. Observing Fig. 4.3, larger central spin density means the system is more segregated. Immediately after the coherent excitation pulse, the central spin density is zero in theory.

4.2.2 Central spin density oscillation amplitude decay

With the concept of central spin density defined, the status of the system can be probed by keeping track of the central spin density evolution over time. Previously, this experiment was conducted in Ref. Pegahan et al. (2019), and an anomalous decay in the oscillation amplitude was observed, which was not predicted by the model. It was believed that the decay was a result of the averaging over several runs with shot-to-shot variation in atom density. However, by implementing the experiment and analyzing data myself, I doubt this conclusion.

In all experiments described in this dissertation, samples are destroyed during the imaging process as mentioned in Sec. 4.1. There are about 400 data points in this experiment, and therefore 400 samples are prepared. Although the preparation method described in Sec. 4.1 is the same for all samples, experimental parameters such as σ_{Fx} and N are not perfectly controlled. The standard deviation in atom number is about 8% and that in the cloud size is about 3%. However, even with such small variations, the modeled central spin density evolution curves show pronounced differences in both oscillation amplitude and frequency as shown in Fig. 4.4. By simply modeling this evolution, the data is expected to show a variation comparable to the modeled central spin density oscillation amplitude for later evolution time since they are sensitive to the variation in mean field frequency Ω_{Fg}, and therefore, cloud density fluctuation.

To test the hypothesis about the decay mechanism in central spin density oscillation amplitude proposed in Ref. Pegahan et al. (2019), I investigate the evolution of central spin density by repeating spin segregation experiments for different evolution times τ. I conduct the experiment at $5.19\,a_0$, with images taken from $\tau = 0$ ms to $\tau = 3600$ ms with a step size of 40 ms in random order. I take 6 shots for each time point. I plot all single shot data in Fig. 4.5 (a) (blue circles) instead of only the average of them to see the distribution. In the same panel, black dashed curve is the central spin density evolution predicted by the model using one

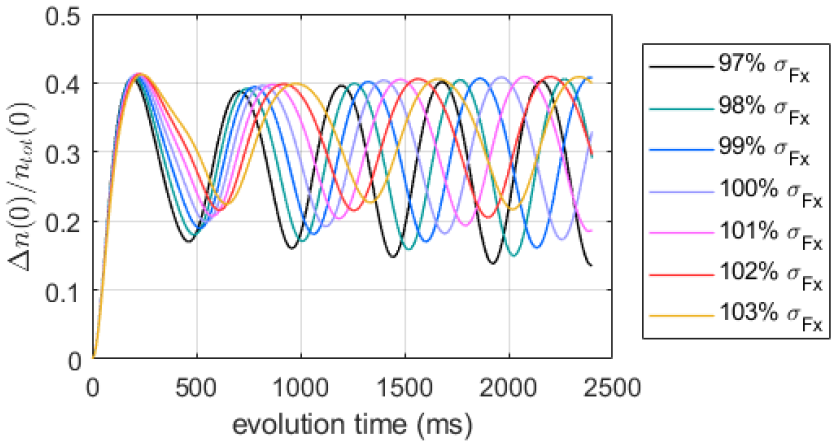

Figure 4.4: Modeled curve of central spin density evolution with fixed atom number $N = 60000$, but vary cloud size $\sigma_{Fx} = 320\,\mu m$ from 97% σ_{Fx} to 103% σ_{Fx} with a step size of 1% σ_{Fx}.

set of parameters σ_{Fx} and N which is averaged over all 400 shots (σ_{Fx} and N_1/N_2 ratio are lowered by 2.5% and 3% respectively to fit data better). The model predicts a large amplitude oscillation throughout the 3.6 s evolution time without decaying, however, the data shows that the oscillation is not noticeable after about 1 s. Also, note that the spread of data for a fixed evolution time is much smaller than the model-predicted oscillation amplitude. In panel (b), the red stars are predicted by the model at different evolution times using σ_{Fx} and N extracted from single-shot data at corresponding times, which means that there are 400 data points (blue circles) in (a), and therefore there are 400 red stars that have 1-to-1 correspondence to them. The spread of the red stars matches the oscillation amplitude of the black curve predicted by model using one averaged set of parameters, and this variation is much larger than the variation in real data shown in (a). (a) and (b) compare the individual shots behavior of model and data, and in (c), I compare the average. Blue circles are averaged over 6 data points at the same evolution time. Red curve is an average of 400 central spin density evolution curves predicted by the model using 400 pairs of σ_{Fx} and N extracted from each single shot data. Averaging result in (c) suggests that with such method of averaging, data and model agree. However, the distribution discrepancy shown in (a) and (b) is not negligible.

4.2.3 Central spin density distribution at longer time

In the experiment presented in Fig. 4.5, I only take 6 shots at each evolution time, which is not optimum for a study of distributions since the sample size is too small. To determine the proper sample size, I use the sample size estimation formula for two-sample t-test, which is a statistical method to compare mean values of two groups: hypothesis (model) group and

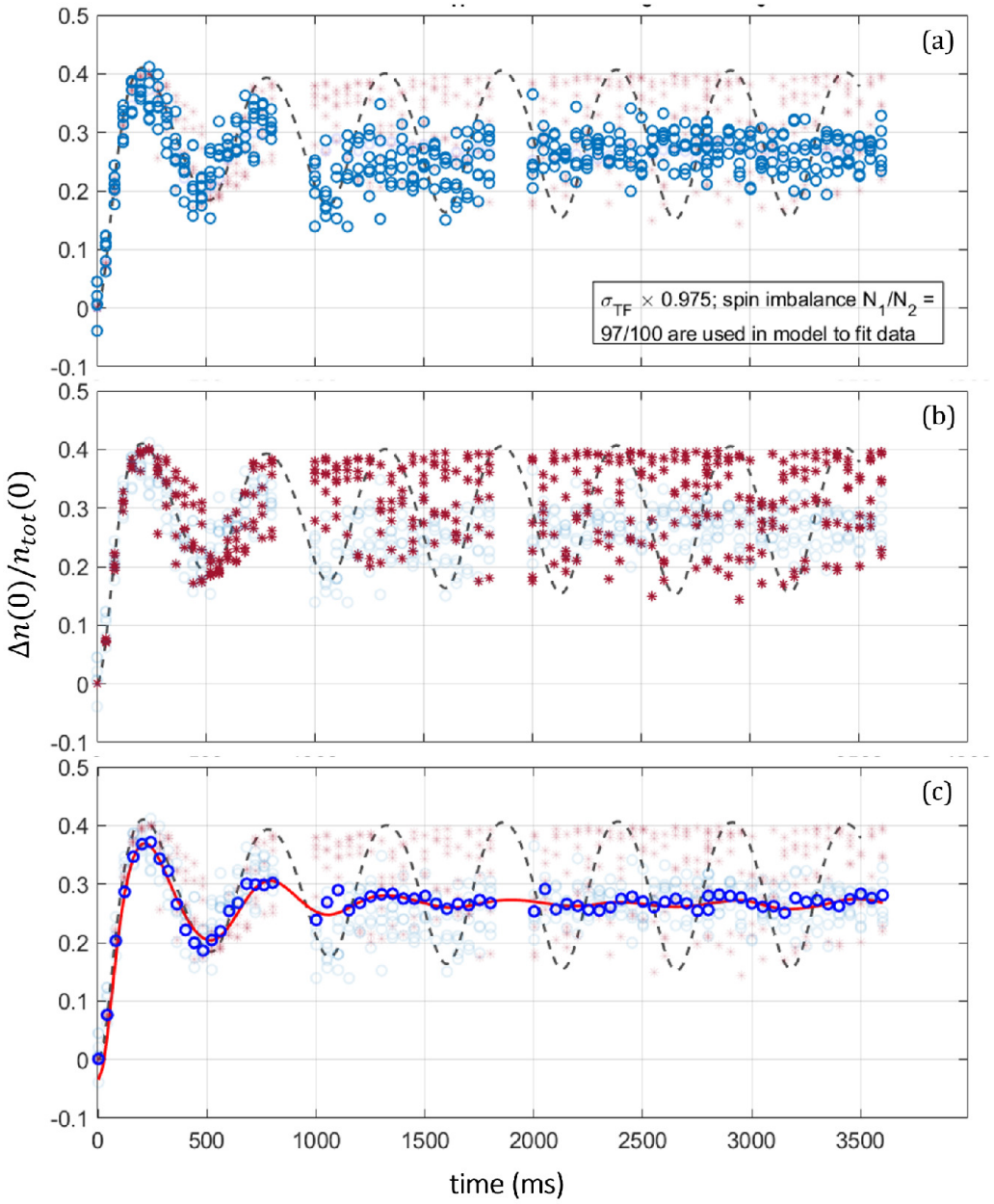

Figure 4.5: Central spin density evolution over time. Spin segregation performed at 5.19 a_0. (a) Blue circles are extracted from single shot data at different evolution times, black dashed curve is model prediction using averaged Thomas-Fermi cloud size σ_{Fx} and atom number N. (b) Red stars are central spin density predicted by the model using σ_{Fx} and N extracted from individual shots at corresponding evolution time. (c) Blue circles are averaged central spin density at different evolution times. The red curve is the average of 400 predicted evolution curves using all pairs of experimental parameters extracted from single shot data across the whole data set.

experimental (data) group.

Sample size determination

Before implementing the experiment to study the distribution, the sample size needs to be determined in advance. To find the sample size which is sufficient for a two-sample t-test, a rough estimation in mean and variance for both hypothesis group and experimental group is required. They can be calculated using the data section with evolution time $t \in [1, 3.6]$ (306 points in total) from data set shown in Fig. 4.5, where the central spin density evolves close to the static offset. I extract their atom number N and cloud size σ_{Fx}, as well as their central spin density $\Delta n(0)/n_{tot}(0)$. The histogram for extracted central spin density is plotted in Fig. 4.6 in blue bars.

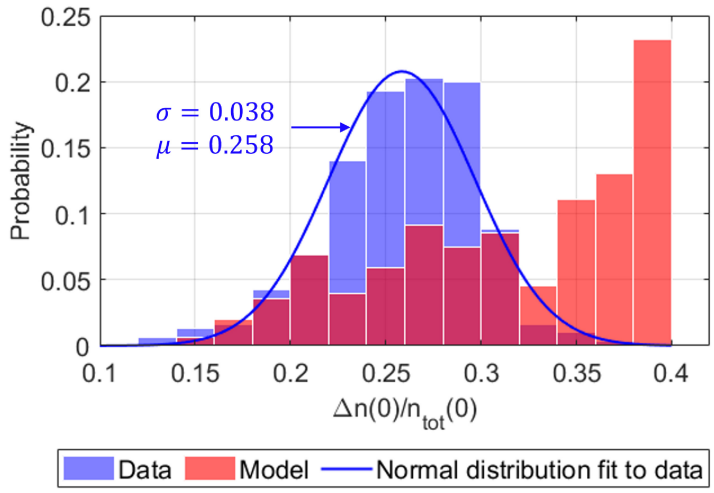

Figure 4.6: Distribution of central spin density for data taken from 1 s to 3.6 s in Fig. 4.5 (blue) and for model prediction (red) using experimental parameter pairs σ_{Fx} and N extracted from all single shots in this data range.

This distribution of data can be fitted by a normal distribution:

$$f(x) = \frac{1}{\sigma\sqrt{(2\pi)}} e^{-\frac{1}{2}\left(\frac{x-\mu}{\sigma}\right)^2}.$$

The fitted standard deviation for this data set is $\sigma_d = 0.038$ and mean $\mu_d = 0.258$.

I use the extracted σ_{Fx} and N for each shot and the corresponding evolution time to model the central spin density, whose histogram is plotted in red bars in Fig. 4.6. Note that the modeled

central spin density doesn't have a normal distribution, but the distribution type is not very critical for the purpose of estimating the sample size for hypothesis test. In fact, when the experimental group and hypothesis group have different distributions, the hypothesis test is harder to fail. The mean of central spin density predicted by the model is $\mu_m = 0.315$, and I take the variance to be double the experimental value to be safe, as the modeled central spin density is more has broader distribution compared to the data, which gives $\sigma_m = 0.076$.

With σ_d, μ_d, σ_m and μ_m estimated above, the required sample size is calculated from the formula for two-sample t-test:

$$n_g = (Z(\alpha/2) + Z(\beta))^2 \frac{\sigma_m^2 + \sigma_d^2}{(\mu_m - \mu_d)^2}. \tag{4.1}$$

$Z(*)$ is called critical value of the value $*$. For example, look at the normal distribution with mean $= 0$ and variance $= 1$ shown in Fig. 4.7, $Z(A)$ is a value such that the shaded area under the curve for $x \in [-Z(A), Z(A)]$ is A. In terms of probability, if the area A is $p\%$ of the total area under this normal distribution curve, then the probability of observing a value of x out of the range $[-Z(A), Z(A)]$ is $1-p\%$.

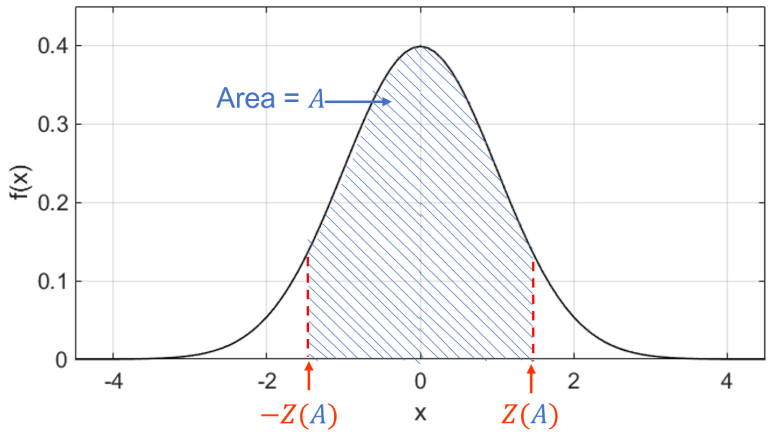

Figure 4.7: Normal distribution defined by $\sigma = 1$, $\mu = 0$.

Define null hypothesis as: data and model have same distribution. α is the probability of the test rejecting the null hypothesis when null hypothesis is true, so it's a type of possible error in the test. β is the probability of the test failing to reject the null hypothesis while hypothesis is false so it is another type of possible error in the test. For the hypothesis and data that do not have extremely close distribution and mean, standard numbers adopted in statistics are $\alpha = 0.05$ and $\beta = 0.2$. These correspond to $Z(\alpha/2) = 1.96$ and $Z(\beta) = 0.84$.

With all numbers introduced above, the sample size calculated from Eq. 4.1 is 20. I treat an average of 6 shots as one reliable sample, therefore, 120 shots are confirmed to be sufficient to perform the hypothesis test for the model with experimental data. To be safe, I take 160 data shots instead of 120 for each experimental group, and generate 160 corresponding model points as the hypothesis group.

Modelling

The method of generating model points for central spin density is not obvious. I describe the method I adopt in detail in this subsection. For an example, I take 160 data shots for evolution time $t = 1.5$ s. I extract N and σ_{Fx} from each shot, and plot the histograms of them in Fig. 4.8.

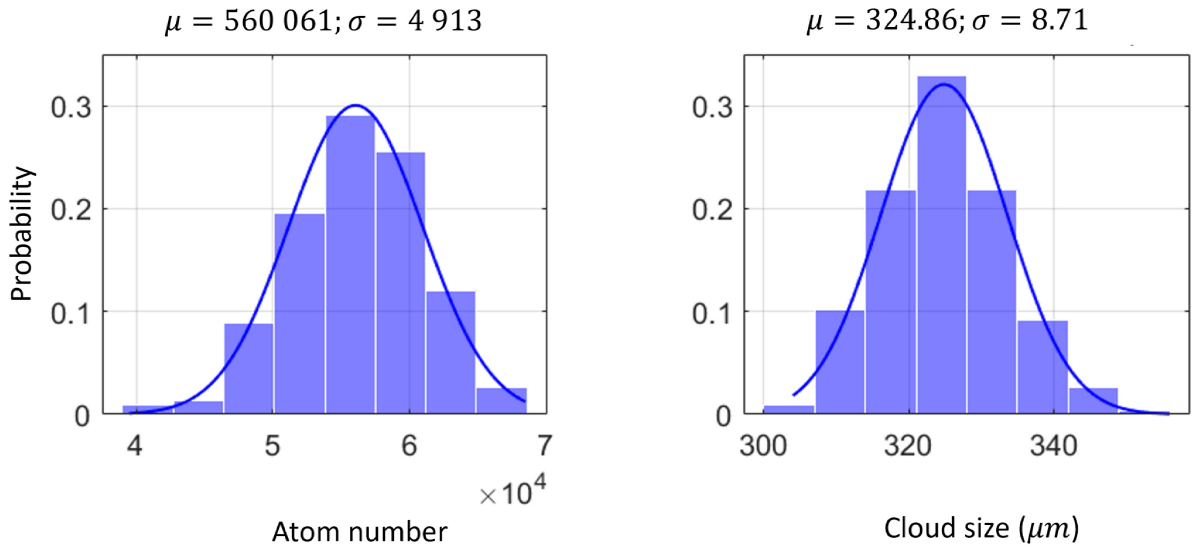

Figure 4.8: Distribution of atom number and cloud size extracted from data taken at 1.5 s evolution time (blue bars) and their normal distribution fit (blue curves). Each standard deviation σ and mean μ are shown on top of the figure.

Since the evolution rate scales linearly with cloud density, but scales as the inverse cube of the cloud size, I expect that the variation in cloud size impacts the distribution of central spin density much more than the atom number. Therefore, while modeling, I only use average atom number for the data set to avoid the false counting in atom number due to imaging problems and use various cloud sizes. I extract the normal distribution fitted to σ_{Fx} histogram as shown in the right figure in Fig. 4.8, and generate a set of $\sigma_{Fx,m}$ (containing 160 points, same as number of data) with normal distribution using same parameters: $\sigma = 8.71$ and $\mu = 324.86$. This way, I

avoid artifacts while fitting σ_{Fx} with Thomas Fermi profile. The erros in atom number counting and profile fitting described above happens occasionally while processing large data sets. With the mean atom number directly obtained from the data set and the generated $\sigma_{Fx,m}$, I run the model for the evolution time which matches the data set, and calculate the same number of central spin densities as the data set. Then, by plotting the histogram for modelled group and data group, I compare the distributions of them.

Experiment

To do the statistics and extract distribution information, I choose evolution times where the data is sensitive to the initial conditions σ_{Fx} and N: 1.5, 2.5, 3.5, and 5 s relative to the coherent excitation point. For each evolution time, I keep experimental procedure the same, and take 160 shots to achieve a large enough sample size, and plot the histogram of central spin density in blue bars shown in Fig. 4.9.

To compare to the model, I extract σ_{Fx} and N from all shots for each data set, and use them to generate modeling parameters with the method described in **Modelling** part so that the initial conditions that go into the model are as close as they can be to reality. The histogram of modeled central spin density is plotted in red bars in Fig. 4.9. These figures suggest that the distribution of modeled $\Delta n(0)/n_{tot}(0)$ always skews towards to a higher value. This can be understood by looking at Fig. 4.4: with the same atom number, the modeled central spin density oscillation curve with different σ_{Fx} has close maximum values but different minimum values and oscillation frequencies. Therefore, for a collection of these curves with a normal distribution of σ_{Fx}, the distribution of the central spin density value at a fixed evolution time should favor a higher value close to 0.4, agreeing with the distribution of modeled central spin density in Fig. 4.9. However, the histogram extracted from data always has a normal distribution. The spread of the data is smaller than that of the model. Note that the discrepancies observed in both the mean and spread of the distribution match the phenomenon revealed by the central spin density evolution experiment shown in Fig. 4.5 (the mean of modeled points is higher than that of the data and the distribution for the modeled points is wider than that of the data). One can also notice that the center of the normal fit to data shifts toward higher value over time, and gets closer to the model at 5 s, although the data distribution is still not as asymmetric as the model and the spread of the data is much narrower than the model. Since the coherent time scale for this experimental system is found to be close to 5 s, the result from experiment with longer evolution time exceeding this scale is not reliable.

The result of this statistical study suggests that multiple modes might govern the evolution of experimental system while the model only predicts one oscillating mode. At long evolution time, the oscillating mode(s) decays and static mode(s) remains the same in the data. Lacking

the static modes, the model only predicts a nondecaying oscillating mode. By averaging over a number of shots with a variation in cloud densities, the model tends to predict an oscillation curve with a higher offset than that of the data.

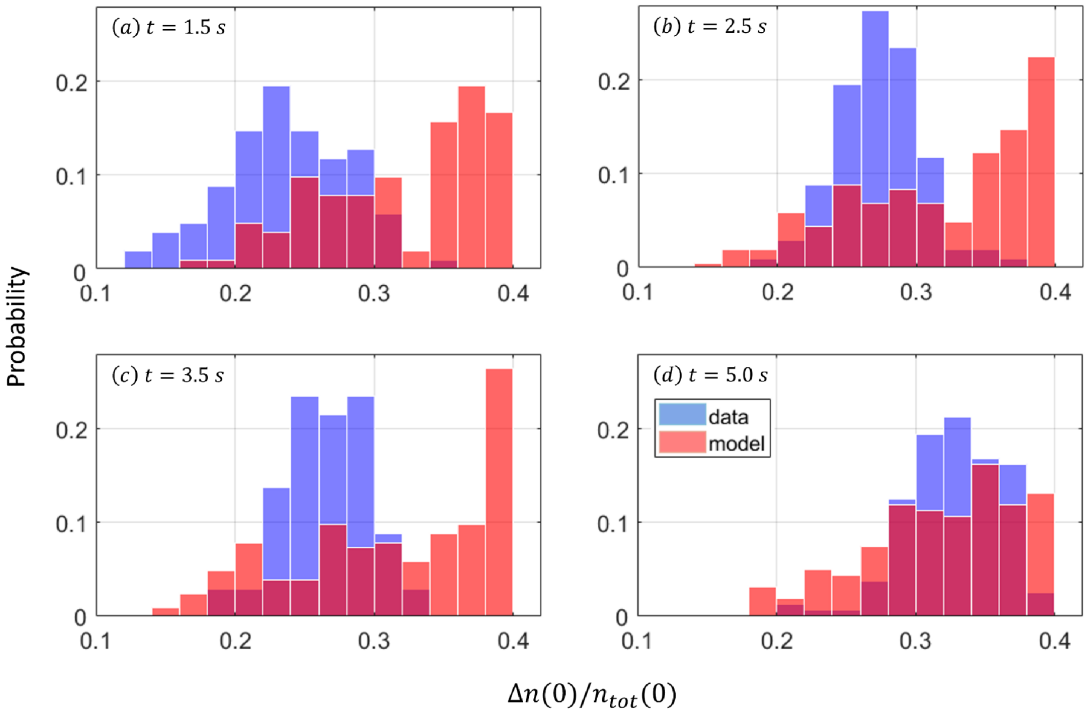

Figure 4.9: The distribution of central spin density at different evolution times. Blue is extracted from 160 data points, red is generated by model with the method described in **Modelling** part.

To investigate more about the multi-mode hypothesis, Hamiltonian reversal experiments might be helpful. In such experiments, instead of studying the distribution depending on cloud densities, the sensitivity to cloud initial conditions is suppressed therefore the reversibility of the modes can be studied reliably. This way, the sources of decay in oscillating mode can be studied.

4.3 Basic calibrations

To guarantee that the system evolves with desired condition, several basic calibrations are needed before data collection. Since the experiments are conducted in a weakly interacting

regime, the temperature and magnetic field magnitude are critical. The degeneracy needs to be ensured to avoid the energy tuning of the scattering length. The scattering length changes with magnetic filed at a rate of $a = 3.14(B - B_0)\,a_0$ and the scattering I work at in this dissertation is mainly at $5\,a_0$, so $B - B_0$ needs to be well controlled. In this section, I introduce calibration procedures to assure the degeneracy of the sample and precission of magnetic field.

4.3.1 Calibration of spin state elimination method

The temperature of the cloud is obtained by fitting the axial spatial profile of the cloud with finite temperature Thomas-Fermi function, in units of T/T_F. The typical sample temperature for experiments in this dissertation is $\approx 0.3\ T/T_F$, the corresponding finite temperature Thomas-Fermi width of the cloud σ_{Fx} is about $340\,\mu m$ for a total atom number of 6.5×10^5. This is mainly achieved by evaporative procedures introduced in Sec. 4.1. However, an improper spin state elimination at 1200 G can heat up the cloud even if a required low temperature is achieved after the forced evaporation. Suppose the pulse intensity is fixed for imaging purpose, if the pulse duration is too long, it might affect spin $|2\rangle$ while removing spin $|1\rangle$; if the pulse duration is too short, there is still spin $|1\rangle$ remaining in the sample, and while sweeping magnetic field down to zero-crossing, two spins interact strongly when it reaches Feshbach resonance magnetic field. This interaction heats up the sample. Hence, the pulse duration needs to be calibrated.

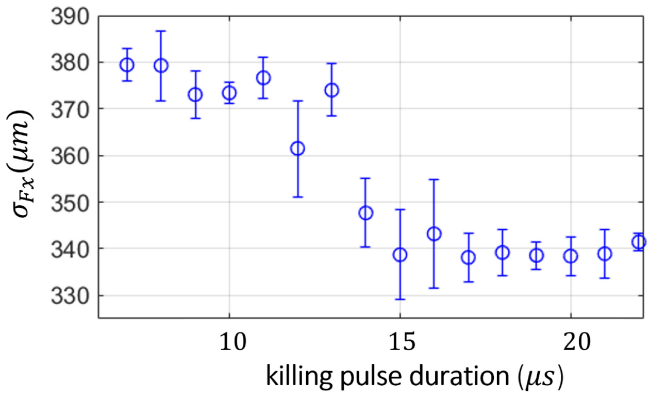

Figure 4.10: Cloud size after sweeping the magnetic field close to zero-crossing as a function of state $|1\rangle$ elimination pulse duration. 6 shots are taken for each pulse duration.

To find the right pulse duration, I conduct the sequence introduced in Sec. 4.1, but without the RF pulse and $\tau = 0$ ms with different pulse duration for the spin elimination imaging pulse from $7\,\mu$s to $22\,\mu$s. This means the sample is prepared and cooled after forced evaporation the

same way, and spin $|1\rangle$ is eliminated differently. At the end, after the magnetic field is swept back to close to 528 G, state $|2\rangle$ is imaged and fitted with zero-temperature Thomas-Fermi profile to obtain σ_{Fx}. The fitted σ_{Fx} as a function of elimination pulse duration is shown in Fig. 4.10.

This calibration suggests that at this intensity, a 17μs killing pulse is safe to obtain a good elimination result. In all experiments in this dissertation, this combination of pulse intensity and duration is adopted.

4.3.2 Calibration of magnetic field

To achieve different scattering lengths, the magnetic fields need to be measured precisely. The energy difference in two states of the sample has one-to-one correspondence to the magnetic field. Therefore, using the resonance frequency of RF pulse for this transition, the field can be calibrated.

As shown in Ref. Zhang (2013), the transfer rate from state $|2\rangle$ to state $|1\rangle$ has a form:

$$\left|\frac{N_1}{N_{tot}}\right|^2 = \frac{1}{1+\frac{\Delta^2}{\Omega^2}} \sin^2\left(\frac{\Omega t}{2}\sqrt{1+\frac{\Delta^2}{\Omega^2}}\right), \tag{4.2}$$

where Ω is the Rabi frequency. Δ/Ω is a dimensionless detuning from the bare atomic transition, and when $\Omega t = \pi$, $\Delta = 0$ yields a full transition from state $|2\rangle$ to $|1\rangle$.

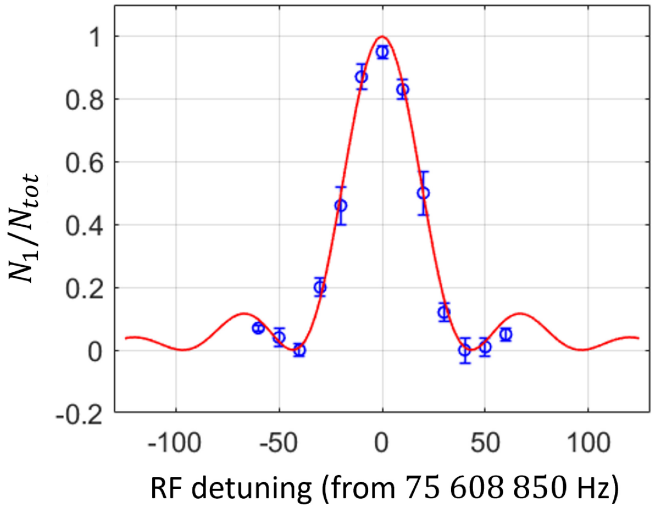

Figure 4.11: Atom transferred from state $|2\rangle$ to $|1\rangle$ as a function of RF detuning from the resonant frequency 75 608 850 Hz. The RF pulse width adopted here is 15 ms.

To measure the magnetic field precisely, apply a 15 ms π pulse at magnetic field of interest with slightly different RF frequencies, and image both spins to extract atom number information. In Fig. 4.11, blue dots show the ratio of atom number transferred from state $|2\rangle$ to state $|1\rangle$ as a function of RF detuning in unit of Hz. Red curve is generated using Eq. 4.2. The result suggests that the resonance frequency is 75.60885 MHz and the corresponding magnetic field is $B = 528.803$ G, giving a scattering length $a = 5.19\, a_0$.

In this dissertation, all magnetic fields adopted for implementing experiments are measured by doing RF spectra using the method introduced in this section.

CHAPTER

5

QUANTUM REWINDING

In this chapter, I study the reversibility of the Hamiltonian of a large many-body system. By observing the reversal behavior at different scattering lengths and for different forward evolution times, I probe the reversibility of this experimental system and search for clues of the potential missing piece in the mean-field model.

Anomalous behaviors in central spin density evolution are observed during the experiments, suggesting the existence of multiple modes in the central spin density evolution model predicted by the mean-field model described in Ch. 3. I quantify how well the system is reversed with a certain set of experimental parameters by comparing the spin density spatial profiles of z-component of the spin vector during forward evolution and backward evolution quantitatively. With this technique, a series of precise measurements are implemented at two regimes to find the zero-crossing magnetic field for ^{6}Li $|1\rangle$-$|2\rangle$ mixture.

5.1 Experimental protocol

The protocol adopted to invert the Hamiltonian is demonstrated in Fig. 5.1. The sample of $|1\rangle$ and $|2\rangle$ mixture is prepared as described in Sec. 4.1 and $|1\rangle$ is eliminated at $1200G$ to give us a z-polarized initial state $|\psi_{0z}\rangle$. A coherent excitation $(\frac{\pi}{2})_y$ RF pulse is applied to give an x-polarized state: $|\psi_{0x}\rangle = e^{-i\frac{\pi}{2}S_y}|\psi_{0z}\rangle$. With the 50-50 superposition state, the system starts

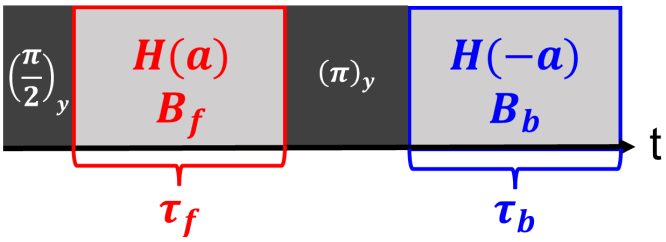

Figure 5.1: Experimental sequence to implement Hamiltonian reversal. Black blocks represent RF pulses around y-axis, and grey blocks represent system evolution. Red corresponds to forward evolution and blue corresponds to backward evolution.

evolving at magnetic field B_f that corresponds to scattering length a for time τ_f. I extract the z-component of spin vector at different forward evolution times $t_{fk} \leq \tau_f$ by imaging both spins at t_{fk}. Up to this point, the experimental procedure is the same as the simple spin segregation experiment described in Sec. 4.1. After the desired length of forward evolution, I invert the sign of Hamiltonian by applying a π_y pulse and sweeping magnetic field to B_b that gives scattering length $-a$ with a pair of auxiliary coils. The calibration of the auxiliary coils is described in Sec. 5.5. Ideally from now on, it's equivalent to making the system evolve backward in time, and after a time period $\tau_b = \tau_f$, the system is expected to evolve back to its non-segregated state. As for the forward evolution, the S_z vector can be observed at different τ_{bk} by imaging both spins at different times.

5.2 Mathematical derivation

To illustrate how the combination of π_y pulse and scattering length flipping inverts the sign of Hamiltonian, I derive the final state after applying the experimental sequence shown in Fig. 5.1 in quantum picture in this section.

I modify Eq. 3.25 by assuming finite resolution ΔE in energy space, such that $E_i \in [E, E+\Delta E]$ and $E_j \in [E', E'+\Delta E]$; it's convenient to write $g(E, E') \rightarrow g_{ij}$, $\Omega_z(E) \rightarrow \Omega_{zi}$, and $\vec{s}(E) \rightarrow \vec{s}_i$. Then the system Hamiltonian of the 1D energy lattice has the form:

$$\frac{H(a)}{\hbar} = \sum_{i,j\neq i} g_{ij} \vec{s}_i \cdot \vec{s}_j + \sum_i \Omega_{zi} s_{zi}, \tag{5.1}$$

H is written as $H(a)$ to remind reader about the sign of mean field term lead by g_{ij}.

The final state after applying the sequence in Fig. 5.1 can be written as:

$$|\psi_f\rangle = e^{-\frac{i}{\hbar}H(-a)\tau_b} e^{-i\pi S_y} e^{-\frac{i}{\hbar}H(a)\tau_f} |\psi_{0x}\rangle. \tag{5.2}$$

Inserting an identity operator $\mathbb{1} = e^{-i\pi S_y} e^{i\pi S_y}$:

$$|\psi_f\rangle = e^{-i\pi S_y} e^{i\pi S_y} e^{-\frac{i}{\hbar}H(-a)\tau_b} e^{-i\pi S_y} e^{-\frac{i}{\hbar}H(a)\tau_f} |\psi_{0x}\rangle,$$

and with Eq. 5.1, the Hamiltonian after a general rotation θ_y can be written as:

$$\begin{aligned} & e^{i\theta S_y} \frac{H(-a)}{\hbar} e^{-i\theta S_y} \\ =& -a \sum_{j\neq i} g_{ij} \vec{s}_i \cdot \vec{s}_j + \Omega_{zi} \underbrace{e^{i\theta S_y} s_{zi} e^{-i\theta S_y}}_{\hat{O} \equiv s_{zi}(\theta)}. \end{aligned}$$

With Heisenberg equation of motion,

$$\begin{aligned} \frac{d\hat{O}}{d\theta} &= i e^{i\theta S_y} [S_y, s_{zi}] e^{-i\theta S_y} = -e^{i\theta S_y} s_{xi} e^{-i\theta S_y} \equiv -s_{xi}(\theta) \\ \frac{d^2\hat{O}}{d\theta^2} &= -i e^{i\theta S_y} [S_y, s_{xi}] e^{-i\theta S_y} = e^{i\theta S_y} s_{zi} e^{-i\theta S_y} = s_{zi}(\theta) \\ &\Rightarrow \frac{d^2\hat{O}}{d\theta^2} + \hat{O} = 0 \quad \text{with initial conditions: } \begin{cases} \hat{O}(0) & = s_{zi} \\ \frac{d\hat{O}}{d\theta}|_0 & = -s_{xi}. \end{cases} \end{aligned}$$

The solution to this differential equation has this analytic form:

$$s_{zi}(\theta) = \cos\theta\, s_{zi} - \sin\theta\, s_{xi}. \tag{5.3}$$

With this solution, the π_y rotation to the Hamiltonian can be written as:

$$\begin{aligned} e^{i\pi S_y} \frac{H(-a)}{\hbar} e^{-i\pi S_y} &= -a \sum_{j\neq i} g_{ij} \vec{s}_i \cdot \vec{s}_j + \Omega_{zi}(-s_{zi}) \\ &= -\frac{H(a)}{\hbar}. \end{aligned}$$

This derivation shows that the combination of a π_y pulse plus flipping the sign of scattering length a achieves the Hamiltonian reversal, and therefore, the final state after the sequence

shown in Fig. 5.1 with $\tau_b = \tau_f = \tau$ is:

$$\begin{aligned} |\psi_f\rangle &= e^{-i\pi S_y} e^{-i(-H(a))\tau} e^{-\frac{i}{\hbar}H(a)\tau} |\psi_{0x}\rangle \\ &= e^{-i\pi S_y} |\psi_{0x}\rangle. \end{aligned}$$

Since $|\psi_{0x}\rangle$ is 50-50 superposition state with two unsegregated Thomas-Fermi shape clouds for two spin states, $|\psi_f\rangle$ should display the same shape for two clouds.

5.3 Quantification of reversal result

Hamiltonian reversal behavior can be observed clearly by comparing the central spin density evolution curves for forward and backward evolution as described in Sec. 5.4. However, if one wants to compare the quality of reversal for a series of very close experimental parameters, a more rigorous quantification of reversal results is required. In this section, I introduce my method and results for quantifying Hamiltonian reversal and utilize it to find the zero-crossing magnetic field.

5.3.1 χ^2 test

A complete data series for the purpose of examining how well the system is reversed with a certain set of experimental parameters is formed by two parts:

1. Spin segregation experiment done at forward evolution magnetic field B_f with spin density spatial profile $S_{zf}(x, t_k)$ measured at different evolution times t_{fk};

2. Hamiltonian reversal experiment with forward evolution time τ_f relative to the coherent excitation pulse, with $S_{zb}(x, t_k)$ measured at different backward evolution time τ_{bk}.

With the data series implemented as described above, the quality of Hamiltonian reversal can be quantified.

Forward evolution spin density spatial profiles $S_{zf}(x)$ at different $t_k \equiv t_{fk}$ are obtained by repeating spin segregation experiments without inverting the Hamiltonian, and backward evolution ones are obtained by doing Hamiltonian reversal experiments with the same τ_f but different τ_{bk} to match the corresponding forward evolution time. Profiles, $S_{zb}(x, t_k)$, for backward evolution data taken at different total evolution times $t_{bk} = \tau_f + \tau_{bk} = t_k + 2\tau_{bk}$ are compared with the profiles, $S_{zf}(x, t_k)$, for forward evolution $t_{fk} = \tau_f - \tau_{bk} \equiv t_k$.

Fig. 5.2 shows an example of $S_z(x, t_k)$ profiles for Hamiltonian reversal done at 8.05 a_0 scattering length with $\tau_f = 280$ ms (top row) and $\tau_f = 400$ ms (bottom row). Forward evolution $S_{zf}(x, t_k)$ is plotted with red circles and backward evolution $S_{zb}(x, t_k)$ is plotted with blue ones.

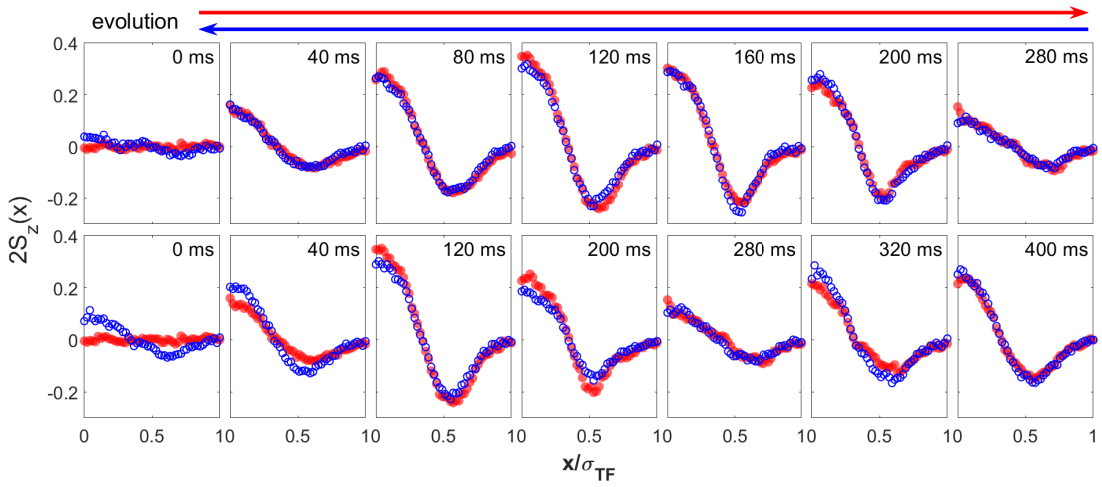

Figure 5.2: Compare spin density spatial profiles for forward and backward evolution at different times to examine the quality of Hamiltonian reversal. Red circles are forward evolution data and blue circles are backward evolution ones. The top row shows the result of doing Hamiltonian reversal at 8 a_0 and $\tau_f = 280$ ms and bottom row shows the result of it done at same scattering length but $\tau_f = 400$ ms. Time t_k shown on top right corner of each tile is the forward evolution time, i.e., $t_k \in [0, \tau_f]$. For the forward evolution data, total evolution time $t_{fk} = t_k$; for the backward evolution data, total evolution time $t_{bk} = \tau_f + (\tau_f - t_k)$ to match the profile at corresponding t_{fk} ($\tau_{bk} = \tau_f - t_k$ is the backward evolution time).

From this figure, it is obvious that the system is reversed better for the set of data where the Hamiltonian is reversed at 280 ms than for the 400 ms one, as the agreement between the corresponding forward and backward spin density profiles for $\tau_f = 280$ ms is much better than for $\tau = 400$ ms.

Eqn. 5.4 defines χ_k^2, the normalized mean square difference between forward and backward evolution spin density profiles for t_k. I take the difference between forward and backward evolution spin density spatial profiles at corresponding times ($t_k \equiv t_{fk} = t_{bk} - 2\tau_{bk}$), and then normalize the difference by dividing the forward evolution profile point-by-point. to make sure this difference is positive so that all of them are taken into count:

$$\chi_k^2 = \sum_x \left(\frac{S_{zb}(x, t_k) - S_{zf}(x, t_k)}{S_{zf}(x, t_k)} \right)^2 \tag{5.4}$$

Finally, I obtain a number, $\chi^2 \equiv \langle \chi_k^2 \rangle$, to quantify the reversal by averaging χ_k^2 for all t_k. With this technique, the quality of reversal for a certain set of B_f, B_b, and τ_f can be examined: small χ^2 means forward and backward $S_z(x)$ profiles overlap very well, corresponds to a good reversal.

5.3.2 Zero-crossing B-field measurement

Experiments that contain Hamiltonian reversal in their sequences, such as out-of-time order correlation (OTOC) and dynamical decoupling pulse sequence, are used to study dephasing, decoherent, and correlation (Lewis-Swan et al. 2019). A critical constant for the implementation of such experiments in a weakly interacting Fermi gas is the zero-crossing magnetic field B_0 where scattering length vanishes. A precise calibration of this field ensures the Hamiltonian is reversed properly during experiments. It is also crucial for studies at strongly interacting regime (O'Hara et al. 2002; Bloch et al. 2012) as it determines the shape of Feshbach resonance (Bartenstein et al. 2005; Zürn et al. 2013). In this section, zero-crossing magnetic field is measured by applying the quantification method introduced in Sec. 5.3.1 to experimental results of two series of Hamiltonian reversal with two distinct forward evolution magnetic fields $B_f = 528.803\ G$ and $529.713\ G$, (close to 5 a_0 and 8 a_0 respectively) and five slightly different backward evolution magnetic fields B_b for each B_f.

The magnitudes of all magnetic fields need to be measured precisely, which is done carefully by doing RF spectroscopy introduced in Sec. 4.3.2. By fitting χ^2 for five B_b with a parabola, the optimum reversal magnetic field $B_{b,opt}$ is obtained. The zero-crossing magnetic field is located at the midpoint between B_f and $B_{b,opt}$. Fig. 5.3 presents the result of this measurement. The top two figures (a) and (b) are the result of data series taken at $\pm 5.19\ a_0$ with Hamiltonian reversal done at $\tau_f = 400$ ms, and bottom two (c) and (d) are the result of $\pm 8.05\ a_0$ with Hamiltonian reversal done at $\tau_f = 240$ ms. The parabola fitting to χ^2 of $\pm 5.19\ a_0$ series suggests that $B_{b,opt} = 525.488$ G for $B_f = 528.803$ G, and it of $\pm 8.05\ a_0$ suggests that $B_{b,opt} = 524.596\ G$ for $B_f = 529.713$ G. Two series of experiments yield the result $B_0 = 527.150(5)$ G, which is 30 mG lower than the result reported before. Note that the scattering lengths $5.2\,a_0$ and $8.0\,a_0$ given above are calculated based on the zero-crossing magnetic field measured in this section.

The result reported by our group previously was obtained by comparing the axial sizes of each spin at different evolution times (Pegahan et al. 2019). This method requires a fitting of zero-temperature Thomas-Fermi function to two spins at different magnetic fields. With the presence of non-zero scattering length, neither spin has Thomas Fermi profile, so the obtained cloud size using this method is not accurate. Systematic error can exist, shifting the linear fit which determines his zero-crossing magnetic field. In contrast, the measurement method described in this chapter is independent of fitting models and algorithms. The spatial profiles are normalized and scaled in a consistent way (described in Appendix A) so that shot-to-shot variation is minimized.

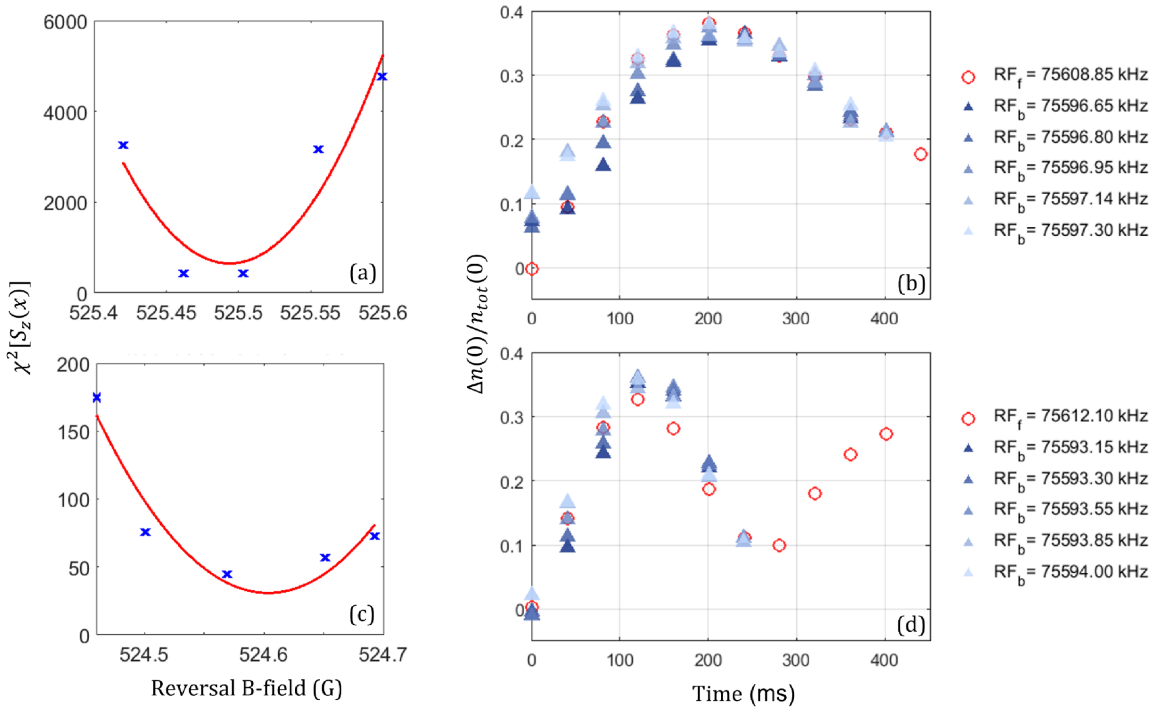

Figure 5.3: Finding the optimum magnetic fields for reversing the spin evolution at two initial magnetic fields. (a)(b) are done at the forward evolution field $B_f = 528.803$ G ($a \approx 5\,a_0$), where the resonant RF frequency is $RF_f = 75608.85$ kHz, with the sign of Hamiltonian inverted after forward evolution time $\tau_f = 400$ ms; (c)(d) are done at $B_f = 529.713$ G ($a \approx 8\,a_0$), where the resonant RF frequency is $RF_f = 75612.10$ kHz, with the sign of Hamiltonian inverted after $\tau_f = 240$ ms. (a)(c) quantify the reversibility with different reversal magnetic fields B_b. Blue crosses are calculated χ^2 results for forward and backward evolution spin density spatial profiles $S_z(x)$. Red curves are parabolas fitted to χ^2 as a function of reversal magnetic field B_b. The parabola fits suggest that the optimum reversal field for $B_f = 528.803$ G is $B_{b,opt} = 525.488$ G and the optimum reversal field for $B_f = 529.713$ G is $B_{b,opt} = 524.596$ G. (b)(d) show the central spin density $\Delta n(0)/n_{tot}(0)$ at different evolution times for both forward (red circle) and backward (blue triangles) evolution data. Darker blue corresponds to higher resonant frequency RF_b at B_b, which means a higher magnetic field.

5.3.3 Reversibility of the system in different regimes

This technique of quantifying the reversal quality can also be used to compare the reversibility for systems in different regimes of scattering length and forward evolution time. This is achieved by weighting the disagreement between forward and backward in spatial profiles differently for different t_k: By construction, the disagreement is weighted more heavily for small t_k, where the system has evolved backward long enough for discrepancies between backward and forward evolution to appear. For small t_k, $S_{fz}(x, t_k)$ is usually small, i.e., close to a horizontal line around x-axis, because the system has not segregated very much for short forward evolution times. Hence, the denominator in Eqn. 5.4 exaggerates the magnitude of χ_k^2 for small t_{fk}.

Also, for the perturbed quantum rewinding type experiments, the evolution times are always chosen to be $\tau_b = \tau_f$, which means that the reversal quality at $t_k = 0$ ms is critical. Hence, χ_k^2 at $t_k = 0$ ms needs to be weighted highly in the test of reversibility especially for the purpose of choosing regimes to do perturbed quantum rewinding experiments.

Note that, χ^2 in Fig. 5.3(a) is one order of magnitude larger than it in (c), which means the system is reversed better at 8.05 a_0 for $\tau = 240$ ms than 5.19 a_0 for $\tau = 400$ ms. This matches the result shown in Fig. 5.3 (b)(d): for 5.19 a_0, $\tau_f = 400$ ms data series, it still shows a clear sign of segregation for Hamiltonian reversed data at $t_i = 0$ ms even if the optimum reversal magnetic field is adopted, and in contrast, 8.05 a_0, $\tau_f = 240$ ms case shows almost a perfect reversal at $t_k = 0$ ms.

With this method of quantification, a systematic study of the reversibility of a system in certain regimes can be done by fixing τ_f and varying scattering length and fixing scattering length and varying τ_f.

5.4 Hamiltonian reversal for three regimes

Two terms in the system Hamiltonian shown in Eq. 5.1 are Zeeman term (led by Ω) and mean-field term (led by g_{ij}). When the system is in the Zeeman dominated regime, Eq. 5.1 describes it more precisely since most of the approximations are done in the mean-field term. As described in Ch. 3, the system is switched to different regimes at different scattering lengths. As shown in Sec. 4.2, the central spin density evolution has different behavior at different regimes. This section shows the study of Hamiltonian reversal in three regimes: Zeeman dominated, $a =$ 3.00 a_0, Mean-field dominated, $a = 8.05\ a_0$, and comparable magnitude, $a = 5.19\ a_0$.

5.4.1 Zeeman dominated regime

In this regime, the central spin density evolution curve does not oscillate, it remains at an equilibrium state once two spin states are fully segregated. Therefore, the central spin density oscillation amplitude decay described in Sec. 4.2.2 cannot be observed in this regime, which means that model agrees with data even at long evolution time when simply looking at forward evolution.

Fig. 5.4 shows the result of Hamiltonian reversal done at 3.00 a_0 with three different τ_f. Red circles are forward evolution data and blue triangles are Hamiltonian reversed data. This set of data suggests that the system is reversed back to its initial state very well with $\tau_f = 200$ ms, but still shows a clear sign of segregation if the experiment is done with $\tau_f = 350$ ms, which means that although the Hamiltonian is inverted at a place ($t_f = 350$ ms) where forward evolution data doesn't have discrepancy with the model, the system is not able to reverse to its non-segregated state somehow. This indicates that, in this system, there is a part of evolution that is not reversible although the model described in Ch. 3 suggests the time-reversible Hamiltonian.

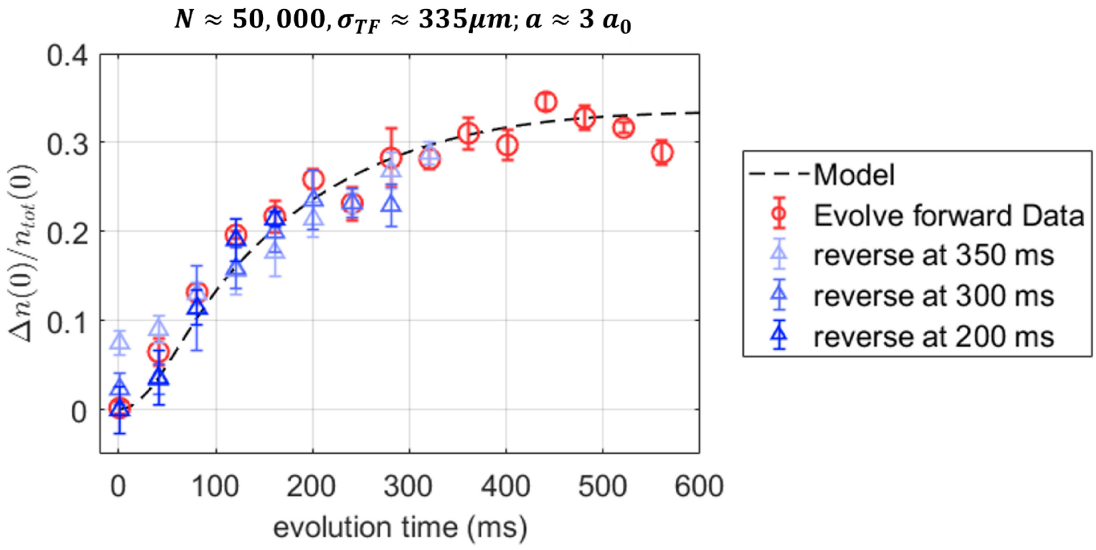

Figure 5.4: Central spin density curve for forward (red circles) and backward (blue triangles) evolution data from Hamiltonian reversal experiment at 3.00 a_0 with system reversed at different times (darker blue corresponds to earlier reversal time).

5.4.2 Zeenam and Mean-field terms with comparable magnitude

A series of Hamiltonian reversal experiments are done at scattering length $a = 5.19\ a_0$, where the Zeeman tuning rate and mean-field frequency are approximately the same. The result is shown in Fig. 5.5. The Hamiltonian is inverted at four different forward evolution times τ_f: 800 ms, 400 ms, 320 ms, and 240 ms. For $\tau_f = 240$ and 320 ms, the reversal results are almost the same. For $\tau_f = 400$ ms data set, one can already tell that the system is not back to the initial state at $t_k = 0$ point. It is remarkable that, although the backward evolution data with $\tau_f = 800$ ms shows an obvious sign of remaining segregation at $t_k = 0$, $\Delta n(0)/n_{tot}(0)$ curve oscillates with a significant amplitude despite the long total evolution time $(\tau_f + \tau_b)$.

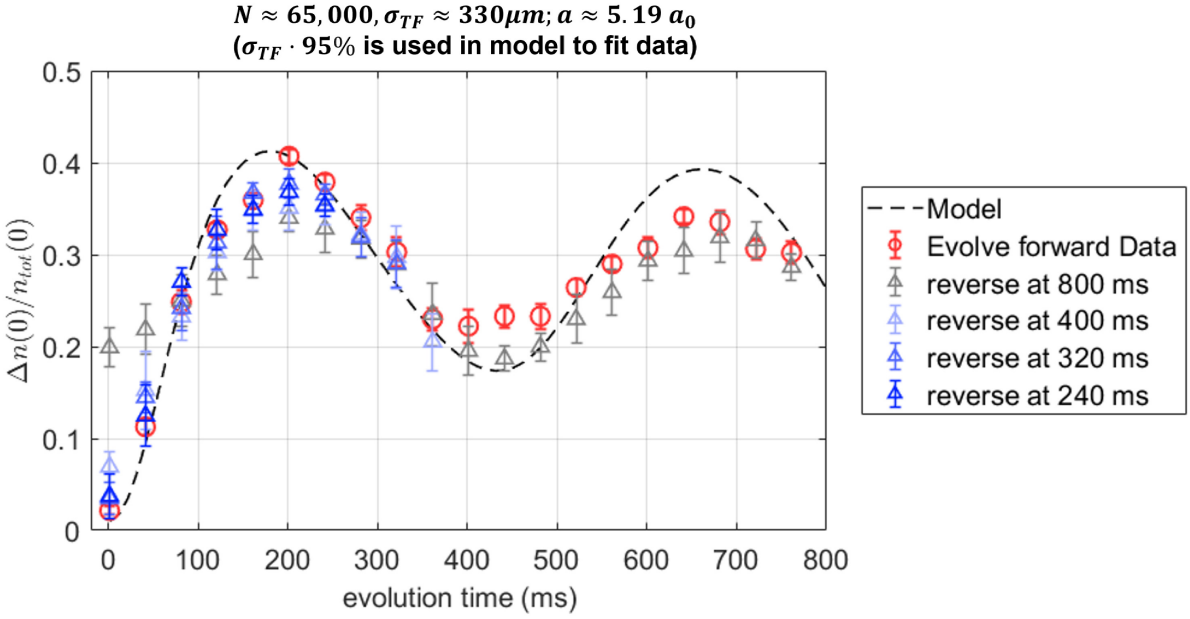

Figure 5.5: Central spin density curve for forward (red circles) and backward (blue triangles) evolution data from Hamiltonian reversal experiment at $5.19\ a_0$ with system reversed at different times (darker blue corresponds to earlier reversal time, grey triangles shows the central spin density of the backward evolution for reversal at very long evolution time $\tau_f = 800$ ms.

This result suggest that the amplitude oscillation decay for forward evolution is not due to external effect coupling to the environment during experimental cycles, otherwise, the oscillation amplitude of $\Delta n(0)/n_{tot}(0)$ would keep decaying after the Hamiltonian is inverted at 800 ms.

5.4.3 Mean-field dominated regime

The largest scattering length adopted in Hamiltonian reversal experiments in this dissertation is 8.05 a_0. The scattering length is flipped from a to $-a$ by switching magnetic field with a pair of auxiliary coils, and the range of magnetic field that the coil is able to sweep through and keep stable is limited by its geometry. The calibration of the auxiliary coil is described in Sec. 5.5. Fig. 5.6 shows the result of Hamiltonian reversal done at 8.05 a_0 for different τ_f. Note that, in this series of data, the error bars for backward evolution data with $\tau_f = 400$, 600, and 800 ms are noticeably larger than the series done at 3.00 a_0 and 5.19 a_0. The reason is the instability of magnetic field produced by the auxiliary coil. The result from this series of experiments indicates the same conclusion as the experiments implemented with 5.19 a_0. This figure suggests that the system is reversed reasonably well when the Hamiltonian is inverted at 280 ms. The same feature as observed in 5.19 a_0 experiment shows here, too: at larger t_k, the central spin density oscillation for forward evolution almost dies out, however, the backward evolution one oscillates with a larger amplitude around an offset.

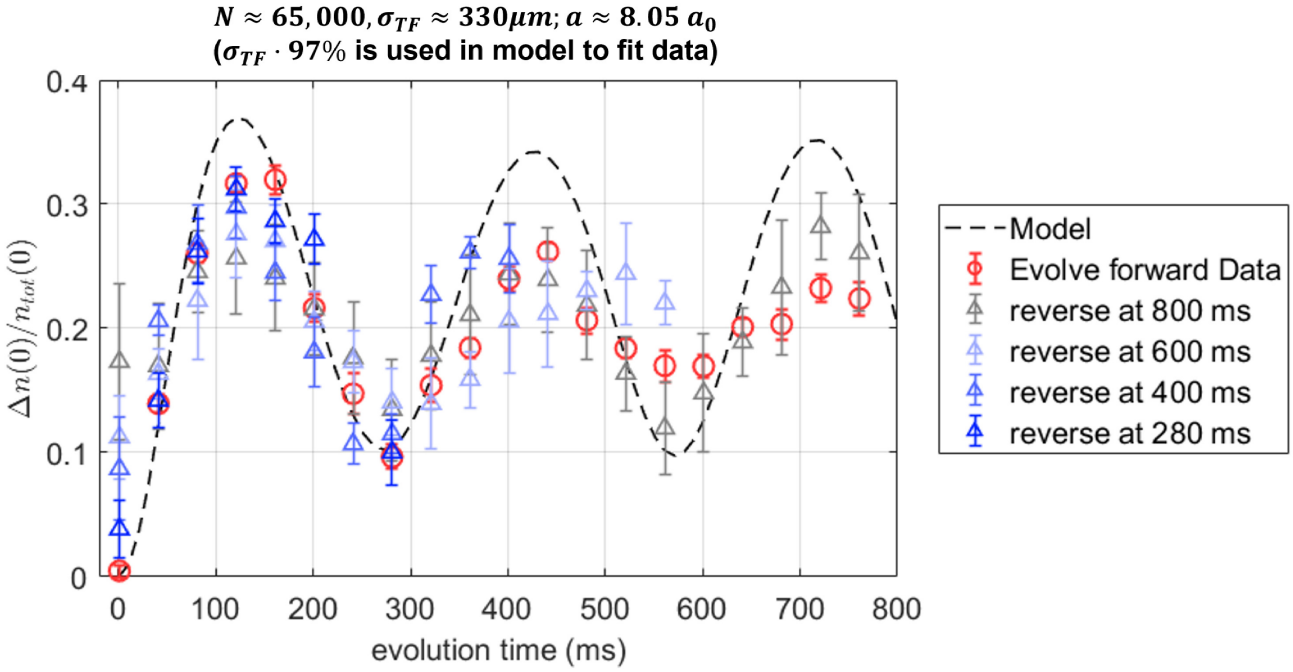

Figure 5.6: Central spin density curve for forward (red circles) and backward (blue triangles) evolution data from Hamiltonian reversal experiment at 8.05 a_0 with system reversed at different times (darker blue corresponds to earlier reversal time, grey triangles shows the central spin density of the backward evolution done at very long evolution time $\tau_f = 800$ ms.

This result suggests that observing central spin density evolution reveals multiple modes of the system: some are static, and the others oscillate. The static ones determine the offset that $\Delta n(0)/n_{tot}(0)$ oscillates around as a function of evolution time, and oscillating ones determine the oscillation amplitude. Once the system reaches the most segregated stage, the dominant oscillating terms start to decay, remaining a small oscillation around the offset. The fact that $\Delta n(0)/n_{tot}(0)$ for the backward evolution data oscillates with a larger amplitude at long t_k than forward evolution observed in $5.19\,a_0$ and $8.05\,a_0$ in the Hamiltonian reversal experiments suggests that at least one of the oscillating terms is time-reversible. The irreversible term can be a result of coupling to the environment, which is usually considered as experimental defect. However, the time-reversible one should be a real physics effect. The mean-field model introduced in Ch. 3 only predicts a static term and a constant oscillating term without decay. The result presented in this chapter indicates that to complete the model, it requires an additional oscillating term with a time-reversible decay.

5.5 Auxiliary coil calibration

In experiments that require a fast and relatively small magnetic field sweep, I implement the sweep with the auxiliary coils. This pair of low inductance copper coils are wounded around the main magnet housings (both top and bottom ones. Fig. 5.7 only shows the top side), flipping the scattering length from a to $-a$ at desired time during experimental cycle.

The timing for triggering and disabling the auxiliary coil and the accurate command voltage magnitude sent to it are critical for providing desired experimental parameters. In this section, I describe the calibration method for the auxiliary coils.

5.5.1 Control voltage

The control voltage is generated by an arbitrary waveform generator and a signal amplifier. The voltage is found by doing RF spectroscopy using the corresponding RF frequency for the desired magnetic field described in Sec. 4.3.2. First, I command 0 voltage to the coil and set the main magnet to generate the magnetic field corresponding to the scattering length a. Then I trigger the auxiliary coil and find the optimum voltage which gives scattering length $-a$ together with the main magnet.

Table 5.1 shows the typical scattering lengths I use in my experiments, the corresponding magnetic fields provided by the auxiliary coils, and their control voltages. These values can vary up to 5% on a daily basis, and therefore a calibration is required every time I conduct experiments involving magnetic field sweep.

Figure 5.7: Configuration of auxiliary coil (top side).

Table 5.1: Voltages commanded to the auxiliary coil to implement magnetic field sweeps and the resulted flips of the scattering length

Scattering length change (a_0)	Magnetic field change (G)	Commanded voltage (V)
$3.00 \rightarrow -3.00$	1.911	1.450
$5.19 \rightarrow -5.19$	3.306	2.465
$8.05 \rightarrow -8.05$	5.126	3.745

5.5.2 Stabilization time

To test how fast the total magnetic field is stabilized after the coil is triggered or disabled, I prepare the system in the z-polarized state, which means all atoms are in state $|2\rangle$. Then I apply a π_y pulse with the RF frequency corresponding to the magnetic field biased by the auxiliary coil. If the system had reached the desired magnetic field, this π_y pulse would be able to transfer all atoms from state $|2\rangle$ to state $|1\rangle$. Fig. 5.8 shows the fraction of atom number in state $|2\rangle$. Green data represents the population at different times after the coil is turned on, and blue data after the coil is turned off. The result shows that, the total magnetic field stabilizes at desired value about 30 ms after the coil is triggered or disabled. The π_y pulse applied here has a duration of 1 ms with -5 dBm amplitude.

However, the magnetic field reaches a magnitude that is very close to the desired value sooner than 30 ms. As calibrated by RF spectra, with 1 ms π_y pulse, the HWHM is 300 Hz

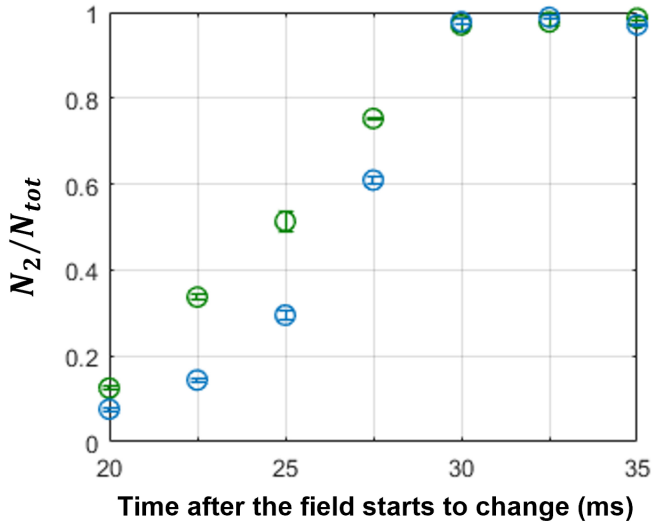

Figure 5.8: Fraction of transferred atom by doing π pulse at different times after the auxiliary coil curve is triggered (green) or disabled (blue).

corresponding to about 75 mG difference in magnetic field, $0.24\,a_0$ in scattering length. Hence, Fig. 5.8 suggests that at 20 ms, the magnetic field is only about 35 mG away from the desired level, which means that the system evolution is not delayed by such a long time.

To take into account this delay, in the experimental protocol, the backward evolution time is always shifted by an extra 6 ms to match the corresponding forward evolution time. To find the proper delay time, I take 10 images at forward evolution time $t_f = \tau_f - 40$ ms. Then I perform another series of experiments with the Hamiltonian reversed at τ_f and take 10 shots at different backward evolution times τ_b of about 40 ms. Then I compare the spatial profiles taken at different backward evolution times to the 10 shots taken for the forward evolution. τ_f is chosen to be at the first local minimum of the central spin density evolution curves, such that the curve slope is steep at t_f, giving a good sensitivity when comparing the spatial profiles. The result suggests that the images with $\tau_b = 46$ ms match the forward evolution profiles the best, which means that the delay time for backward evolution should be set to 6 ms. This calibration is performed at both $5.19\,a_0$ and $8.05\,a_0$, yielding the same result. The fact that the forward and backward evolution spatial profiles can overlap with each other so perfectly as shown in Fig. 5.2 suggests that this calibration is done properly.

CHAPTER

6

PERTURBED QUANTUM REWINDING

The perturbed quantum rewinding experiment is based on the quantum rewinding experiment introduced in Ch. 5: before inverting the Hamiltonian, a ϕ_x pulse is applied to perturb the reversal, and after the whole sequence is done, another $(\frac{\pi}{2})_y$ pulse is added to observe the transverse component of the spin vector (sequence shown in Fig. 6.1). Although we mostly treat the spin rotation quasi-classically, the ϕ_x pulse adds a quantum mechanical meaning to this system: It changes the relative phases of the superposed total angular momentum states $|S, M_x\rangle \rightarrow e^{-iM_x\phi_x}|S, M_x\rangle$ for each state. Therefore, the coherence between states receives ϕ_x-dependence (Gärttner et al. 2017, 2018; Pegahan et al. 2021).

A set of experiments described in this chapter follows the same sequence as the out-of-time-order correlation (OTOC) experiment in Ref. Pegahan et al. (2021). There, to fit the data with the quasi-classical spin model presented in Ch. 3, the scattering length needed to be increased to ≈ 2.5 times the measured value. This adjustment is not physical since the scattering length can be calculated from the magnetic field, the magnitude of which can be measured precisely with the method of RF spectra described in Sec. 4.3.2.

In this chapter, I illustrate the modifications I introduce into the previous model adopted in Ref. Pegahan et al. (2021). Then I utilize the perturbed quantum rewinding experiment to test this modified quasi-classical spin evolution model, which includes different RF detunings for two evolution periods explicitly. I present the experimental results obtained from the perturbed

quantum rewinding experiments implemented at two different scattering lengths and two evolution times, and illustrate the quantitative agreement between the modified model and experimental data. The result elucidates the effect of uncontrolled RF detunings on the system and measurements and resolves the outstanding conflict with previous treatment. With this understanding of random RF phases, I propose new correlation analysis methods, which will be discussed in Ch. 7

6.1 Experimental protocol

The experimental sequence of perturbed quantum rewinding experiment is shown in Fig. 6.1. The sample is prepared to be z-polarized spin state as described in Sec. 4.1. After that the magnetic field sweeps down to B_f close to the zero-crossing, which corresponds to scattering length a, to implement the experiment. A $(\frac{\pi}{2})_y$ pulse is applied to create the coherent superposition state of two spin states. After the system evolves forward for a time period of τ_f, an RF pulse ϕ_x is applied to perturb the rewinding. The x-pulse is achieved by connecting a voltage-controlled phase shifter in series with the output of the RF generator, so that a ϕ_y pulse can be phase shifted by 90°. The calibration of the phase shifter will be presented in Sec. 6.5.1. Right after the perturbation pulse, the sign of Hamiltonian is inverted by a combination of π_y pulse and magnetic field sweeping to B_b resulting in scattering length $-a$. This Hamiltonian reversal procedure is introduced in Sec. 5.1. With reversed Hamiltonian, the system evolves backward for a period of $\tau_b = \tau_f$. Before imaging both spins, the magnetic field is swept back to B_f and a $(\frac{\pi}{2})_y$ pulse is applied to observe the transverse components of spin vector.

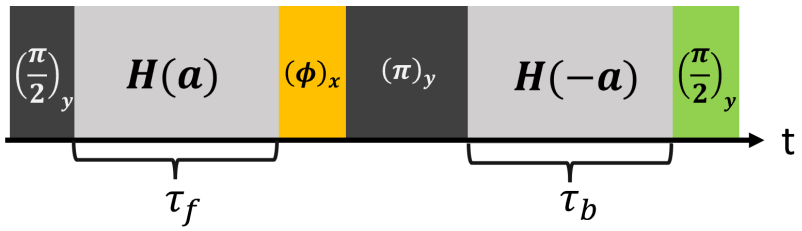

Figure 6.1: Experimental sequence for perturbed quantum rewinding. After the sample is prepared to be a z-polarized spin state as described in Sec. 4.1, this sequence is applied to it, with $\tau \equiv \tau_f = \tau_b$. Yellow and green blocks are additional pulses compared to the Hamiltonian reversal protocol shown in Fig. 5.1. The yellow block is the perturbation pulse, around x-axis, and the green block is the measurement preparation pulse, around y-axis, allowing the observation of transverse components of spin vector.

6.2 Detuning

As mentioned briefly in Sec. 3.2.3, the RF and the Bloch reference frames are defined differently: The RF frame is defined by x_{RF} and y_{RF} axes that rotate about the z-axis at the instantaneous RF frequency, $\omega_{RF}(t)$, tracking the total phase of the RF field; the Bloch frame is defined by x_B and y_B axes that rotate at the instantaneous hyperfine resonance frequency $\omega_{HF}(t)$ for an atom of axial energy $E = 0$. Ideally, during the experimental cycle, for zero detuning, the Bloch frame overlaps with the RF frame, which means that the ϕ_x, π_y and the last $(\frac{\pi}{2})_y$ rotations in the RF frame are also done about the x or y-axis in the Bloch frame.

However, the time-dependent detuning $\Delta(t) = \omega_{HF}(t) - \omega_{RF}(t)$, which is defined as the difference between the instantaneous hyperfine resonance frequency for an atom at rest and the instantaneous radiofrequency, causes different phase shifts during different evolution periods. When the hyperfine frequency is larger than the radiofrequency, spin vectors will appear to rotate counterclockwise as seen looking down the z-axis from above, i.e., through a positive angle, relative to the RF frame. In the experiments, changes in the applied bias magnetic field, as used to reverse the scattering length, and uncontrolled magnetic field fluctuations, tune the hyperfine frequency at a rate of $\simeq 5$ kHz/G. The detuning causes the components of spin vectors in the Bloch frame to rotate relative to the RF-frame by generally different angles, during the forward and backward evolution times respectively, even for $\tau_b = \tau_f = \tau$ as used in the experiments. The forward and backward phase shifts are defined by integrations of $\Delta(t)$ for τ_f and τ_b respectively,

$$\varphi_f = \int_{\tau_f} d\,t\,\Delta(t) \qquad \text{and} \qquad \varphi_b = \int_{\tau_b} d\,t\,\Delta(t), \tag{6.1}$$

and $\varphi_f \neq \varphi_b$ generally.

Experimentally, all rotations are done in the RF frame, which is defined by the RF generator. As described in detail in Sec. 6.3, φ_f controls the effective rotation axis of the perturbation ϕ_x pulse relative to the Bloch vector. In addition, the difference between phases accumulated during the τ_f and τ_b, $\varphi_{fb} \equiv \varphi_f - \varphi_b$, determines the measured spin components.

For Hamiltonian reversal experiments, when only the z-component of the spin vectors is measured, there is no sensitivity to the detuning, because the detuning is equivalent to a rotation about the z-axis. In contrast, for perturbed quantum rewinding experiments, where the transverse components of the spin vectors are measured, understanding the roles of φ_f and φ_b is critical for correct data analysis and comparison with predictions.

Although the detuning is not controlled, the experimental results presented in Sec. 6.4 show that single-shot data can be quantitatively fitted by the model described in Sec. 6.3, where

the different accumulated phase shifts for the two evolution periods, φ_f and φ_b, are properly included.

6.3 Modified spin evolution model

In my modified quasi-classical spin model, I treat the global detuning $\Delta(t)$ as time-dependent. This determines the relative angle between the RF-frame and Bloch frame φ_{fb} in Fig. 6.2. To understand how $\Delta(t)$ affects the perturbation pulse and the measurement in this experiment, the final state of the system after the pulse sequence of Fig. 6.1 is derived in this section.

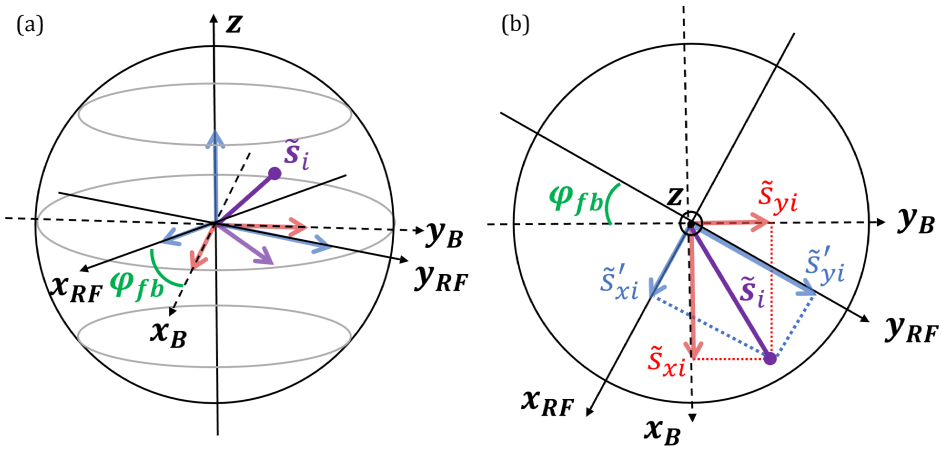

Figure 6.2: Relation between the spin vector components in RF frame and Bloch frame for nonzero φ_{fb}. (b) is the top view of (a).

As described in Sec. 6.1, before implementing this experiment, samples are initially prepared in a z-polarized state,

$$|\psi_{0z}\rangle = \Pi_i |\uparrow_{zi}\rangle. \tag{6.2}$$

To find the final state including the global detuning, the Hamiltonian of Eq. 5.1 is written in the general form

$$\frac{H(a)}{\hbar} = \frac{H_0(a)}{\hbar} + \Delta(t) S_z, \tag{6.3}$$

where S_z is the z-component of the dimensionless *total* spin vector. Here, the time-*independent*

part of the Hamiltonian, for $\Delta = 0$, is defined by

$$\frac{H_0(a)}{\hbar} = \sum_{i,j\neq i} g_{ij}\,\vec{s}_i \cdot \vec{s}_j + \sum_i \Omega'_{E_i}\, s_{zi} \tag{6.4}$$

and

$$[H_0(a), S_z] = 0. \tag{6.5}$$

For measurements of spin components in the RF frame, the final state of the system after applying the sequence shown in Fig. 6.1 with $\tau_f = \tau_b = \tau$ becomes:

$$|\psi_f\rangle = e^{-i\frac{\pi}{2}S_y} \underbrace{e^{-\frac{i}{\hbar}H_0(-a)\tau - i\varphi_b S_z} e^{-i\pi S_y}}_{I} \underbrace{e^{-i\phi_x S_x} e^{-\frac{i}{\hbar}H_0(a)\tau - i\varphi_f S_z}}_{II} e^{-i\frac{\pi}{2}S_y} |\psi_{0z}\rangle. \tag{6.6}$$

To simplify Term I:
Insert $\mathbb{1} = e^{-i\pi S_y} e^{i\pi S_y}$:

$$e^{-\frac{i}{\hbar}H_0(-a)\tau - i\varphi_b S_z} e^{-i\pi S_y} = e^{-i\pi S_y}\left[e^{i\pi S_y} e^{-\frac{i}{\hbar}H_0(-a)\tau - i\varphi_b S_z} e^{-i\pi S_y}\right],$$

and then apply $(\pi)_y$ rotation and scattering length flipping to reverse the Hamiltonian as described in Sec. 5.2. which invert S_z to Eq. 6.4:

$$e^{i\pi S_y}\left[\frac{H_0(-a)}{\hbar}\tau + \varphi_b S_z\right] e^{-i\pi S_y} = -\frac{H_0(a)}{\hbar}\tau - \varphi_b S_z.$$

To simplify Term II:
Inserting $\mathbb{1} = e^{-i\varphi_f S_z} e^{i\varphi_f S_z}$ again:

$$e^{-i\phi_x S_x} e^{-i\varphi_f S_z} = e^{-i\varphi_f S_z}\left[e^{+i\varphi_f S_z} e^{-i\phi_x S_x} e^{-i\varphi_f S_z}\right].$$

Define:

$$S_x(\varphi_f) \equiv e^{+i\varphi_f S_z} S_x\, e^{-i\varphi_f S_z} = S_x \cos\varphi_f - S_y \sin\varphi_f, \tag{6.7}$$

which is derived the same way as Eq. 7.9. Then

$$e^{-i\phi_x S_x} e^{-i\varphi_f S_z} = e^{-i\varphi_f S_z} e^{-i\phi_x S_x(\varphi_f)}.$$

With simplified Terms I and II, using commutation relation in Eq. 6.5, final state has this form:

$$|\psi_f\rangle = e^{-i\frac{3\pi}{2}S_y} e^{+i(\varphi_b - \varphi_f)S_z} e^{+\frac{i}{\hbar}H_0(a)\tau} e^{-i\phi_x S_x(\varphi_f)} e^{-\frac{i}{\hbar}H_0(a)\tau} e^{-i\frac{\pi}{2}S_y} |\psi_{0z}\rangle. \tag{6.8}$$

Defining an operator:

$$W_\phi(\varphi_f,\tau) = e^{\frac{i}{\hbar}H_0(a)\tau} e^{-i\,\phi_x S_x(\varphi_f)} e^{-\frac{i}{\hbar}H_0(a)\tau}, \tag{6.9}$$

and the x-polarized state just after the first $(\frac{\pi}{2})_y$ rotation,

$$|\psi_{0x}\rangle = e^{-i\frac{\pi}{2}S_y}|\psi_{0z}\rangle, \tag{6.10}$$

the final state has this simple form,

$$|\psi_f\rangle = e^{-i\frac{3\pi}{2}S_y} e^{+i(\varphi_b-\varphi_f)S_z} W_\phi(\varphi_f,\tau)|\psi_{0x}\rangle. \tag{6.11}$$

With Eq. 7.9: $e^{+i\frac{3\pi}{2}S_y} s_{zi} e^{-i\frac{3\pi}{2}S_y} = +s_{xi}$, then the expectation value of s_{zi} is:

$$\langle|\psi_f|s_{zi}|\psi_f\rangle = \langle\psi_{0x}|W_\phi^\dagger(\varphi_f,\tau)e^{-i(\varphi_b-\varphi_f)S_z} s_{xi}\, e^{i(\varphi_b-\varphi_f)S_z} W_\phi(\varphi_f,\tau)|\psi_{0x}\rangle. \tag{6.12}$$

Do the same trick using Eq. 7.11, and let $\varphi_f \to \varphi_{fb} \equiv \varphi_f - \varphi_b$, $S_x \to s_{xi}$ and $S_y \to s_{yi}$:

$$e^{i(\varphi_f-\varphi_b)S_z} s_{xi}\, e^{-i(\varphi_f-\varphi_b)S_z} = s_{xi}\cos\varphi_{fb} - s_{yi}\sin\varphi_{fb}.$$

Then,

$$\begin{aligned}\langle\psi_f|s_{zi}|\psi_f\rangle =& \langle\psi_{0x}|W_\phi^\dagger(\varphi_f,\tau)s_{xi}W_\phi(\varphi_f,\tau)|\psi_{0x}\rangle\cos\varphi_{fb} \\ &- \langle\psi_{0x}|W_\phi^\dagger(\varphi_f,\tau)s_{yi}W_\phi(\varphi_f,\tau)|\psi_{0x}\rangle\sin\varphi_{fb}\end{aligned} \tag{6.13}$$

As explained before, a single shot measures the operator s_{zi} for the ensemble of atoms in the ith energy group. Eq. 6.13 shows that a single-shot measurement of the spin density profile then yields, via inverse-Abel transformation (Pegahan et al. 2021), the ensemble-averages,

$$\langle\psi_f|s_{zi}|\psi_f\rangle \equiv \langle\psi_{0x}|\tilde{s}'_{xi}|\psi_{0x}\rangle, \tag{6.14}$$

where

$$\tilde{s}'_{xi} = \cos\varphi_{fb}\,\tilde{s}_{xi} - \sin\varphi_{fb}\,\tilde{s}_{yi} \tag{6.15}$$

is the x-component of the spin vector operator relative to the RF frame just before the final $(\frac{\pi}{2})_y$ pulse as shown in Fig. 6.2. $\tilde{s}'_{xi}$ is given in terms of the components in the Bloch frame:

$$\tilde{s}_{xi} \equiv W_\phi^\dagger(\varphi_f,\tau)s_{xi}W_\phi(\varphi_f,\tau) \tag{6.16}$$

and similarly for $\tilde{s}_{yi}$.

For each measurement, the difference between the forward and backward phase shifts, $\varphi_f - \varphi_b \equiv \varphi_{fb}$, determines the relative contribution of the $\tilde{s}_{xi}$ and $\tilde{s}_{yi}$ spin components in the Bloch frame to the measured projection in the RF frame, $\tilde{s}'_{xi}$. In addition, Eq. 6.9 shows that the forward phase shift φ_f determines the effective rotation axis for the ϕ_x pulse.

6.3.1 Quasi-classical model

To compare the prediction of Eq. 6.14 to single-shot measurements in a system containing a large number of spins, the quasi-classical model introduced in Ch. 3 is employed. In this case, the Heisenberg equations for the spin-vectors $\vec{s}_i$ are treated as evolution equations for classical vectors, which neglects quantum correlations.

Recall the equation of motion Eq. 6.17 derived in Ch. 3 has the form:

$$\dot{\vec{s}}(E,t) = \vec{\Omega}(E,t) \times \vec{s}(E,t) + \sum_{E',E} g(E',E)\, \vec{s}(E',t) \times \vec{s}(E,t). \tag{6.17}$$

To include RF pulses and RF detunings into this model, write the generalized energy-dependent precession rate:

$$\vec{\Omega}(E,t) = [\Omega'_E + \Delta(t)]\hat{z} + \vec{\Omega}_R(t). \tag{6.18}$$

Ω'_E, as mentioned in Ch. 3, arises from the magnetic bowl curvature. While modeling the system, $\Delta(t)$ is assigned different values for forward and backward evolution, $\Delta(t_f) = \varphi_f/\tau_f$ and $\Delta(t_b) = \varphi_b/\tau_b$, with t_f and t_b being time points during forward and backward evolution respectively. $\vec{\Omega}_R(t)$ is created by RF pulses to rotate the system either about x_{RF} or y_{RF} axis at desired times. These equations are readily evaluated for any chosen φ_f and φ_b by numerical integration, enabling fits to single-shot data with φ_f and φ_b as fit parameters.

6.4 Measurement results

I perform the perturbed quantum rewinding experiments with scattering length and evolution time [5.19 a_0, $\tau \equiv \tau_f = \tau_b = 200$ ms] and nine different perturbation pulses ϕ_x from 0 to 2π, with a step of $\pi/4$. Two additional data sets are taken at [5.19 a_0, 400 ms] and [8.04 a_0, 200 ms], respectively. Additional data sets are taken with coarser step size in ϕ_x.

Sixty shots are taken for each set of parameters $[a, \tau; \phi_x]$. Due to the complexity of the spatial profiles for cases which $\phi_x \neq 0 \bmod 2\pi$, single-shot data analysis is essential for this experiment. Small standard deviation ($\leq 5\%$) in cloud parameters σ_{Fx} and N always exists

from cycle to cycle, which affects the density of the sample significantly, changing the evolution rate of the system and yielding slightly shifted spatial profiles even for fixed φ_f and φ_b.

6.4.1 Main data set

The experimental condition for the main data set is [5.19 a_0, 200 ms; ϕ_x], with nine different ϕ_x values: 0, $\pi/4$, $\pi/2$, $3\pi/4$, π, $5\pi/4$, $3\pi/2$, $7\pi/4$, and 2π. For $\phi_x = 0$ and $\phi_x = 2\pi$, both spins have Thomas-Fermi spatial profiles with different total spin S_z; for other ϕ_x values, the spatial profiles are rather complicated. Fig. 6.3 shows examples of single-shot data in the main data set for seven ϕ_x values where $\phi_x \not\equiv 0 \bmod 2\pi$. In this figure, blue dots in ($*1$) are directly measured single shot spatial spin density profiles (data binned and folded as described in Appendix A.1), and blue dots in ($*2$) are energy space profiles obtained by performing Abel inversion to spatial profiles in ($*1$) as described in Appendix B. Red curves in ($*2$) are energy space profiles of $s_z(E)$ directly generated by model that includes φ_f and φ_b as separate fitting parameters, and red curves in ($*1$) are predicted spatial spin density profiles by Abel transform from model shown in ($*2$). The black dashed curves shown in (b) and (c) are model adopted in Ref. Pegahan et al. (2021), which assumes $\varphi = \varphi_f \equiv \varphi_b + \pi \bmod 2\pi$ and takes φ and scattering length a_{fit} as two fit parameters. To fit data with this model, it requires $a_{fit} = 9\,a_0$ while the measured scattering length is at 5.19 a_0. It is observed that for this set of experimental parameters, the data can be fitted by both models, however, for the cases where the additional data sets are obtained (in Sec. 6.4.2), Ref. Pegahan et al. (2021) model is not able to fit data for any a_{fit} while the model reported in this dissertation quantitatively fits all data.

The single-shot data shown in Fig. 6.3 is fitted with different φ_f and φ_b pairs. These values are listed in Table 6.1 in the unit of π. Note that, this table does not represent the distribution of φ_f and φ_b for the whole data set since the shots shown in Fig. 6.3 are randomly picked for each ϕ_x among those shots with σ_{Fx} and N close to the average values.

Table 6.1: Fitted φ_f and φ_b for data shown in Fig. 6.3

$\phi_x(\pi)$	$\frac{1}{4}$	$\frac{1}{2}$	$\frac{3}{4}$	1	$\frac{5}{4}$	$\frac{3}{2}$	$\frac{7}{4}$
$\varphi_f(\pi)$	0.44	1.67	1.44	1.56	1.78	0.67	1.89
$\varphi_b(\pi)$	0.56	1.33	1.22	0.78	0.11	1.44	0.56

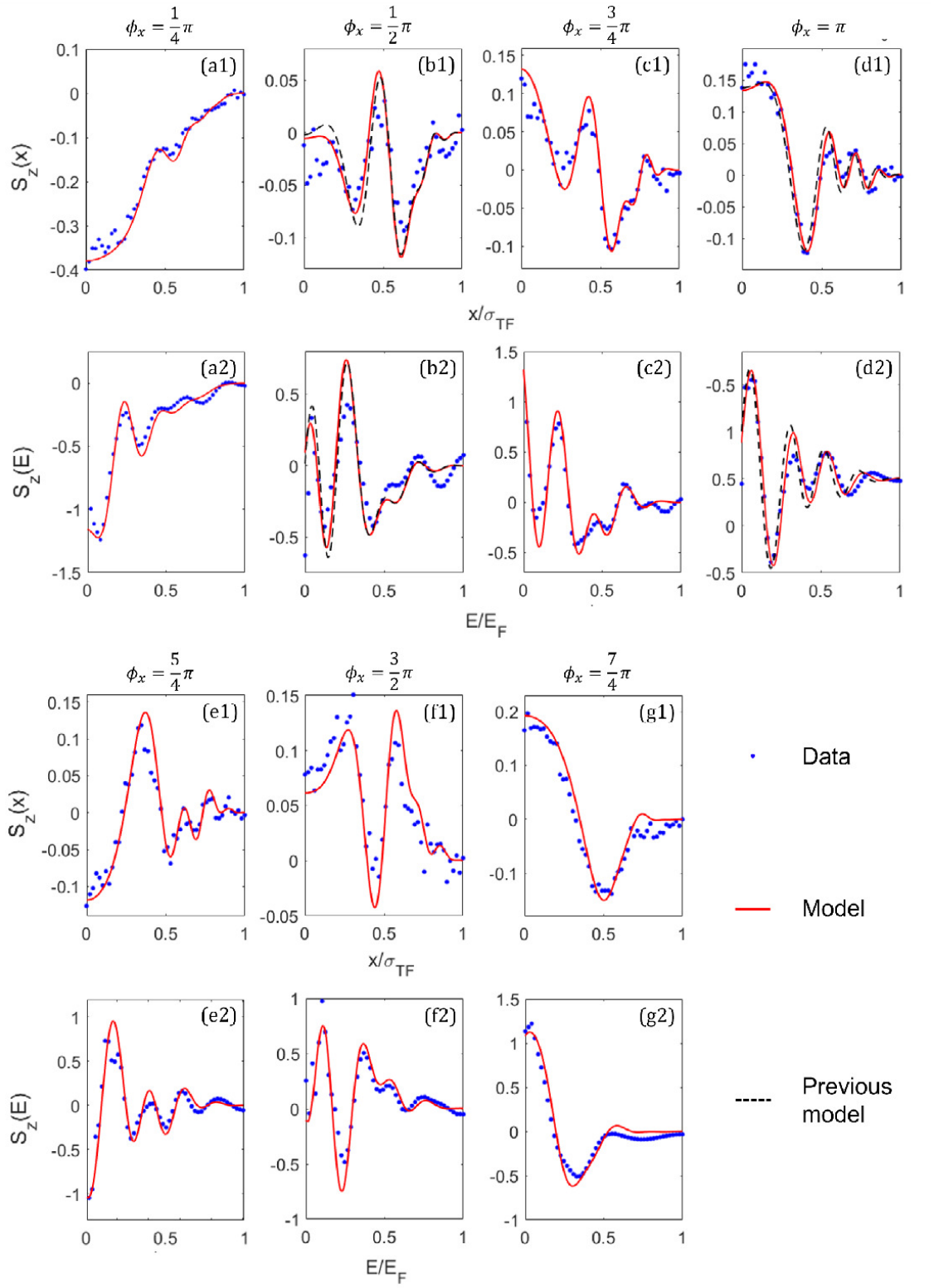

Figure 6.3: Main Data set. Experiment implemented at $\pm 5.19\, a_0$, $\tau = 200$ ms.

6.4.2 Additional data set

The validity of the quasi-classical spin model is demonstrated by the main data set with experimental conditions [5.19 a_0, 200 ms; ϕ_x] in Sec. 6.4.1. To verify this model in other regimes, additional experiments are implemented. The experimental conditions for two additional data series are [8.05 a_0, 200 ms; ϕ_x] and [5.19 a_0, 400 ms; ϕ_x], with coarser ϕ_x steps: 0, $\pi/2$, π, $3\pi/2$ and 2π. Fig. 6.4 shows the results of both data sets with $\phi_x \not\equiv 0 \bmod 2\pi$, and the legends are the same as those in Fig. 6.3. The fitted φ_f and φ_b pairs for single shots shown in Fig. 6.4 are listed below in Table 6.2.

Table 6.2: Fitted φ_f and φ_b for data shown in Fig. 6.4

$[a;\tau]$	[8.05 a_0; 200 ms]			[±5.19 a_0; 400 ms]		
$\phi_x(\pi)$	$\frac{1}{2}$	1	$\frac{3}{2}$	$\frac{1}{2}$	1	$\frac{3}{2}$
$\varphi_f(\pi)$	0.78	0.00	0.00	0.67	0.44	1.00
$\varphi_b(\pi)$	1.89	0.33	1.22	1.44	0.67	0.22

It is observed that in many shots, the agreement between model and data is less quantitative for additional data obtained at higher scattering length or longer evolution time. There are three main reasons.

First, some spatial profiles after the sequence for these cases tend to be more complicated than those shown in Fig. 6.3. For example, in Fig. 6.4 (f1) and (f2), the narrow peak shown in the model is not well presented by the data. This arises from limited imaging resolution. For this reason, some data may not show the sharp features predicted by the model.

Second, drifts in the magnetic field alter the RF pulse area. Therefore, one or more RF pulses are more likely to be slightly off resonance from the hyperfine frequency if the experimental cycle is long or the magnetic field sweep of the auxiliary coil is big. When this happens, the measured spatial profiles show obvious incorrect spin imbalance while the general features are still well predicted by the model. This incorrect spin imbalance analysis is described in detail in Appendix A.2.2.

Another reason is that the *unperturbed* quantum rewinding results are not ideal when the experiments are implemented with these parameters, as shown in Sec.5.4. Note that in Sec.5.4.2, when the reversal is done at 5.19 a_0 and 400 ms, there is an obvious sign of segregation remaining in the reversed data at $t_f = 0$ ms according to the central spin density evolution curve

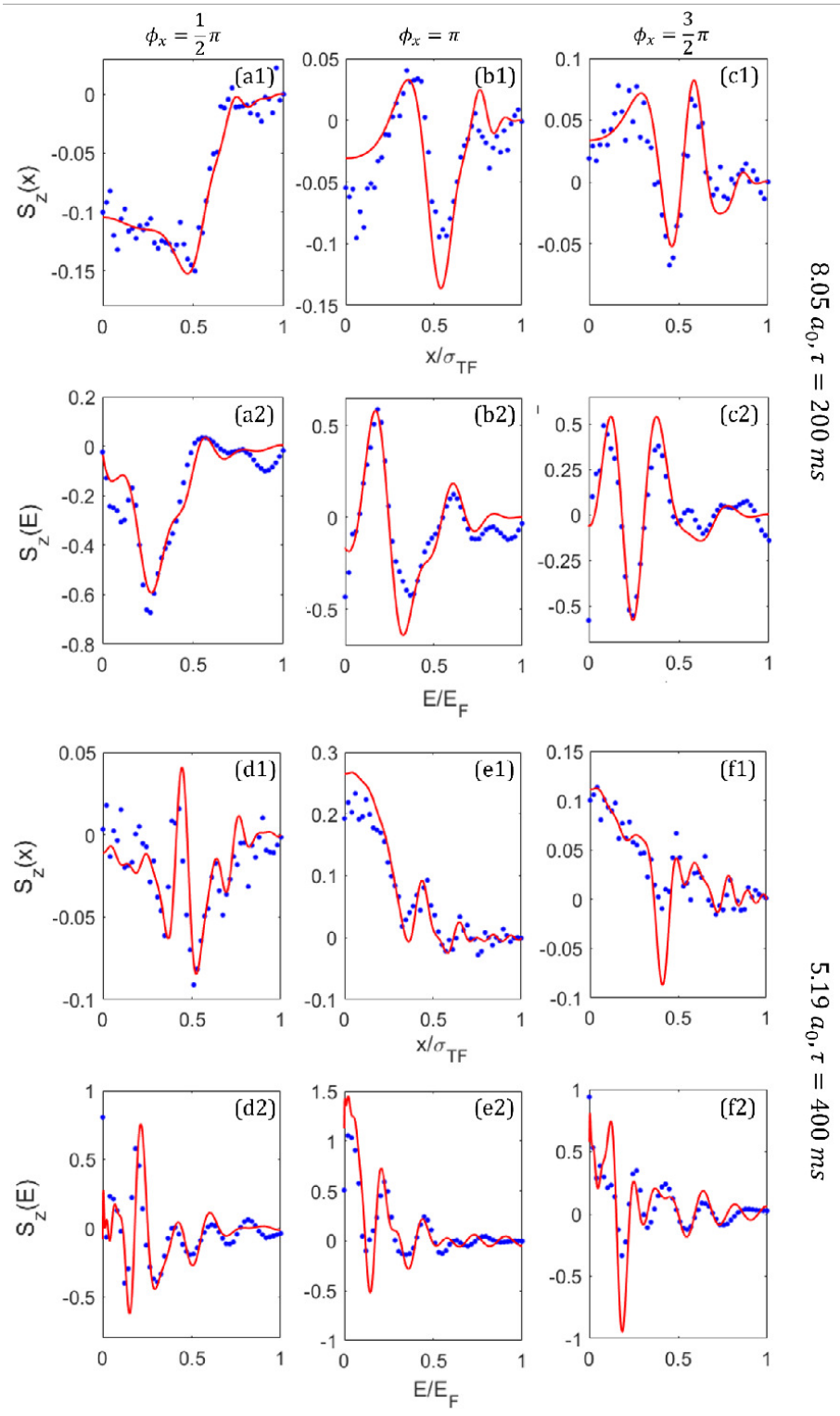

Figure 6.4: Additional Data set. Top two rows: experiment implemented at $\pm 8.05\,a_0$, $\tau = 200$ ms; Bottom two rows: $\pm 5.19\,a_0$, $\tau = 400$ ms.

in Fig. 5.5. The 8.05 a_0 case, as shown in Fig. 5.2, has much bigger error bars for the reversal data due to the limitation in stability of the auxiliary coil. For the experimental conditions in additional data sets, the forward evolution cannot be reversed properly. Therefore, it's not reasonable to expect that the perturbed quantum rewinding experiments behave as predicted by the model with these parameters.

6.5 Calibrations

Due to the complexity of the experimental sequence of the perturbed quantum rewinding experiment, before conducting this experiment, calibration procedures are required in addition to those described in Sec. 4.3.2 and Sec. 5.5.

6.5.1 Phase shifter calibration

The RF pulses applied by the RF generator are defined to be around y-axis in RF frame. To apply perturbation pulse, ϕ_x, which is around x-axis, I connect a voltage-controlled phase shifter in series with the RF generator. This is a commercial phase shifter with a broadband frequency range of 70 − 100 MHz, which covers the resonant RF transition on the two hyperfine states adopted in the experiment.

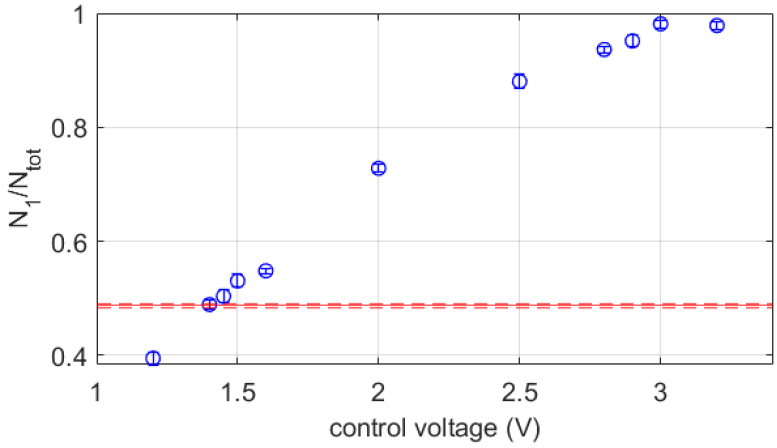

Figure 6.5: Control voltage calibration for the phase shifter. Blue circles represent the fraction of atom number transferred from spin 2 to spin 1 after applying $(\frac{\pi}{2})_\perp$ and $(\frac{\pi}{2})_y$ consecutively. Red horizontal line marks the level of fraction of atom number transferred from spin 2 to spin 1 by only doing $(\frac{\pi}{2})_y$ pulse.

To calibrate the control voltage that shifts the ϕ_y pulse by 90°, I prepare the standard z-polarized sample, and then apply a $(\frac{\pi}{2})_\perp$ and $(\frac{\pi}{2})_y$ pulses consecutively. Various command voltages allow the first pulse $(\frac{\pi}{2})_\perp$ to rotate the system around different axis in x-y plane. When $\perp \equiv x$, the $(\frac{\pi}{2})_x$ yields a y-polarized 50-50 superposition state and the $(\frac{\pi}{2})_y$ pulse doesn't have any effect on the system. Therefore, in this case, the system state after the combination of two pulses $(\frac{\pi}{2})_x$ and $(\frac{\pi}{2})_y$ is still a 50-50 superposition state. Fig. 6.5 shows the result of this calibration: blue circle shows the atom number ratio transferred from spin 2 to spin 1 after the two pulses, and red line shows the fraction transferred by only doing $(\frac{\pi}{2})_y$ pulse, which should be 0.5 idealy. The result suggests that when the control voltage is 1.4 V, the phase shifter is providing a 90° phase shift relative to y-axis in RF frame.

This control voltage for 90° phase shift can change by $\sim 15\%$ on a daily basis, especially when the phase shifter overheats. Therefore, it's essential to repeat this calibration frequently so that the perturbation pulse is applied properly.

6.5.2 Auxiliary coil timing calibration

In contrast to the Hamiltonian reversal experiment presented in Ch. 5, perturbed quantum rewinding experimental sequence requires a $(\frac{\pi}{2})_y$ pulse right before imaging, which has to be done at initial magnetic field B_f. Therefore, at the end of experimental cycle, the auxiliary coil needs to be off so that the total magnetic field can switch back. As shown in Fig. 5.8, it takes about 30 ms for the total magnetic field to settle after the auxiliary coil status is changed, whether it is turned on or off. However, it's observed that there is always a spike in the main magnet coil current when the auxiliary coil is triggered or disabled as shown in Fig. 6.6. Blue curve is the current going through the main magnet power cord measured by a Hall sensor, and orange curve is the control voltage of the auxiliary coil. At $t = 0$ ms, the auxiliary coil is triggered to provide magnetic field sweep (corresponds to $5.19\,a_0 \rightarrow -5.19\,a_0$ in this figure), which affects the main magnet due to the Faraday effect, same phenomenon is measured when the coil is shut off at 200 ms. This response plus the effect of magnetic field sweeping makes the combined magnetic field pass through B_f briefly before fully stablized, giving a very short window before the 30 ms delay which allows a narrow RF pulse to be performed on resonance with B_f.

To find the range of this window, the π_y pulse is turned on at different times after the coil is disabled, and observe the fraction of atoms remaining in state 2, as shown in Fig. 6.7. When the pulse is on resonance, there should be no atoms remaining in state 2. The result suggests that this window is extremely narrow and the delay time I adopt is 10.9 ms after the auxiliary coil is disabled. This number changes during the day, too, because of the heating effect of the

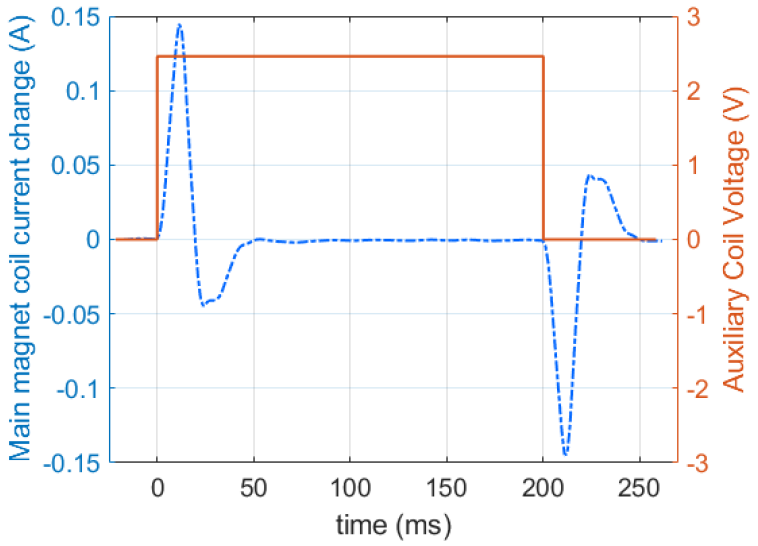

Figure 6.6: Response of current going through main magnet coil to auxiliary coil status change. The blue curve is the current going through the main magnet power cord measured by a Hall sensor. The orange curve is the command voltage to the auxiliary coil.

auxiliary coil. Therefore, this calibration needs to be performed several times during a day to ensure that the true transverse components of spin vector are observed.

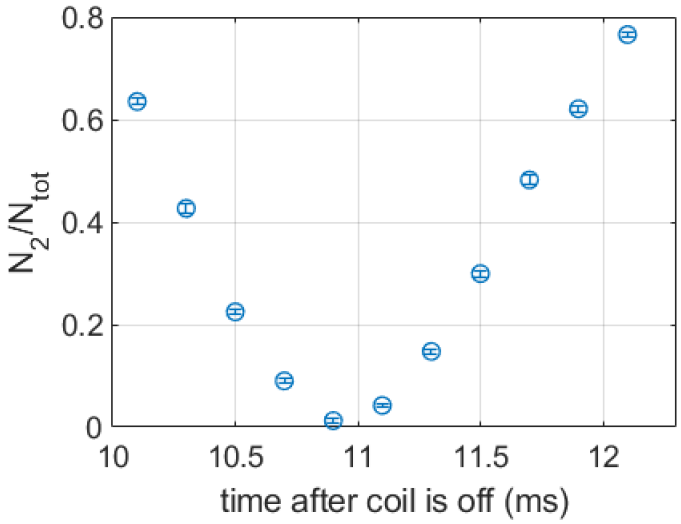

Figure 6.7: Locating the window where the last $(\frac{\pi}{2})_y$ pulse can be applied on resonance after the auxiliary coil is disabled. When the RF frequency is on resonance, there should be no atoms remaining in state 2, which corresponds to 10.9 ms after the auxiliary coil is disabled.

CHAPTER

7

CORRELATION MEASUREMENTS

In this chapter, I study the correlation between collective spin vectors in different energy groups in a system evolving with a small scttering length near zero-crossing magnetic field. The correlation function for s_σ operators for two energy groups i and j is calculated from the collective spin vector $s_\sigma(E_i)$ by

$$\mathscr{C}^{\sigma}_{ij} = \langle s_{\sigma i} s_{\sigma j} \rangle, \tag{7.1}$$

where $\langle \cdots \rangle$ represents ensemble average over multiple shots. The measured spatial spin density profile $s_\sigma(x)$ is preprocessed as described in Appendix A.1 and then Abel inversion is applied as described in Appendix B, yielding $s_\sigma(E)$ with a bin width of $\Delta E = E_F/50$. To estimate the evolution of spin vector for a single particle in each energy group, I divide $s_{\sigma i}$ by the total number of atoms in i^{th} energy bin, $N_i/2$. The correlation for single particle spin vectors then takes a form: $\boldsymbol{c}^{\sigma}_{ij} = \langle s_{\sigma i} s_{\sigma j} \rangle / (N_i N_j/4)$. Since the atom numbers in higher energy bins are very low, to reduce the signal-to-noise ratio, I only adopt the lowest $50\% - 70\%$ of energy groups of $s_\sigma(E)$ profiles to calculate the correlation functions.

First, I measure the longitudinal spin correlation $\boldsymbol{c}^{z}_{ij}$ and subtract the classical part $\langle s_{zi} \rangle \langle s_{zj} \rangle$ from it to examine if there is quantum correlation accumulating during this evolution. The result suggests that the quantum correlation in z-component is comparable to the magnitude of spin noise. Therefore, this system is expected to evolve classically, where the classical transverse correlation $\boldsymbol{c}^{\perp}_{ij}$ is of interest. By construction, $\boldsymbol{c}^{\perp}_{ij}$ also detects quantum correlations when they

are present.

Then I measure the transverse spin correlation $\boldsymbol{c}^{\perp}_{ij} = \frac{1}{2}(\langle s_{xi}s_{xj} + s_{yi}s_{yj}\rangle)/(N_iN_j/4)$ with a new data selection method, which is not highly-dependent on fitting model and does not assume an averaged RF detuning rate value. With this measurement, I observe the flow of transverse spin correlation in energy space and connect the macroscopic magnetization evolution to the localization and spread behavior of $\boldsymbol{c}^{\perp}_{ij}$.

7.1 s_z correlation measurement

Using the definition of s_z in Eq. 3.9, it is most convenient to measure the correlation in s_z operator, $\boldsymbol{c}^{z}_{ij} = \langle s_{zi}s_{zj}\rangle/(N_iN_j/4)$. By measuring it, and subtracting the classical part $\langle s_{zi}\rangle\langle s_{zj}\rangle/(N_iN_j/4)$, the magnitude of quantum correlation can be obtained. This way, I can test whether the system is quantum correlated or not: If it is, the quasi-classical model cannot fully predict the spin evolution. I initially suspected that this is the reason for the observed decay in spin wave amplitude described in Sec. 4.2.2.

To measure longitudinal spin correlation $\boldsymbol{c}^{z}_{ij}$, I perform spin segregation experiment introduced in Ch. 4 at the scattering length of $8.05\,a_0$. First, a degenerate sample is prepared, then a coherent 50-50 superposition state is excited by $(\frac{\pi}{2})_y$ RF pulse. I let the system evolve for four different times: 1, 121, 281, and 441 ms before imaging. For each evolution time, I take 30 shots to obtain enough samples for ensemble average. The measurements yield the spatial spin density of z component: $s^{meas}(x) \equiv s_z(x) = \frac{1}{2}(n_\uparrow(x) - n_\downarrow(x))$. Then individual images are processed to obtain energy space profile $s_z(E)$, containing 50 s_{zi} values for each shot, corresponding to 50 equal-spaced energy partitions. $\mathscr{C}^{z}_{ij}$ is calculated by doing matrix multiplication to a single shot $s_z(E)$ vector yielding a 50×50 matrix, and averaging the obtained matrix for all 30 shots. $\mathscr{C}^{z}_{ij}$ is normalized by the product of atom numbers in the corresponding energy partitions i and j: $\boldsymbol{c}^{z}_{ij} = \mathscr{C}^{z}_{ij}/(N_iN_j/4)$. The classical part is obtained by averaging $s_z(E)$ for all 30 shots first to get $\langle s_z\rangle$, then do matrix multiplication to obtain one 50×50 matrix $\langle s_{zi}\rangle\langle s_{zj}\rangle$. In the end, the quantum mechanical contribution to the measured correlation is estimated by: $\boldsymbol{c}^{z}_{ij} - \langle s_{zi}\rangle\langle s_{zj}\rangle/(N_iN_j/4)$.

The result from this experiment is shown in Fig. 7.1. The top row shows the correlation $\boldsymbol{c}^{z}_{ij}$ at four different evolution times. Each pixel represents the correlation between one pair of particles in energy groups E_i and E_j, with maximum and minimum possible values $\pm\frac{1}{2}$ by the construction of $\boldsymbol{c}^{z}_{ij}$. The bottom row shows the result after subtracting the classical correlation from it. In this figure, only the lowest 50% energy bins are shown.

Consider the full correlation function $\boldsymbol{c}^{z}_{ij}$ first. At 1 ms, immediately after the coherent excitation, the system has not evolved or correlated at all. At this point, the profile of s_z is

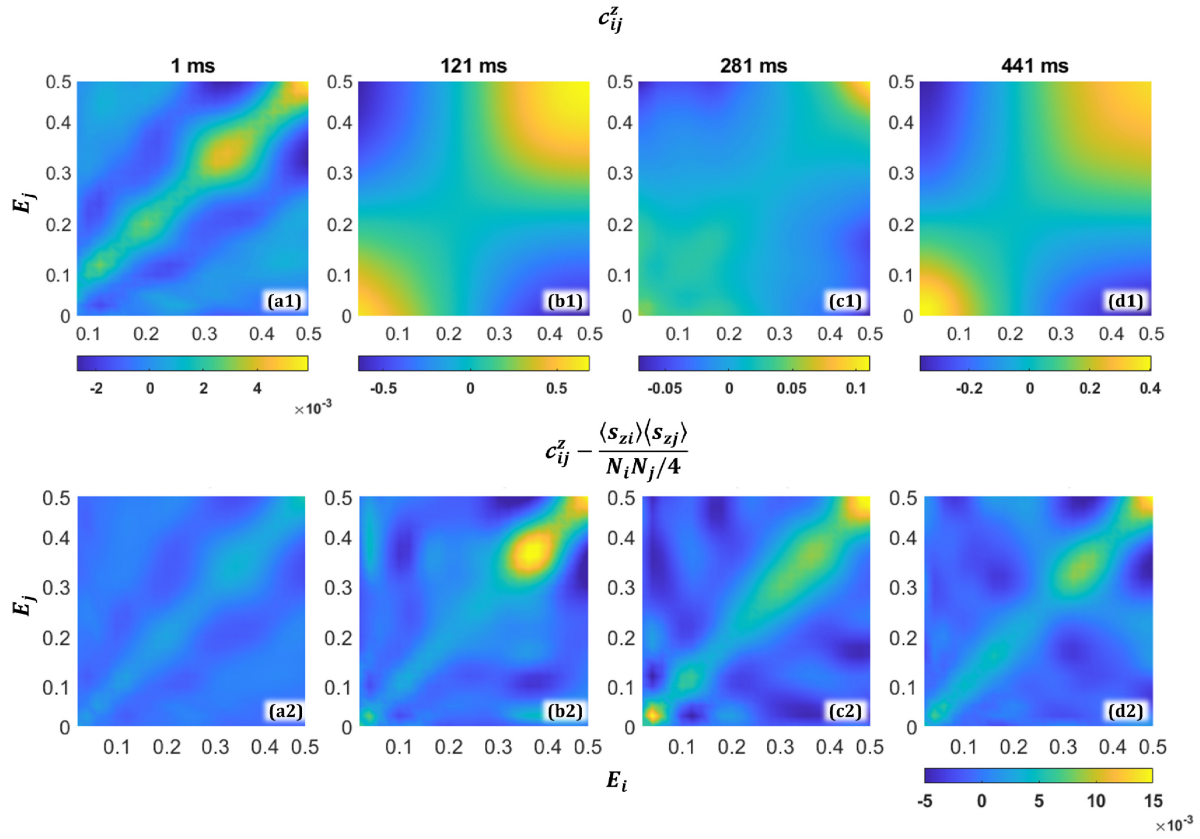

Figure 7.1: Correlation of z-component of spin vectors for the i^{th} and j^{th} energy groups at different evolution times for 8.05 a_0, normalized by the product of atom numbers in i^{th} and j^{th} energy partitions, $N_i N_j/4$. Energy E_i and E_j are in units of effective Fermi energy E_F, i.e., E_i, $E_j \in [0,1]$. Top row is directly calculated from correlation function: $\boldsymbol{c}^z_{ij}$. Bottom row is after subtracting the classical correlation $\langle s_{zi}\rangle\langle s_{zj}\rangle$ from $\boldsymbol{c}^z_{ij}$, yielding the quantum part of correlation function. Four figures in top row have their individual color bars below the corresponding figure while the four figures in the bottom row share the same color bar on the bottom of the whole row. In this figure, only the lowest 50% of the energy bins ($E/E_F \leq 0.5$) are adopted in data analysis.

expected to be a horizontal line. As expected, (a1) shows an extremely small correlation, whose color bar shows a scale of 10^{-3}. Then at 121 ms, the system evolves to its most segregated stage, where the central spin density has its maximum value, ≈ 0.35 (refer to Fig. 5.6). In (b1), the magnitude of correlation is much larger because of the large value of s_z. $|\boldsymbol{c}^z_{ij}|$ is of the order of magnitude of ~ 0.5. Note that, in (b1), negative correlation between high and low energy groups starts showing up, corresponding to the spin segregation observed in real space. At later evolution time 280 ms, two spins are less segregated again, yielding an overall smaller s_z for all energy groups. Therefore, at this time, the correlation becomes smaller again in (c1), shown by the color bar with a scale of ~ 0.05. After another 160 ms, the system is more segregated again so the correlation shown in (d1) is stronger again.

In contrast, after subtracting the classical part from $\boldsymbol{c}^z_{ij}$, the non-classical correlation is shown in the bottom row of Fig. 7.1. All quantum correlation figures, (∗2), share the same color bar on the bottom, which suggests that they are all on an order of magnitude of $\sim 5\times 10^{-3}$. The predicted mean square spin noise $\delta s^2_{zi}/N_i^2$ in s_{zi} is $4/N_i$, where N_i is the atom number in i^{th} energy bin. Take the atom number in the energy bin close to averaged energy $E_F/4$ as an example, $E\in[E_F/4, E_F(1/4+1/50)]$. According to the Thomas-Fermi distribution of the s_z energy profile, there are about 2000 atoms in it in this energy bin. Therefore, the predicted spin noise is at a level of 2×10^{-3}, which is the same order of magnitude as observed. This experiment suggests that the correlation measured during this evolution is mostly classical plus some quantum spin projection noise. In addition, the single-shot measurements in Ch. 6 showed that this large spin system can be well explained by a quasi-classical model (Huang et al. 2023). Therefore, this system is expected to evolve classically, where the classical correlation $\boldsymbol{c}^{\perp}_{ij}$ is of interest, which will be studied in Sec. 7.2.

7.2 $s_\perp$ correlation measurements

To observe the transverse component of spin vector, a Ramsey sequence is applied. Starting from an initially z-polarized state, the first excitation $(\frac{\pi}{2})_y$ RF pulse produces an x-polarized sample. After that, the system is allowed to evolve for a period τ at the scattering length a of interest. Then, a second $(\frac{\pi}{2})_y$ RF pulse is applied to collectively rotate the spin vectors about the y-axis, projecting the x-component onto the measurement z-axis, ideally. Immediately after the last RF pulse, two spin states $|\uparrow_z\rangle$ and $|\downarrow_z\rangle$ are imaged. In reality, as discussed below, $s^{meas}(x)=s_z(x)=(n_\uparrow(x)-n_\downarrow(x))/2$ measures a combination of transverse components of the spin vector in the Bloch resonant frame, $\tilde{s}_x$ and $\tilde{s}_y$, just prior to imaging. (Note that, s_z here has a different meaning from s_z in Sec. 7.1 as the experimental protocol in this section has a final $(\frac{\pi}{2})_y$ pulse in addition to that in Sec. 7.1. s_z in Sec. 7.1 is equivalent to $\tilde{s}_z$ in this section.)

Abel inversion (Appendix B) is applied to $s^{meas}(x)$ to obtain the energy-resolved spin density $s^{meas}(E)$.

The imperfectly controlled RF detuning and subsequent phase φ accumulation introduced in Ch. 6 changes the relative contribution of the x and y components of spin vectors in the measurement, $s^{meas} = \cos(\varphi)\tilde{s}_x + \sin(\varphi)\tilde{s}_y$. With a broad spread $\varphi \in [0, 2\pi]$, a multi-shot average $\langle s^{meas} \rangle$ tends to vanish. As the φ distribution for each data set is usually irreproducible, the contribution of the x and y components in $\langle s^{meas} \rangle$ cannot be controlled in an efficient and reliable way even with data selection method (See Sec. 7.2.3). This problem is circumvented in the analysis of the correlation between measured operators with energy E_i and E_j, which has the form (See Sec. 7.2.2 for derivation):

$$\begin{aligned} \mathscr{C}_{ij}^{\perp} \equiv \langle s_i^{meas} s_j^{meas} \rangle =& \frac{1}{2}\langle \tilde{s}_{xi}\tilde{s}_{xj} + \tilde{s}_{yi}\tilde{s}_{yj} \rangle \\ &+ \frac{1}{2}\langle \cos(2\varphi) \rangle \langle \tilde{s}_{xi}\tilde{s}_{xj} - \tilde{s}_{yi}\tilde{s}_{yj} \rangle \\ &- \frac{1}{2}\langle \sin(2\varphi) \rangle \langle \tilde{s}_{xi}\tilde{s}_{yj} + \tilde{s}_{yi}\tilde{s}_{xj} \rangle, \end{aligned} \tag{7.2}$$

where $\tilde{s}_{\sigma i}$ is the σ component of spin vector in Bloch frame before the last $(\frac{\pi}{2})_y$ pulse. In the data analysis, a data group is selected with a specific φ distribution to enforce $\langle \cos(2\varphi) \rangle = \langle \sin(2\varphi) \rangle = 0$, estimated using the quasi-classical spin model. This method (will be introduced in detail in Sec. 7.2.3) ensures that the correlation obtained by averaging selected single shots is $\mathscr{C}_{ij}^{\perp} = \frac{1}{2}\langle \tilde{s}_{xi}\tilde{s}_{xj} + \tilde{s}_{yi}\tilde{s}_{yj} \rangle$, without making assumptions about the φ distribution for the whole data set.

In Sec. 7.2.1, I will discuss the experimental results and conclusions. Then in Sec. 7.2.2, I will derive Eq. 7.2, the final state of the system after a Ramsey sequence. In the end, I will present two data processing methods for these experiments in Sec. 7.2.3 and Sec. 7.2.4.

7.2.1 Data

In this section, I study the evolution of transverse spin correlation as a function of scattering length at a microscopic level. For convenience, a dimensionless coefficient is defined to describe interaction strength: $\zeta \equiv \bar{g}/(\sqrt{2}\sigma_{\Omega_z})$. $\bar{g} \propto a$, is the average coupling parameter $g(E, E')$ in Eq. 3.29. $\bar{g}(a = 5.2\, a_0) \approx 1.7\,\text{Hz}\times 2\pi$. σ_{Ω_z} is the statistical standard deviation of Ω'_{E_i}, which determines the spread in spin-precession rates, $\sigma_{\Omega_z} \approx 1.4\,\text{Hz}\times 2\pi$. Larger ζ represents a stronger mean-field interaction, and for small ζ, the system is dominated by the spread in Zeeman precession.

Fig. 7.2 shows the evolution of $\boldsymbol{c}_{ij}^{\perp}$ with interaction strengths $\zeta = 1.2$ ($a = 5.19\, a_0$) (top row (a-e)) and $\zeta = 1.8$ ($a = 8.05\, a_0$) (bottom row (f-j)), normalized by the product of atom

numbers in the corresponding energy partitions i and j. Therefore, each pixel represents $\boldsymbol{c}_{ij}^{\perp}$, the correlation between one pair of particles in energy groups E_i and E_j, with maximum and minimum possible values $\pm\frac{1}{2}$ by construction from Eq. 7.2. It is observed that the system evolves in a qualitatively different way as the interaction strength increases. At $\zeta = 1.2$, the single particle pair correlation tends to be localized between multiple specific energy subgroups. At $\zeta = 1.8$, the correlation tends to become uniform across all pairs of energy groups. This qualitatively distinct behavior of microscopic correlations reveals the source of the transition in macroscopic quantities such as magnetization.

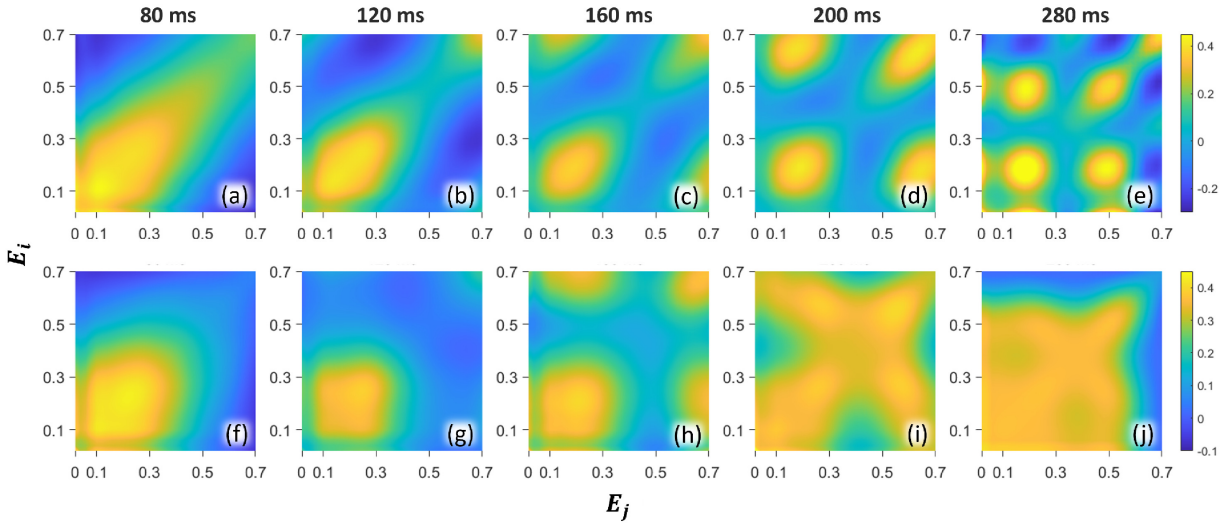

Figure 7.2: Correlation function $\boldsymbol{c}_{ij}^{\perp}$, ensemble-averaged over 30 shots with a selected φ distribution , at different evolution times with interaction strength $\zeta = 1.2$ (top row (a-e)) and $\zeta = 1.8$ (bottom row (f-j)). Figures in the same row share the same color bar on the right. In this figure, only the lowest 70% of energy bins are adopted in data analysis as higher energy groups contain very few particles. E_i and E_j are in units of effective Fermi energy E_F. The $\boldsymbol{c}_{ij}^{\perp}$ values shown here and correlation plots (b-d,f-g) in Fig. 7.3 are amplified by dividing an energy-dependent attenuation coefficient $\Gamma(E_i|\sigma_{E_F}, \alpha_r)$ arising from the finite energy resolution ($\lesssim 0.08\sqrt{E_i}$) to restore the amplitudes to their correct values (Sec. 7.2.4).

The system magnetization is related to the ensemble-averaged correlation functions by definition. The square of total transverse magnetization $\mathscr{M}_{\perp}^2 = S_x^2 + S_y^2$ is the double summation of the perpendicular correlation in energy space: $\frac{1}{2}\mathscr{M}_{\perp}^2 = \sum_{i,j} \mathscr{C}_{ij}^{\perp}$.

Fig. 7.3 shows the time-evolution of $\mathscr{M}_{\perp}^2$ with different interaction strengths. The qualitative change in the behavior of the magnetization is also observed in the microscopic correlation

$\boldsymbol{c}_{ij}^{\perp}$ between energy subgroups, which are shown as correlation plots in (b-d,f-h). For all pairs of correlation plots, the left one corresponds to $\tau = 80$ ms and the right one corresponds to $\tau = 200$ ms. For the lighter blue data in (a), where the interaction strength is very small $\zeta = 0$, 0.6, $\frac{1}{2}\mathscr{M}_{\perp}^{2}(t \to \infty) = 0$. For the darkest blue data in (a), where $\zeta = 1.2$, $\frac{1}{2}\mathscr{M}_{\perp}^{2}(t \to \infty)$ asymptotes to a non-zero, small value. For small scattering lengths, correlation figures in (b-d) show that as time evolves, the largest correlations $|\boldsymbol{c}_{ij}^{\perp}|$ (either positive or negative) arise between certain localized energy groups, either forming thin stripes or forming islands. Note that, with the absence of mean-field interaction, i.e., at $0\,a_0$, the uniform stripes shown in (b) are the Ramsey fringes in energy space. By analyzing the width of the Ramsey fringes, the Zeeman tuning rate Ω' can be tested. For stronger interactions shown in (e), where $\zeta \geq 1.8$, $\frac{1}{2}\mathscr{M}_{\perp}^{2}(t \to \infty)$ tends to oscillate relative to a larger static level as ζ increases. In addition, the behavior in pair correlation shown in (f-h) is totally different from that for small ζ (b-d). With strong interactions, high correlation regions tend to spread over all pairs of energy groups i and j.

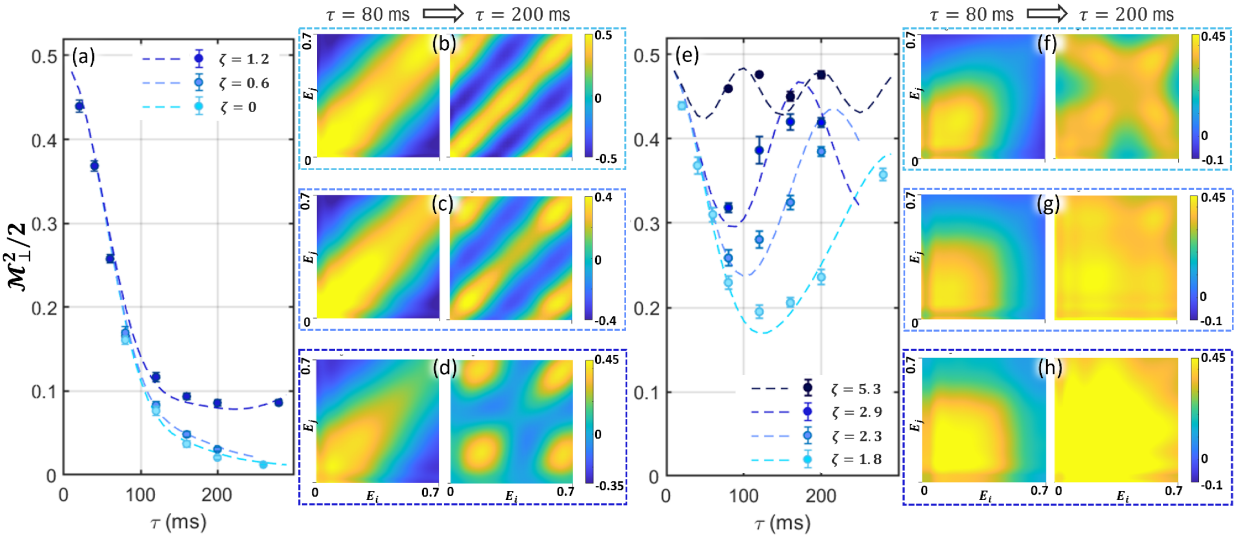

Figure 7.3: Time-dependent magnetization with different interaction strength and corresponding $\boldsymbol{c}_{ij}^{\perp}$ correlation plots. Blue circles in (a) and (e) are averaged data over multiple shots with desired φ distribution. Darker blue corresponds to stronger interaction. A detailed description of data selection and error bar calculation is Sec. 7.2.3. Dashed lines are predictions from the quasi-classical spin model. Correlation plots (b-d) and (f-h) show $\boldsymbol{c}_{ij}^{\perp}$ at $\tau = 80$ ms (left of each pair) and 200 ms (right of each pair). (b) $\zeta = 0\,(a = 0\,a_0)$, (c) $\zeta = 0.6\,(a = 2.62\,a_0)$, (d) $\zeta = 1.2\,(a = 5.19\,a_0)$, (f) $\zeta = 1.8\,(a = 8.05\,a_0)$, (g) $\zeta = 2.3\,(a = 10.54\,a_0)$, (h) $\zeta = 2.9\,(a = 13.20\,a_0)$. Same as Fig. 7.2, only $E_i, E_j \in [0, 0.7]E_F$ are shown in these correlation plots.

The transition in behavior of $\frac{1}{2}\mathscr{M}_\perp^2$, which occurs between Fig. 7.3(a-d) and (e-h) matches the one observed between Fig. 7.2 top row (a-e) and bottom row (f-j). From the measured energy-space correlation function $\boldsymbol{c}_{ij}^{\perp}$, I conclude that a system with a more localized transverse correlation between multiple specific energy group pairs tends to be demagnetized as time evolves (Fig. 7.3(a)). In contrast, a system with the transverse correlation spread over most energy group pairs maintains the high initial magnetization (Fig. 7.3(e)).

Furthermore, even when $\mathscr{M}_\perp^2$ has the same value at two different times, it is observed that the corresponding correlation plots can have totally different structures. As shown in Fig. 7.3(e), $\mathscr{M}_\perp^2(80\,\text{ms}) = \mathscr{M}_\perp^2(200\,\text{ms})$ for $\zeta = 1.8$, but the corresponding $\boldsymbol{c}_{ij}^{\perp}$ (Fig. 7.3(f)) shows different features for these two times. Similarly, for $\zeta = 1.2$ in Fig. 7.3(a), $\mathscr{M}_\perp^2(200\,\text{ms}) = \mathscr{M}_\perp^2(280\,\text{ms})$, but Fig. 7.2(e)(f) show different behaviors of $\boldsymbol{c}_{ij}^{\perp}$. Therefore, the observation of energy-resolved correlation provides a new probe to characterize the spin dynamic more deeply than simply measuring macroscopic quantities.

Fig. 7.4 shows the emergence of xy-plane magnetization versus interaction strength at four evolution times. Blue circles are measured $\mathscr{M}_\perp^2$, for the same sample selection method described above. Predictions of $\mathscr{M}_\perp^2$ (red curves) are obtained using the quasi-classical model. It is found that, as the interaction strength increases, $\mathscr{M}_\perp^2$ surges, simulating a transition to a ferromagnetic state.

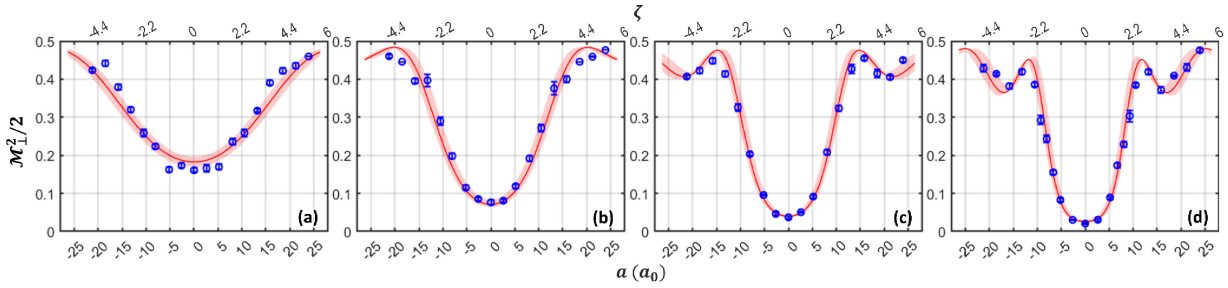

Figure 7.4: Observing the emergence of spin locking by measuring $\frac{1}{2}\mathscr{M}_\perp^2$ for various interaction strength ζ (top axis) and corresponding scattering lengths a (bottom axis) at (a) 80 ms, (b) 120 ms, (c) 160 ms, and (d) 200 ms. Blue circles are averaged data over multiple shots with the same averaging and error bar calculation for Fig. 7.3. Bright red curves are predictions with the quasi-classical spin evolution model and the pink bands correspond to a 2% standard deviation in cloud size σ_{Fx}.

A sharp rise in $|\mathscr{M}_\perp|$ has been observed and considered as a transition between dynamical states (Smale et al. 2019). The spin vector picture provides a physical illustration of this transition. Recall that, by definition, $\mathscr{M}_\perp^2 = S_x^2 + S_y^2$. Thus, the magnetization is related to the

dispersion of the spin vector in the xy-plane: the more spins cluster, the larger magnitude $\mathscr{M}_\perp^2$ has. This can be considered as a spin-locking effect. Fig. 7.5 depicts this phenomenon using the quasi-classical spin model. (a$*$) shows the spin vectors with different energies after evolving for 200 ms with a small interaction strength $\zeta = 1.2$. (a2) is the top view of (a1) and clearly shows spin vectors in different energy partitions are largely spread out over all four quadrants in the xy-plane. In the microscopic correlation picture, spins with the same or opposite azimuthal angles are strongly correlated, and positive and negative single-pair correlations tend to cancel each other, leaving a weak magnetization after double summation over all energy partitions, corresponding to low $\mathscr{M}_\perp^2$ value in Fig. 7.4(d). In contrast, (c$*$) demonstrate a spin-locked state, with $\zeta = 4.1$ after evolving for 80 ms (green), 140 ms (blue), and 200 ms (red). For all three evolution times, the spin vectors in all energy partitions tend to congregate. In this situation, spins in all energy partitions are strongly and positively correlated, resulting in a highly magnetized state, in agreement with Fig. 7.4(a-d) for $\zeta = 4.1$. (b$*$) shows an intermediate stage between (c$*$) and (a$*$): the spin vectors have not formed a bundle at $\tau = 80$ ms (green), but start showing this trend at $\tau = 140$ ms, (blue) and 200 ms (red). Further, as interaction strength increases, s_{zi} also tends to cluster, with $\langle S_z^2 \rangle$ becoming small as $\langle S_x^2 + S_y^2 \rangle$ increases.

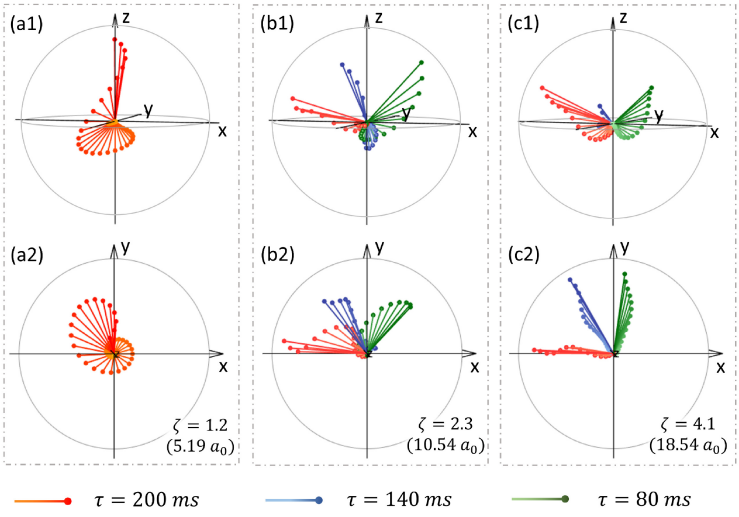

Figure 7.5: Modeled spin vector for different energy partitions (longer segments represent spin vectors with lower energy and vice versa). (a$*$) are spin vectors with $\zeta = 1.2$ at 200 ms. (b$*$,c$*$) are spin vectors at different τ with $\zeta = 2.3$ and 4.1 respectively. ($*$2) are the top views of ($*$1). Red, blue, and green segments are spins at 200, 140, and 80 ms respectively.

7.2.2 Final state derivation

In this section, I will derive the final state of the system after a Ramsey sequence to illustrate how $\langle s_i^{meas} s_j^{meas} \rangle$ can reliably measure $\langle s_{xi} s_{xj} + s_{y1} s_{yj} \rangle$ with the help of data selection method Sec. 7.2.3.

Although the measured quantity is written as $s^{meas}(x)$, it is really the z-component of the spin vector at the moment the system is imaged. However, after the last $(\frac{\pi}{2})_y$ RF pulse, there is no evolution time before imaging. Therefore, the measured quantity contains the transverse components of the spin vector just prior to imaging. For convenience, s^{meas} is written as s_z in this section so that the rotation can be illustrated more straightforwardly in the derivation.

Prior to the pulse sequence, the optically trapped atoms are initially prepared in a z-polarized state,

$$|\psi_{0z}\rangle = \Pi_i |\uparrow_{zi}\rangle. \tag{7.3}$$

Therefore, the final state after the pulse sequence is

$$|\psi_f\rangle = e^{-i\frac{\pi}{2}S_y} e^{-i\frac{H}{\hbar}\tau} \underbrace{e^{-i\frac{\pi}{2}S_y}|\psi_{0z}\rangle}_{|\psi_{0x}\rangle}. \tag{7.4}$$

As derived before in Eq. 6.4, the Hamiltonian has a form:

$$\frac{H}{\hbar} = \sum_{i,j\neq i} g_{ij} \vec{s}_i \cdot \vec{s}_j + \sum_i (\Omega'_{Ei} + \Delta(t)) s_{zi}, \tag{7.5}$$

where $\Delta(t)$ represents the RF detuning rate with unknown time dependence. Keeping the detuning part separate, I define the Hamiltonian with two parts:

$$\frac{H}{\hbar} = \frac{H^0}{\hbar} + \Delta(t) S_z, \tag{7.6}$$

then $H/\hbar\tau$ becomes:

$$\frac{H}{\hbar}\tau = \frac{H^0}{\hbar}\tau + \int_\tau \Delta(t)\, dt\, S_z = \frac{H^0}{\hbar}\tau + \varphi S_z, \tag{7.7}$$

where φ is the accumulated phase shift due to RF detuning for an evolution period τ.

Then the measurement of s_z yields:

$$\langle \psi_f | s_{zi} | \psi_f \rangle = \langle \psi_{0x} | e^{i\frac{H}{\hbar}\tau} \underbrace{e^{i\frac{\pi}{2}S_y} s_{zi} e^{-i\frac{\pi}{2}S_y}}_{s_{zi}(\frac{\pi}{2})_y} e^{-i\frac{H}{\hbar}\tau} |\psi_{0x}\rangle. \tag{7.8}$$

With Heisenberg equation of motion, $s''_{zi}(\theta_y) = s_{zi}(\theta_y)$ and initial conditions $s_{zi}(0_y) = s_{zi}$ and

$s'_{zi}(0_y) = -s_{xi}$, the analytic form is obtained:

$$s_{zi}(\theta_y) = \cos(\theta_y) s_{zi} - \sin(\theta_y) s_{xi}. \tag{7.9}$$

Then

$$\begin{aligned}\langle \psi_f | s_{zi} | \psi_f \rangle &= \langle \psi_{0x} | e^{i\frac{H}{\hbar}\tau} (-s_{xi}) e^{-i\frac{H}{\hbar}\tau} | \psi_{0x} \rangle \\ &= \langle \psi_{0x} | e^{i\frac{H^0}{\hbar}\tau} e^{i\varphi S_z} (-s_{xi}) e^{-i\frac{H^0}{\hbar}\tau} e^{-i\varphi S_z} | \psi_{0x} \rangle.\end{aligned}$$

Since the commutation rule $[H^0, S_z] = 0$, rearrange the terms to get:

$$\langle \psi_f | s_{zi} | \psi_f \rangle = \langle \psi_{0x} | e^{i\frac{H^0}{\hbar}\tau} e^{i\varphi S_z} (-s_{xi}) e^{-i\varphi S_z} e^{-i\frac{H^0}{\hbar}\tau} | \psi_{0x} \rangle. \tag{7.10}$$

Similar to Eq. 7.9, have

$$s_{xi}(\theta_z) \equiv e^{i\theta S_z} s_{xi} e^{-i\theta S_z} = \cos(\theta_z) s_{xi} - \sin(\theta_z) s_{yi}. \tag{7.11}$$

Then the measurement of s_{zi} becomes:

$$\langle \psi_f | s_{zi} | \psi_f \rangle = \langle \psi_{0x} | e^{i\frac{H^0}{\hbar}\tau} (s_{xi} \cos\varphi - s_{yi} \sin\varphi) e^{-i\frac{H^0}{\hbar}\tau} | \psi_{0x} \rangle. \tag{7.12}$$

For convenience, define:

$$\tilde{s}_{\sigma i} = e^{i\frac{H^0}{\hbar}\tau} s_{\sigma i} e^{-i\frac{H^0}{\hbar}\tau},$$

then

$$\langle \psi_f | s_{zi} | \psi_f \rangle = \langle \psi_{0x} | (\tilde{s}_{xi} \cos\varphi - \tilde{s}_{yi} \sin\varphi) | \psi_{0x} \rangle. \tag{7.13}$$

To calculate the correlation, start from:

$$\langle \psi_f | s_{zi} s_{zj} | \psi_f \rangle = \langle \psi_{0x} | e^{i\frac{H}{\hbar}\tau} \underbrace{e^{i\frac{\pi}{2}S_y} s_{zi} s_{zj} e^{-i\frac{\pi}{2}S_y}}_{(*)} e^{-i\frac{H}{\hbar}\tau} | \psi_{0x} \rangle. \tag{7.14}$$

Inserting identity operator $\mathbb{1}$:

$$(*) = e^{i\frac{\pi}{2}S_y} s_{zi} s_{zj} e^{-i\frac{\pi}{2}S_y} = e^{i\frac{\pi}{2}S_y} s_{zi} e^{-i\frac{\pi}{2}S_y} e^{i\frac{\pi}{2}S_y} s_{zj} e^{-i\frac{\pi}{2}S_y}.$$

Using Eq. 7.9 again:

$$(*) = s_{xi} s_{xj}.$$

Then Eq. 7.14 becomes:

$$\begin{aligned}\langle \psi_f | s_{zi} s_{zj} | \psi_f \rangle &= \langle \psi_{0x} | e^{i\frac{H}{\hbar}\tau} s_{xi} s_{xj} e^{-i\frac{H}{\hbar}\tau} | \psi_{0x} \rangle \\ &= \langle \psi_{0x} | e^{i\frac{H^0}{\hbar}\tau} e^{i\varphi S_z} s_{xi} s_{xj} e^{-i\frac{H^0}{\hbar}\tau} e^{-i\varphi S_z} | \psi_{0x} \rangle.\end{aligned}$$

Exchange H^0 and S_z terms and inserting $\mathbb{1}$ again:

$$\langle \psi_f | s_{zi} s_{zj} | \psi_f \rangle = \langle \psi_{0x} | e^{i\frac{H^0}{\hbar}\tau} \underbrace{e^{i\varphi S_z} s_{xi} e^{-i\varphi S_z}}_{(*1)} \underbrace{e^{i\varphi S_z} s_{xj} e^{-i\varphi S_z}}_{(*2)} e^{-i\frac{H^0}{\hbar}\tau} | \psi_{0x} \rangle. \tag{7.15}$$

Evaluating $(*1)$ and $(*2)$ with Eq. 7.11 again, obtain:

$$\langle \psi_f | s_{zi} s_{zj} | \psi_f \rangle = \langle \psi_{0x} | e^{i\frac{H^0}{\hbar}\tau} (s_{xi}\cos\varphi - s_{yi}\sin\varphi)(s_{xj}\cos\varphi - s_{yj}\sin\varphi) e^{-i\frac{H^0}{\hbar}\tau} | \psi_{0x} \rangle. \tag{7.16}$$

Using trigonometry and rearranging terms, the correlation has the form:

$$\begin{aligned}\Rightarrow \mathscr{C}_{ij}^{\perp} \equiv \langle \psi_f | s_{zi} s_{zj} | \psi_f \rangle = &\frac{1}{2} \langle \psi_{0x} | \tilde{s}_{xi} \tilde{s}_{xj} + \tilde{s}_{yi} \tilde{s}_{yj} | \psi_{0x} \rangle \\ &+ \frac{1}{2} \langle \cos(2\varphi) \rangle \langle \psi_{0x} | \tilde{s}_{xi} \tilde{s}_{xj} - \tilde{s}_{yi} \tilde{s}_{yj} | \psi_{0x} \rangle \\ &- \frac{1}{2} \langle \sin(2\varphi) \rangle \langle \psi_{0x} | \tilde{s}_{xi} \tilde{s}_{yj} + \tilde{s}_{yi} \tilde{s}_{xj} | \psi_{0x} \rangle.\end{aligned} \tag{7.17}$$

Zero scattering length limit

At the magnetic field where the scattering length vanishes, the spin vector evolution is independent of the mean-field interaction: the system evolves under Zeemen precession only. In this section, I derive the prediction for the measured ensemble averaged transverse components of the spin vector and their correlation at $0\,a_0$, including an uncontrolled detuning. In this case,

$$\frac{H^0}{\hbar}\tau = \sum_i \vartheta_{Ei} s_{zi}, \tag{7.18}$$

$$\text{where } \vartheta_{Ei} \equiv \Omega'_{Ei}\tau = \Omega' E_i \tau = -\frac{\delta\omega_x}{\hbar\overline{\omega}_x}\tau \frac{E_i}{E_F} E_F. \tag{7.19}$$

ϑ_{Ei} is energy dependent, and directly proportional to the evolution time τ. Calculating the correlation with Eq. 7.17 requires all three components, which are evaluated silimarly to Eq. 7.11:

$$\begin{aligned}
e^{i\frac{H^0}{\hbar}\tau}s_{xi}s_{xj}e^{-i\frac{H^0}{\hbar}\tau} &= e^{i\frac{H^0}{\hbar}\tau}s_{xi}e^{-i\frac{H^0}{\hbar}\tau}e^{i\frac{H^0}{\hbar}\tau}s_{xj}e^{-i\frac{H^0}{\hbar}\tau} \\
&= [s_{xi}\cos(\vartheta_{Ei}) - s_{yi}\sin(\vartheta_{Ei})][s_{xj}\cos(\vartheta_{Ej}) - s_{yj}\sin(\vartheta_{Ej})] \\
e^{i\frac{H^0}{\hbar}\tau}s_{yi}s_{yj}e^{-i\frac{H^0}{\hbar}\tau} &= e^{i\frac{H^0}{\hbar}\tau}s_{yi}e^{-i\frac{H^0}{\hbar}\tau}e^{i\frac{H^0}{\hbar}\tau}s_{yj}e^{-i\frac{H^0}{\hbar}\tau} \\
&= [s_{yi}\cos(\vartheta_{Ei}) + s_{xi}\sin(\vartheta_{Ei})][s_{yj}\cos(\vartheta_{Ej}) + s_{xj}\sin(\vartheta_{Ej})] \\
e^{i\frac{H^0}{\hbar}\tau}s_{xi}s_{yj}e^{-i\frac{H^0}{\hbar}\tau} &= e^{i\frac{H^0}{\hbar}\tau}s_{xi}e^{-i\frac{H^0}{\hbar}\tau}e^{i\frac{H^0}{\hbar}\tau}s_{yj}e^{-i\frac{H^0}{\hbar}\tau} \\
&= [s_{xi}\cos(\vartheta_{Ei}) - s_{yi}\sin(\vartheta_{Ei})][s_{yj}\cos(\vartheta_{Ej}) + s_{xj}\sin(\vartheta_{Ej})].
\end{aligned} \tag{7.20}$$

Then with some trigonometry:

$$\begin{aligned}
e^{i\frac{H^0}{\hbar}\tau}(s_{xi}s_{xj} + s_{yi}s_{yj})e^{-i\frac{H^0}{\hbar}\tau} &= \cos(\vartheta_{Ej} - \vartheta_{Ei})(s_{xi}s_{xj} + s_{yi}s_{yj}) \\
&\quad + \sin(\vartheta_{Ej} - \vartheta_{Ei})(s_{yi}s_{xj} - s_{xi}s_{yj}) \\
e^{i\frac{H^0}{\hbar}\tau}(s_{i}s_{xj} - s_{yi}s_{yj})e^{-i\frac{H^0}{\hbar}\tau} &= \cos(\vartheta_{Ej} + \vartheta_{Ei})(s_{xi}s_{xj} + s_{yi}s_{yj}) \\
&\quad - \sin(\vartheta_{Ej} + \vartheta_{Ei})(s_{yi}s_{xj} + s_{xi}s_{yj}) \\
e^{i\frac{H^0}{\hbar}\tau}(s_{xi}s_{yj} + s_{xj}s_{yi})e^{-i\frac{H^0}{\hbar}\tau} &= \cos(\vartheta_{Ej} + \vartheta_{Ei})(s_{xi}s_{yj} + s_{yi}s_{xj}) \\
&\quad + \sin(\vartheta_{Ej} + \vartheta_{Ei})(s_{xi}s_{xj} - s_{yi}s_{yj}).
\end{aligned} \tag{7.21}$$

Since $s_{xi}|\uparrow_{xi}\rangle = N_i/2|\uparrow_{xi}\rangle$,

$$\langle\psi_{0x}|s_{xi}s_{xj}|\psi_{0x}\rangle = \frac{N_i}{2}\frac{N_j}{2}.$$

When $i = j$, $\langle s_{xi}s_{yj}\rangle << N_i^2/4$ for $N_i >> 1$. For $i \neq j$,

$$\langle\psi_{0x}|s_{yi}s_{xj}|\psi_{0x}\rangle = \langle\psi_{0x}|s_{xi}s_{yj}|\psi_{0x}\rangle = 0.$$

Using these results, Eq. 7.17 can be simplified and the correlation can be written as:

$$\begin{aligned}
\boldsymbol{c}_{ij}^{\perp} \equiv \frac{\langle\psi_f|s_{zi}s_{zj}|\psi_f\rangle}{N_iN_j/4} &= \frac{1}{2}\cos(\vartheta_{Ej} - \vartheta_{Ei}) \\
&\quad + \frac{1}{2}\langle\cos(2\varphi)\rangle\cos(\vartheta_{Ej} + \vartheta_{Ei}) \\
&\quad - \frac{1}{2}\langle\sin(2\varphi)\rangle\sin(\vartheta_{Ej} + \vartheta_{Ei}).
\end{aligned} \tag{7.22}$$

7.2.3 Data selection

Because of the unknown distribution of φ, $\langle\cos(2\varphi)\rangle$ and $\langle\sin(2\varphi)\rangle$ in Eq. 7.17 can vary, leading to unknown fractions of $\tilde{s}_x\tilde{s}_x$, $\tilde{s}_y\tilde{s}_y$, and $\tilde{s}_x\tilde{s}_y$ contributions. However, by intentionally manipulating the distribution of φ such that $\langle\cos(2\varphi)\rangle = \langle\sin(2\varphi)\rangle = 0$, the measurement result is expected to give the desired $\langle\tilde{s}_x\tilde{s}_x + \tilde{s}_y\tilde{s}_y\rangle$ correlation.

A data set with the desired φ distribution is obtained by data selection. After collecting raw data set with a number of $s^{meas}(x)$ profiles and converting them to $s^{meas}(E)$ profiles using Abel inversion, each $s^{meas}(E)$ is fit with the quasi-classical model to determine fitted φ for each shot. Then a collection of pairs of shots are selected from the raw data set, such that in this collection, for each single shot k whose fitted phase is φ^k, there is another unique single shot k' whose fitted phase $\varphi^{k'} = \varphi^k + \frac{\pi}{2}$. k^{th} and k'^{th} shots form a data pair that makes $\langle\cos(2\varphi)\rangle = \langle\sin(2\varphi)\rangle = 0$. In this way, for the whole collection of k and k', k_{max} pairs of single shots are obtained and $\langle\cos(2\varphi)\rangle = \langle\sin(2\varphi)\rangle = 0$ is guaranteed for the selected $2k_{max}$ shots. Fig. 7.6 shows two examples of histograms of fitted φ, $\langle\cos(2\varphi)\rangle$ and $\langle\sin(2\varphi)\rangle$ for the raw data set (red, top row) and for the corresponding subset after data selection (blue, bottom row). For the raw data set, the distributions of these φ-related quantities are pretty random. After the data selection, $\langle\cos(2\varphi)\rangle$ and $\langle\sin(2\varphi)\rangle$ can be constrained to 0.

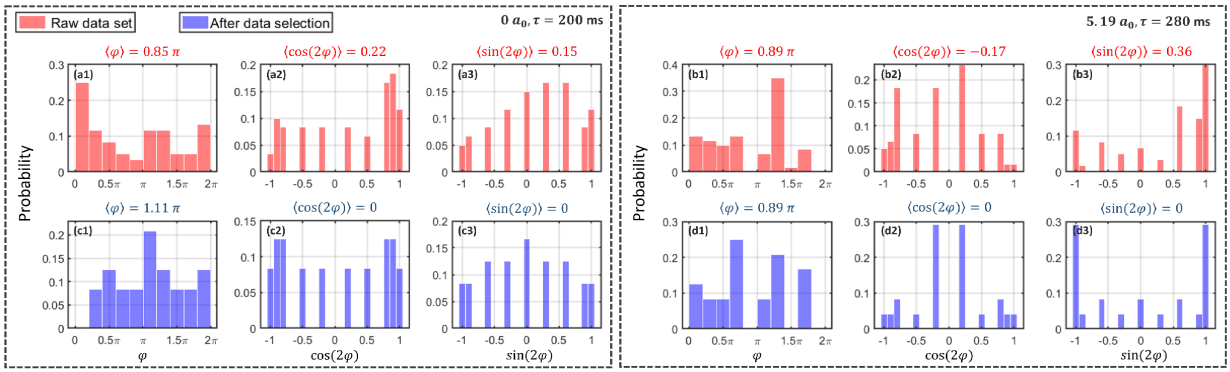

Figure 7.6: Histograms to show examples of distributions of φ-related quantities before (red) and after (blue) phase selection. ($*1$) shows the distribution of φ. ($*2$) shows the distribution of $\langle\cos(2\varphi)\rangle$. ($*3$) shows the distribution of $\langle\sin(2\varphi)\rangle$. Left dashed box is for $[0\,a_0, \tau = 200$ ms$]$ data set, while right dashed box is for $[5.19\,a_0, \tau = 280$ ms$]$.

With this method, for nonzero scattering length, the measured correlation Eq. 7.17 is written

as:

$$\begin{aligned} \mathscr{C}_{ij}^{\perp} &= \frac{1}{2}\langle\psi_{0x}|\tilde{s}_{xi}\tilde{s}_{xj}+\tilde{s}_{yi}\tilde{s}_{yj}|\psi_{0x}\rangle \\ \Rightarrow \boldsymbol{c}_{ij}^{\perp} &= \frac{4}{N_iN_j}\frac{1}{2}\langle\psi_{0x}|\tilde{s}_{xi}\tilde{s}_{xj}+\tilde{s}_{yi}\tilde{s}_{yj}|\psi_{0x}\rangle. \end{aligned} \tag{7.23}$$

For zero scattering length, the measured correlation Eq. 7.22 takes the form:

$$\boldsymbol{c}_{ij}^{\perp} = \frac{1}{2}\cos(\vartheta_{Ej}-\vartheta_{Ei}) \tag{7.24}$$

This data selection method is applied to every data set presented in Sec. 7.2. Each data point $\mathscr{M}_{\perp}^2(a,\tau)$ and its error bar in Fig. 7.3 and 7.4 in Sec. 7.2.1 are calculated from k_{max} pairs of single shots. First, make sure that k_{max} adopted to calculate error bar is the same for all data sets with $[a,\tau]$. Then to do data selection for each set, randomly choose 3 pairs of k and k' shots 10 times to obtain 10 $\mathscr{M}_{\perp,k}^2$ values. In the end, average these 10 $\mathscr{M}_{\perp,k}^2$ values to obtain the ensemble-averaged macroscopic magnetization $\mathscr{M}_{\perp}^2$. Error bars are calculated from the statistical standard deviation of these 10 $\mathscr{M}_{\perp,k}^2$ values.

Note that instead of selecting a phase φ to be around a specific value (like maximum likelihood estimation), the method presented here enforces a distribution that is flexible, as it employs the mean and deviation of φ for the raw data set, resulting in larger fraction of usable data. This method is also tolerant of the fitting model: as long as the fitting model can fit the data qualitatively and includes φ-dependence correctly, the selected data pairs will have the correct $\varphi_k' = \varphi_k + \frac{\pi}{2}$, ensuring an equal distribution of $\langle s_{xi}s_{xj}\rangle$ and $\langle s_{yi}s_{yj}\rangle$ in $\langle s_i^{meas}s_j^{meas}\rangle$. If the fitting model has a systematic offset δ in fitting result φ_k from the real RF detuning φ_k^{RF}, i.e., $\varphi_k = \varphi_k^{RF}+\delta$, this data selection method, which enforces $\varphi_k' = \varphi_k + \frac{\pi}{2}$, will still give selected data pairs with $\varphi_k^{RF'}+\delta = \varphi_k^{RF}+\delta+\frac{\pi}{2}$, and therefore $\varphi_k^{RF'} = \varphi_k^{RF}+\frac{\pi}{2}$, the desired distribution.

In contrast, for $\langle s_i^{meas}\rangle$, data selection can only be done reliably by choosing single shots with $\varphi = 0 \bmod \pi$ (ensuring $\langle s^{meas}\rangle = \pm\langle\tilde{s}_x\rangle$) or $\varphi = \frac{\pi}{2} \bmod \pi$ (ensuring $\langle s^{meas}\rangle = \pm\langle\tilde{s}_y\rangle$). This is inefficient as the selected subset is naturally much smaller than enforcing the distribution as proposed before. Also, the data selection method enforcing a specific φ value is highly dependent on the accuracy of fitting model. If the fitting result ends up with a systematic deviation from the real RF phase shift, then the ensemble average of the whole selected data set will have a contribution of the undesired transverse component. Therefore, $\langle\tilde{s}_x\rangle$ or $\langle\tilde{s}_y\rangle$ are not readily obtained by this method.

7.2.4 Energy dependent suppression

For the experiments presented in this dissertation, the sample is destroyed upon imaging for each shot. Hence all data have slightly varying atom number and cloud size and, therefore, different Fermi energies E_F, which determines the maximum Zeeman tuning and the mean-field frequency. The correlation between different energy partitions is presented in units of E_F, and higher energy partitions are more sensitive to the variation in E_F. In addition, within one shot, there is uncertainty in the measurement of each energy partition E_i. This effect arises from the finite energy resolution of the Abel Inversion and spatial resolution of the imaging system. Therefore, after averaging over multiple shots, the magnitude of the measured correlation is suppressed more for higher energy groups.

To calculate this suppression, a normal distribution of E_F and E_i is adopted:

$$P(E_F|\sigma_{E_F},\mu_{E_F}) = \frac{1}{\sigma_{E_F}\sqrt{2\pi}} exp\left[-\frac{1}{2}\left(\frac{E_F-\mu_{E_F}}{\sigma_{E_F}}\right)^2\right];$$

$$P(E_i|\sigma_{E_i},\mu_{E_i}) = \frac{1}{\sigma_{E_i}\sqrt{2\pi}} exp\left[-\frac{1}{2}\left(\frac{E_i-\mu_{E_i}}{\sigma_{E_i}}\right)^2\right].$$

Thus, when using Eq. 7.24 for $0\,a_0$ to estimate the suppression coefficient, the measured correlation has the form:

$$\int_{-\infty}^{\infty} dE_F P(E_F|\sigma_{E_F},\mu_{E_F}) \int_{-\infty}^{\infty} dE_i P(E_i|\sigma_{E_i},\mu_{E_i}) \int_{-\infty}^{\infty} dE_j P(E_j|\sigma_{E_j},\mu_{E_j}) \frac{1}{2}\cos(\vartheta_{Ej}-\vartheta_{Ei}) \quad (7.25)$$

$$\boldsymbol{c}_{ij}^{\perp} \Rightarrow exp\left[-\frac{1}{2}\left(\Omega'\mu_{E_F}\tau\right)^2\left[\left(\frac{\sigma_{E_F}}{\mu_{E_F}}\right)^2\left(\frac{E_i}{E_F}-\frac{E_j}{E_F}\right)^2+\alpha_r^2\left(\frac{E_i}{E_F}+\frac{E_j}{E_F}\right)\right]\right]\boldsymbol{c}_{ij}^{\perp}.$$

This defines an energy-dependent decay factor:

$$\Gamma(E_i|\sigma_{E_F},\alpha_r) \equiv exp\left[-\frac{1}{2}\left(\Omega'\mu_{E_F}\tau\right)^2\left[\left(\frac{\sigma_{E_F}}{\mu_{E_F}}\right)^2\left(\frac{E_i}{E_F}-\frac{E_j}{E_F}\right)^2+\alpha_r^2\left(\frac{E_i}{E_F}+\frac{E_j}{E_F}\right)\right]\right]. \quad (7.26)$$

The standard deviation, σ_{E_F}, and mean, μ_{E_F}, of the Fermi energy E_F are directly extracted from each data set: E_F for all single shot data is calculated from the measured cloud size, $E_F = m\overline{\omega}_x^2\sigma_{Fx}^2/2$, and fit the distribution with a normal probability density function $P(E_F|\sigma_{E_F},\mu_{E_F})$. Typically, for each data set, $\sigma_{E_F} \approx 0.043\mu_{E_F}$.

μ_{E_i} is just the mean energy for each energy bin. $\sigma_{E_i} \equiv \alpha_r E_F\sqrt{E_i/E_F}$ where α_r is found from the energy uncertainty $\delta E_A + \delta E_s$. δE_A arises from the number of terms n_{max} adopted to apply Abel inversion as estimated in Eq. B.16, $\delta E_A \lesssim 0.06\,E_F\sqrt{E_i/E_F}$ for $n_{max} = 12$. δE_s arises from

the finite imaging resolution and is estimated in Eq. B.15: $\delta E_s \lesssim 0.03\, E_F \sqrt{E_i/E_F}$. Therefore, the maximum $\alpha_r \approx 0.09$. In data fitting, the value of α_r is adjusted between 0.06 and 0.09, but for most cases, 0.08 is adopted.

Then the measured correlation after ensemble averaging is predicted to be scaled by Γ:

$$\Gamma(E_i|\sigma_{E_F}, \alpha_r)\, \boldsymbol{c}_{ij}^{\perp}, \tag{7.27}$$

with $\boldsymbol{c}_{ij}^{\perp}$ being the correct correlation between group i and j.

Tests of $\Gamma(E_i|\sigma_{E_F}, \alpha_r)$

With the parameters σ_{E_F} and α_r estimated, $\Gamma(E_i|\sigma_{E_F}, \alpha_r)$ can be calculated and examined quantitatively by comparing the data to quasi-classical model prediction with Γ included. Since the lowest energy group always has the largest atom number, providing the largest signal, I calculate the correlation between particles in the first (lowest) energy group and in all other energy groups, $\boldsymbol{c}_{ij}^{\perp}$, to test the validity of suppression coefficient $\Gamma(E_i|\sigma_{E_F}, \alpha_r)$.

The first test is implemented at zero scattering length. In this case, there is no mean-field interaction. Therefore the model prediction is very reliable as there is no approximation in the Zeeman precession term. Fig. 7.7 shows the result for zero scattering length case. Blue circles are the correlations obtained by averaging over about 30 single-shot data. Black dashed curves are the exact solutions predicted by Eq. 7.24. Note that this curve has a sinusoidal shape and the oscillation amplitude stays the same as it goes from low to high energy groups, while the data only has the same amplitude as the model at lower energy groups and becomes smaller and smaller compared to the model for higher energy groups. Red curves show the Γ scaled model, Eq. 7.27. As shown in this figure, with the variation in E_F and energy resolution included, the model and data are in quantitative agreement. The oscillation frequency of the data, which is determined by ϑ_{Ei} defined in Eq. 7.19, is in agreement with both predictions. This confirms that the numerical value of Ω' adopted in our model is correct.

Fig. 7.8 visualizes the correlation between all energy partitions $\boldsymbol{c}_{ij}^{\perp}$ to compare model and data. The top row shows data and bottom row shows the model calculated with Eq. 7.27. This figure confirms the agreement between the adjusted model and data.

The agreement between the model with $\Gamma(E_i|\sigma_{E_F}, \alpha_r)$ included and data for the experiment conducted at the zero-crossing suggests that the calculated energy-dependent suppression coefficient Γ predicts the decay in correlation because of the multi-shot average and finite energy resolution. To consolidate this idea and apply it to all data analysis, I do the same comparison with the data obtained at nonzero scattering length, $5.19\, a_0$. In such a situation, the exact solution Eq. 7.24 is not valid anymore. To predict the correlation, modeling $\tilde{s}_{xi}$ and $\tilde{s}_{yi}$ is

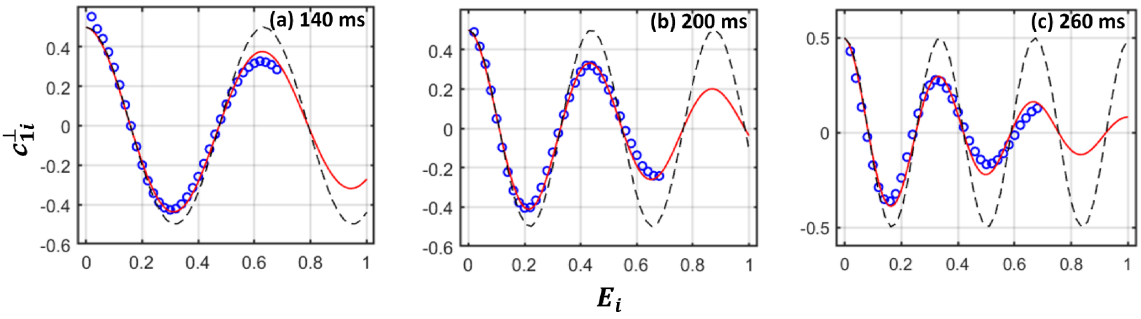

Figure 7.7: Comparing model with suppression factor Γ (red curve) and without (black dashed curve) and experimental data (blue circles) for the normalized correlation $c^{\perp}_{1j}$ at different evolution times at the zero-crossing magnetic field. Blue circles are obtained by averaging over 30 single shot data. Black dashed curve is the exact solution given in Eq. 7.24. Red curve is the adjusted model, which includes the shot-to-shot variation in E_F and the finite energy resolution. In this figure, only the lowest 70% energy bins are adopted in data analysis.

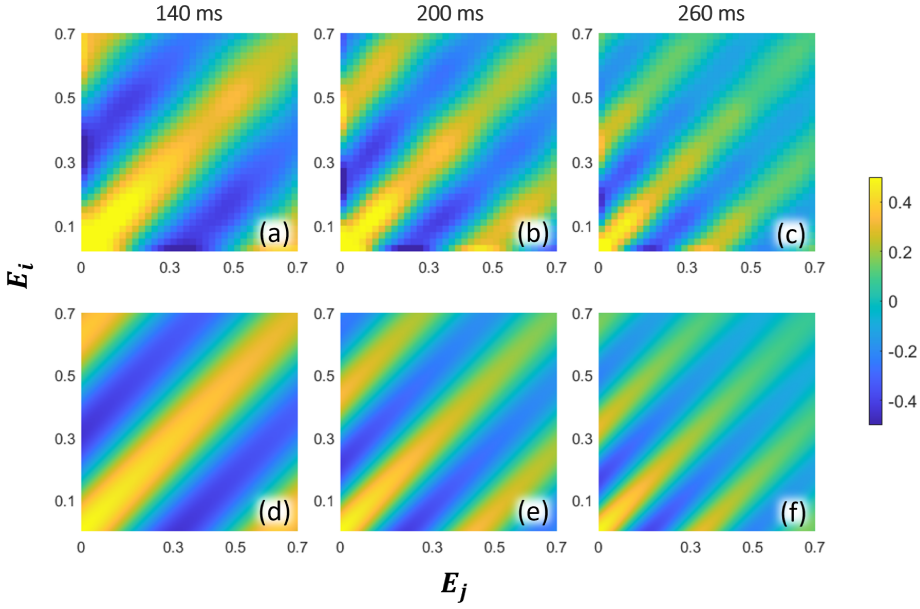

Figure 7.8: Normalized correlation $c^{\perp}_{ij}$ at different evolution times at 0 a_0. Top row is calculated from data. Bottom row is predicted by the model using Eq. 7.24 and Eq. 7.27. All panels share the same color bar. In this figure, only the lowest 70% of the energy bins are adopted in data analysis.

required. Experimental parameters σ_{Fx} and N are extracted from each shot to estimate $\tilde{s}_{xi}$ and $\tilde{s}_{yi}$ with the quasi-classical spin model, then calculate $\tilde{s}_{xi}\tilde{s}_{xj}$ and $\tilde{s}_{yi}\tilde{s}_{yj}$. Thus $\langle\psi_{0x}|\tilde{s}_{xi}\tilde{s}_{xj}|\psi_{0x}\rangle$ and $\langle\psi_{0x}|\tilde{s}_{yi}\tilde{s}_{yj}|\psi_{0x}\rangle$ are obtained by averaging over multiple predictions and $\boldsymbol{c}_{ij}^{\perp}$ is predicted using Eq. 7.17.

The model in Eq. 7.17 is not written in terms of E_F or E_i explicitly, so it is harder to include shot-to-shot variation in E_F and finite resolution of E_i in the model rigorously. However, a rough estimation can be made by applying the same exponential decay factor in Eq. 7.26 to Eq. 7.23. Thus, after the data selection, the measured correlation is predicted with:

$$\Gamma(E_i|\sigma_{E_F},\alpha_r)\frac{1}{2}\langle\psi_{0x}|\tilde{s}_{xi}\tilde{s}_{xj}+\tilde{s}_{yi}\tilde{s}_{yj}|\psi_{0x}\rangle. \tag{7.28}$$

μ_{E_F} and σ_{E_F} are obtained by fitting normal probability density function to E_F distribution for each data set. α_r is the same value as calculated for $0\,a_0$ case: $\alpha_r = 0.09$. The result of correlation between first and all other energy groups predicted by this adjusted model is shown in red curves in Fig. 7.9. In this figure, blue circles are data, black dashed curves are the raw model without E_F variation and finite energy resolution. The agreement between data and the raw model is qualitative: the oscillation frequencies of correlation for the data and model are the same, but the amplitude of correlation calculated from data is obviously smaller than the raw model prediction. In contrast, the model including E_F variation and E_i uncertainty fits the data much better.

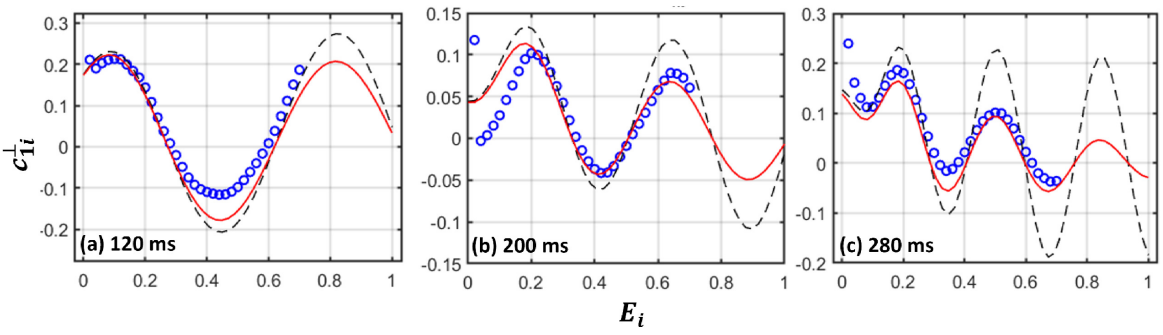

Figure 7.9: Comparing model with suppression factor Γ (red curve) and without (black dashed curve) and experimental data (blue circles) for the normalized correlation $\boldsymbol{c}_{1j}^{\perp}$ at different evolution times at $5.19\,a_0$. Blue circles are obtained by averaging over 30 single shot data. Black dashed curve is the exact solution given in Eq. 7.23. Red curve is the adjusted model, which includes the shot-to-shot variation in E_F and the finite energy resolution. In this figure, only the lowest 70% energy bins are adopted in data analysis.

By comparing the ensemble-averaged $\boldsymbol{c}_{ij}^{\perp}$ over the data set after data selection to the quasi-classical model with an energy-dependent coefficient $\Gamma(E_i|\sigma_{E_F},\alpha_r)$ included, it is confirmed that the numerical implementation of $\Gamma(E_i|\sigma_{E_F},\alpha_r)$ is consistent with data as described in this section. Therefore, for all $\boldsymbol{c}_{ij}^{\perp}$ plots presented in this Sec. 7.2, the calculated $\boldsymbol{c}_{ij}^{\perp}$ is shown after being multiplied by $\Gamma^{-1}(E_i|\sigma_{E_F},\alpha_r)$ to restore the suppressed signal to the correct multi-shot average. The value of α_r adopted varies from 0.06 to 0.09 for fitting purposes. Note that, in $\mathscr{M}_{\perp}^2$ calculation, $\Gamma^{-1}(E_i|\sigma_{E_F},\alpha_r)$ is not needed since the double summation $\sum_{i,j}\mathscr{C}_{ij}^{\perp}$ is implemented for every single shot, avoiding the suppression because of average. In the end, the $\mathscr{M}_{\perp}^2$ for the selected data set is obtained by averaging over that for all single shots.

CHAPTER

8

CONCLUSION

In this dissertation, I presented four various experiments employing different data-taking and data analysis strategies to study ensemble-averaged, energy-resolved spin vectors and their correlations in weakly interacting regime close to zero-crossing magnetic field. The measurements were analyzed based on the quasi-classical spin model.

By observing the time-dependent evolution of the spin density, I proved that for a short evolution time, the quasi-classical spin model is able to predict the longitudinal component of the spin vector, s_z. A decay in the magnitude of s_z at the center of the cloud at long evolution time has been observed both in my experiments and in a previous study (Pegahan et al. 2019) which concluded that this decay was a result of shot-to-shot variation in experimental parameters. However, by conducting a statistical study at long evolution times, I proved that this hypothesis is false. The results suggested that there can be multiple missing modes that prevent the model from predicting the system status after evolving for a long time. For the evolution of central spin density, $s_z(x=0)$, which quantifies the degree of spatial segregation of two spin states, the current model only predicts a constant oscillation amplitude of $s_z(x=0)$ over time. I concluded that in the real system, there can be multiple oscillating and static modes. Once the system reaches its most segregated stage, the oscillating modes start to decay and the static mode remains with a fixed amplitude.

Some hints about the missing pieces in the model were given by quantum rewinding

experiments. These experiments suggested that the decay in the amplitude of oscillating modes is reversible by inverting Hamiltonian, but some are not. The non-reversible ones arise from the coupling of the system and environment, which is usually considered as experimental defects. However, the oscillating modes with a time-reversible decay, I claim, may arise from real physics effects during the system evolution which are not included in the current model. Further, I developed new methods for quantifying the spin-density profiles obtained after Hamiltonian reversal, and used these measurements to precisely measure the zero-crossing magnetic field, B_0, yielding a result that is 30 mG lower than the value reported previously (Pegahan et al. 2019). The improved determination of B_0 enabled proper time-reversal and, thus, stringent new tests of spin-lattice models with perturbed quantum rewinding experiments.

A previous OTOC study questioned the adequacy of the quasi-classical spin evolution model in describing this system (Pegahan et al. 2021), suggested the probable existence of quantum correlations during evolution. I performed correlation measurements on s_z operator and proved that measured correlations are mostly classical plus some spin noise. I modified the quasi-classical model to include different RF detunings explicitly for different evolution periods separated by RF pulses. The modified model resolved the outstanding conflict observed in Ref. (Pegahan et al. 2021). Using single shot data analysis in perturbed quantum rewinding experiments, I proved that the modified quasi-classical model is in quantitative agreement with measurements in this large spin-energy lattice.

Results from the above experiments supported a classical spin description of a weakly interacting gas, which behaves as a large spin-lattice system. On the other hand, they also suggested that there are missing pieces in the quasi-classical spin evolution model. For future work, to investigate the missing pieces of the model, I plan to do statistical studies on all components of spin vectors and their correlations for different evolution times.

In the past, because of the unavoidable imperfectly controlled RF detuning, the study of transverse components of spin vector has been challenging: probabilistic methods had to be adopted in order to measure the ensemble-averaged single operator $\langle s_x \rangle$ and $\langle s_y \rangle$ (Smale et al. 2019). In contrast, I measured the correlation of transverse components of the spin vector ($\langle s_{xi} s_{xj} + s_{yi} s_{yj} \rangle$), which circumvents this problem using a new data selection method proposed in this dissertation. This method is tolerant of fitting models: Instead of trying to stabilize RF detuning rate for every piece of data, the purpose of this method is to ensure a specific RF phase shift distribution across a data set such that the transverse spin correlations can be measured using a multi-shot average method.

I used the energy-space transverse spin correlation measurement as a method for characterizing the spin dynamics. I studied the connection between the spread and localization of correlations and the system magnetization and demagnetization by observing the correla-

tion distribution as a function of time and interaction strength. In this study, I have marked energy-space spin correlation measurement as a method for characterizing the spin dynamics of quasi-continuous, weakly interacting quantum gases, which simulate a synthetic lattice of spins pinned in energy space. This method enables a full view of how correlations develop between the extensive subsets of spins in energy space on a microscopic level, associating the evolution of the macroscopic properties with the local correlation behavior. This energy-resolved probe can be exploited in studies of macroscopic out-of-equilibrium dynamics and critical dynamics across quantum phase transitions.

BIBLIOGRAPHY

Anderson, P. W. (1958). Random-phase approximation in the theory of superconductivity. *Physical Review*, 112:1900.

Arimondo, E., Inguscio, M., and Violino, P. (1977). Experimental determinations of the hyperfine structure in the alkali atoms. *Rev. Mod. Phys.*, 49:31–75.

Auerbach, A. (1994). *Interacting electrons and quantum magnetism*. Springer-Verlag, New York.

Ball, P. (2021). Evolution of spins looks surprisingly classical. *Physics World*, 34(10):6ii.

Bartenstein, M., Altmeyer, A., Riedl, S., Geursen, R., Jochim, S., Chin, C., Denschlag, J. H., Grimm, R., Simoni, A., Tiesinga, E., Williams, C. J., and Julienne, P. S. (2005). Precise determination of ^{6}Li cold collision parameters by radio-frequency spectroscopy on weakly bound molecules. *Phys. Rev. Lett.*, 94:103201.

Bloch, I., Dalibard, J., and Nascimbène, S. (2012). Quantum simulations with ultracold quantum gases. *Nature Physics*, 8:267.

Cheuk, L. W., Nichols, M. A., Okan, M., Gersdorf, T., Ramasesh, V. V., Bakr, W. S., Lompe, T., and Zwierlein, M. W. (2015). Quantum-gas microscope for fermionic atoms. *Phys. Rev. Lett.*, 114:193001.

Chin, C., Grimm, R., Julienne, P., and Tiesinga, E. (2010). Feshbach resonances in ultracold gases. *Rev. Mod. Phys.*, 82:1225–1286.

Das, A., Kulkarni, M., Spohn, H., and Dhar, A. (2019). Kardar-Parisi-Zhang scaling for an integrable lattice Landau-Lifshitz spin chain. *Phys. Rev. E*, 100:042116.

Deutsch, C., Ramirez-Martinez, F., Lacroûte, C., Reinhard, F., Schneider, T., Fuchs, J. N., Piéchon, F., Laloë, F., Reichel, J., and Rosenbusch, P. (2010). Spin self-rephasing and very long coherence times in a trapped atomic ensemble. *Phys. Rev. Lett.*, 105:020401.

Du, X., Luo, L., Clancy, B., and Thomas, J. E. (2008). Observation of anomalous spin segregation in a trapped Fermi gas. *Phys. Rev. Lett.*, 101:150401.

Du, X., Zhang, Y., Petricka, J., and Thomas, J. E. (2009). Controlling spin current in a trapped Fermi gas. *Phys. Rev. Lett.*, 103:010401.

Dukelsky, J., Pittel, S., and Sierra, G. (2004). Exactly solvable Richardson-Gaudin models for many-body quantum systems. *Reviews of Modern Physics*, 76:634–662.

Ebling, U., Eckardt, A., and Lewenstein, M. (2011). Spin segregation via dynamically induced long-range interactions in a system of ultracold fermions. *Phys. Rev. A*, 84:063607.

Eisert, J., Friesdorf, M., and Gogolin, C. (2015). Quantum many-body systems out of equilibrium. *Nature Phys.*, 11:124–130.

Gärttner, M., Bohnet, J. G., Safavi-Naini, A., Wall, M. L., Bollinger, J. J., and Rey, A. M. (2017). Measuring out-of-time-order correlations and multiple quantum spectra in a trapped-ion quantum magnet. *Nature Physics*, 13:781.

Gärttner, M., Hauke, P., and Rey, A. M. (2018). Relating out-of-time-order correlations to entanglement via multiple-quantum coherences. *Phys. Rev. Lett.*, 120:040402.

Gehm, M. E., Hemmer, S. L., O'Hara, K. M., and Thomas, J. E. (2003). Unitarity-limited elastic collision rate in a harmonically trapped Fermi gas. *Phys. Rev. A*, 68:011603.

Granade, S. R. (2002). *All-Optical Production of a Degenerate Gas of Li-6: Characterization of Degeneracy*. PhD thesis, Duke University.

Hazzard, K. and Gadway, B. (2023). Synthetic dimensions. *Physics Today*, 76(4):62.

Houbiers, M., Stoof, H. T. C., McAlexander, W. I., and Hulet, R. G. (1998). Elastic and inelastic collisions of ^{6}Li atoms in magnetic and optical traps. *Phys. Rev. A*, 57:R1497–R1500.

Huang, J., Royse, C. A., Arakelyan, I., and Thomas, J. E. (2023). Verifying a quasiclassical spin model of perturbed quantum rewinding in a fermi gas. *Phys. Rev. A*, 108:L041304.

Huang, J. and Thomas, J. E. (2023). Decoding transverse spin dynamics by energy-resolved correlation measurement. arXiv:2309.07226 [cond-mat.quant-gas].

Joshi, M. K., Elben, A., Vermersch, B., Brydges, T., Maier, C., Zoller, P., Blatt, R., and Roos, C. F. (2020). Quantum information scrambling in a trapped-ion quantum simulator with tunable range interactions. *Phys. Rev. Lett.*, 124:240505.

Kangara, J. (2018). *Atom Pairing in Optical Superlattices*. PhD thesis, North Carolina State University.

Kaufman, A. M. and et al. (2016). Quantum thermalization through entanglement in an isolated many-body system. *Science*, 353:794–800.

Koller, A. P., Wall, M. L., Mundinger, J., and Rey, A. M. (2016). Dynamics of interacting fermions in spin-dependent potentials. *Phys. Rev. Lett.*, 117:195302.

Lakshmanan, M., Ruijgrok, T. W., and Thompson, C. J. (1976). On the dynamics of a continuum spin system. *Physica*, 84A:577–590.

Lewis-Swan, R. J., Safavi-Naini, A., Bollinger, J. J., and Rey, A. M. (2019). Unifying scrambling, thermalization and entanglement through measurement of fidelity out-of-time-order correlators in the Dicke model. *Nature Communications*, 10:5007.

Natu, S. S. and Mueller, E. J. (2009). Anomalous spin segregation in a weakly interacting two-component Fermi gas. *Phys. Rev. A*, 79:051601.

O'Hara, K. (2000). *Optical Trapping and Evaporative Cooling of Fermionic Atoms*. PhD thesis, Duke University.

O'Hara, K. M., Hemmer, S. L., Gehm, M. E., Granade, S. R., and Thomas, J. E. (2002). Observation of a strongly interacting degenerate Fermi gas of atoms. *Science*, 298:2179.

Pegahan, S., Arakelyan, I., and Thomas, J. E. (2021). Energy-resolved information scrambling in energy-space lattices. *Phys. Rev. Lett.*, 126:070601.

Pegahan, S., Kangara, J., Arakelyan, I., and Thomas, J. E. (2019). Spin-energy correlation in degenerate weakly interacting Fermi gases. *Phys. Rev. A*, 99:063620.

Piéchon, F., Fuchs, J. N., and Laloë, F. (2009). Cumulative identical spin rotation effects in collisionless trapped atomic gases. *Phys. Rev. Lett.*, 102:215301.

Pretzier, G. (1991). A new method for numerical Abel-inversion. *Zeitschrift für Naturforschung A*, 46(7):639 – 641.

Richerme, P., Gong, Z.-X., Lee, A., Senko, C., Smith, J., Foss-Feig, M., Michalakis, S., Gorshkov, A. V., and Monroe, C. (2014). Non-local propagation of correlations in quantum systems with long-range interactions. *Nature*, 511:198.

Sakurai, J. J. (1993). *Modern Quantum Mechanics (Revised Edition)*. Addison Wesley, 1 edition.

Schubert, D., Richter, J., Jin, F., Michielsen, K., De Raedt, H., and Steinigeweg, R. (2021). Quantum versus classical dynamics in spin models: Chains, ladders, and square lattices. *Phys. Rev. B*, 104:054415.

Smale, S., He, P., Olsen, B. A., Jackson, K. G., Sharum, H., Trotzky, S., Marino, J., Rey, A. M., and Thywissen, J. H. (2019). Observation of a transition between dynamical phases in a quantum degenerate Fermi gas. *Science Advances*, 5(8). elocation-id: eaax1568.

Swingle, B., Bentsen, G., Schleier-Smith, M., and Hayden, P. (2016). Measuring the scrambling of quantum information. *Phys. Rev. A*, 94:040302.

Zhang, Y. (2013). *Radio Frequency Spectroscopy Of a Quasi-Two-Dimensional Fermi Gas*. PhD thesis, Duke University.

Zürn, G., Lompe, T., Wenz, A. N., Jochim, S., Julienne, P. S., and Hutson, J. M. (2013). Precise characterization of ^{6}Li Feshbach resonances using trap-sideband-resolved rf spectroscopy of weakly bound molecules. *Phys. Rev. Lett.*, 110:135301.

APPENDICES

APPENDIX

A

SPATIAL PROFILE PROCESSING

The data processing procedures introduced in Sec. A.1 are applied to all experiments in this dissertation to create dimensionless spin density profiles. For the unperturbed quantum rewinding experiments, additional preprocessing to include the total spin vector amplitude $S_z \equiv \sum_i s_{z,i} = 0$ as described in Sec. A.2.

A.1 Standard processing

To study the spin density profiles in dimensionless units, all spatial profiles are normalized and scaled axially in the same way. As described in Sec. 4.1, the axial density profiles for both spin states are obtained by integrating over the radial dimension of an absorption image. The resulted density profile $\tilde{n}_\sigma(x')$ has a unit of atom/μm, and its axis x' has a unit of μm. In this dissertation, the normalization is done such a way that ensures $S_z \equiv \sum_i s_z(x_i) = \frac{1}{2}$ before the excitation RF pulse. To achieve that, for each individual shot, $\tilde{n}_1(x')$ and $\tilde{n}_2(x')$ are obtained. Then these are added up to get the total density $\tilde{n}_{tot}(x') = \tilde{n}_1(x') + \tilde{n}_2(x')$. The resulted density profile is fitted with a zero-temperature Thomas-Fermi profile to extract the effective Fermi width, σ_{Fx}, and center, c_{Fx}, of the cloud. With this information, the density profiles for each

spin state are normalized as:

$$n_\sigma(x') = \frac{\tilde{n}_\sigma(x')}{\tilde{n}_{tot}(c_{Fx})}.$$

Then the axial direction is scaled by dividing the Thomas Fermi width σ_{Fx}, so that it's convenient to perform Abel Inversion later:

$$\frac{x}{\sigma_{Fx}} = \frac{x' - c_{Fx}}{\sigma_{Fx}}.$$

As the density distribution has cutoff at $|x| = \sigma_{Fx}$, the spatial information is all contained in a region that $x/\sigma_{Fx} \in [-1, 1]$. The typical number for σ_{Fx} is 340 μm for a cloud with 65 000 atoms in the experiments reported in this dissertation.

Since the sample is supposed to be symmetric over the center of cloud, I fold each axial spatial profile over $x/\sigma_{Fx} = 0$ and obtain the profile for only $x/\sigma_{Fx} \in [0, 1]$. Because of the finite resolution of CCD cameras, I perform equal-width binning to the dimensionless spin profiles obtained above, yielding 50 bins in total.

A.2 Optional preprocessing

By observing spatial profiles generated from a single-shot data, I found that some data have artifacts such as spatial asymmetry (as shown in Fig. A.1) and spin imbalance. The asymmetry problem is most likely a result of magnetic field sweep. Recall that the magnetic field is tuned from 1200 G to $\sim$ 528 G after spin elimination. Since the curvature of magnetic bowl changes with the magnitude of the field, the cloud is pushed slightly during this field sweeping. In an isolated experimental system, this initial force on the sample has no way to be damped and it drives the atoms in two spin states to oscillate differently at very low frequencies. The spin imbalance is mostly because of the fluctuation of magnetic field, and therefore, the RF pulses are slightly off resonance yielding imperfect $(\frac{\pi}{2})_y$ pulses.

In the data analysis for unperturbed quantum rewinding experiments, before processing data with the procedure introduced in last section, the raw profiles are preprocessed to avoid systematic error. In this section, I describe the procedures for fixing the asymmetry (Sec. A.2.1) and spin-imbalance (Sec. A.2.2) problem during data analysis.

A.2.1 Asymmetric profile correction

In principle, samples prepared in this system introduced in Sec. 4.1 should be symmetrical as shown in Fig. A.1 (a). However, sometimes asymmetrical profiles in (b) are observed. Blue circles and grey circles are unormalized density profiles of two spin states, and the orange circles are the sum of them. The red curve is zero-temperature Thomas Fermi profile fitted to the total density of the cloud. The peak of it marks the center of the cloud, c_{Fx}, pointed out as a red vertical line. In this figure, everything is raw data shown in natural units, nothing is scaled yet.

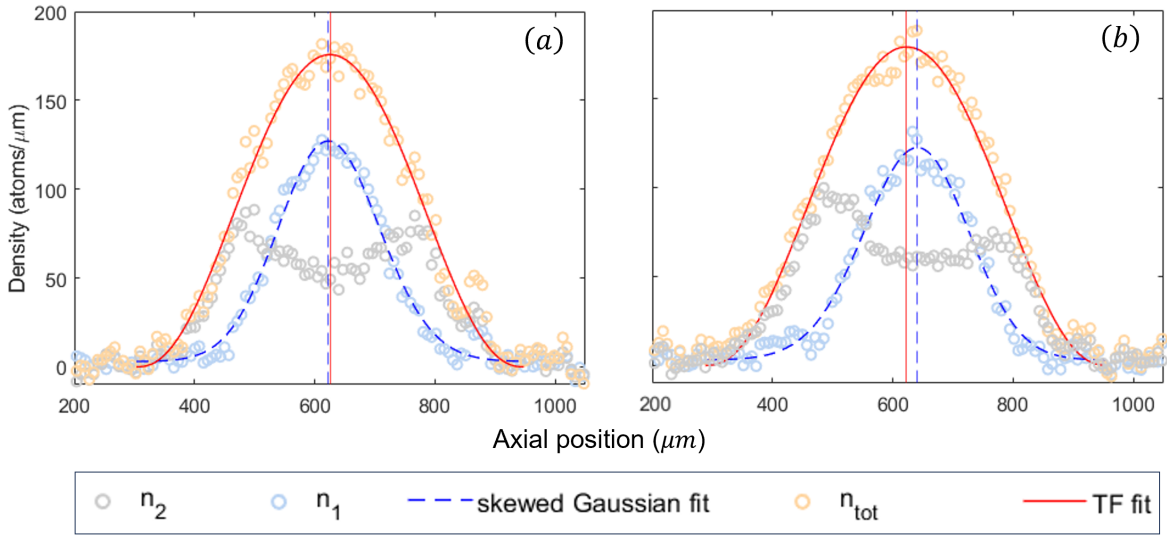

Figure A.1: Examples of a symmetrical sample (a) and an asymmetrical sample (b) from spin segregation experiment described in Ch 2. Grey circles are profiles for spin 2, blue circles are for spin 1, and orange ones are the total density. Blue dashed curves are skewed Gaussian Eq. A.1 fitting results, and red curves are zero-temperature Thomas Fermi profiles fitted to the total density. Red vertical lines point out the center of the cloud by doing TF fit, and the blue dashed vertical lines go through the peak value of fitted skewed Gaussian function. Fit result yields $\alpha \approx 0.85$, $\xi = 66.60 \mu m$ as described in the main text.

In panel (b), spin 2 profile shows an obvious asymmetry comparing to the good data plotted in (a). It is found that the profiles of two spins are usually skewed instead of shifted spatially, and skewed Gaussian function is close to the nominal shape of n_1 profile. Although the skewing in spin 1 profile is not as pronounced as it in spin 2, it can be quantified with function fitting method.

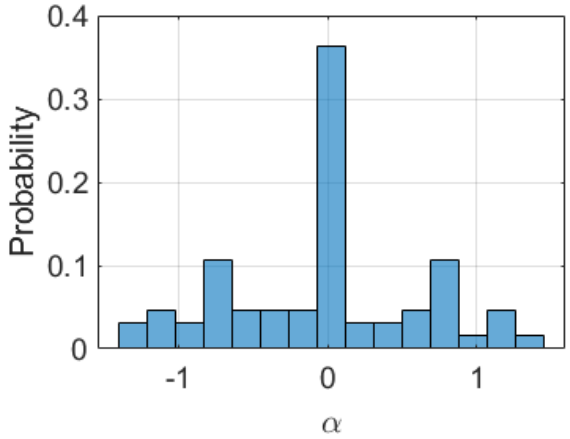

Figure A.2: Distribution of fitted α for a typical dataset.

A particular case of a general class of probability density function (PDF) $\phi(\cdot)$ is a standard Gaussian probability density function, which has the form:

$$\phi(x) = \frac{1}{\sqrt{2\pi}} e^{-\frac{x^2}{2}},$$

and its cumulative density function (CDF) is:

$$\begin{aligned}\Phi(x) &= \int_{-\infty}^{x} dt\, \phi(t) \\ &= \frac{1}{2}\left[1 + erf\left(\frac{x}{\sqrt{2}}\right)\right],\end{aligned}$$

where $erf(x)$ denotes the Gaussian error function. The skewed sPDF has the form $f(x) = 2\phi(x)\Phi(\alpha x)$. Add a shift in x and width ω: $x \to \frac{x-\xi}{\omega}$, then the skewed PDF has the form:

$$\begin{aligned} f(x) &= \frac{2}{\omega}\phi\left(\frac{x-\xi}{\omega}\right)\Phi\left(\alpha\frac{x-\xi}{\omega}\right) \\ \Rightarrow \qquad &= \frac{1}{\omega\sqrt{2\pi}} e^{\frac{1}{2}\left(\frac{x-\xi}{\omega}\right)^2}\left[1 + erf\left(\frac{\alpha}{\sqrt{2}}\frac{x-\xi}{\omega}\right)\right]. \end{aligned} \tag{A.1}$$

Fitting Eq. A.1 to $\tilde{n}_1$ gives us the blue dashed curve in Fig. A.1, and the location of its peak value is labeled with a vertical blue dashed line. By fitting the skewed sPDF, the absolute value of fitted parameter $|\alpha|$ labels the skewness of density profile of spin 1. Larger absolute value

means spin 1 profile is more skewed, negative α means it's shifted to the left and positive α means it's shifted to the right. For the data shown in this dissertation, typical absolute value for α is, of course, zero. However, for the asymmetric results like Fig. A.1 (b), $\alpha \approx 0.85$, $\xi = 66.60\,\mu m$. Fig. A.2 shows a typical distribution of fitted values of α. It suggests that most data are not noticeably asymmetric.

Another feature obtained from the fitting is the peak position of $\tilde{n}_1$, ξ. Comparing this position to the center of the cloud, c_{Fx}, one can find that, for $\alpha < 0$, $\xi < c_{Fx}$ and for $\alpha > 0$, $\xi > c_{Fx}$. Define the difference between the locations of the peaks for the total density and spin 1 density to be $\epsilon = \xi - c_{Fx}$, so that the center of mass for spin 2 is at $c_{Fx} - \epsilon$. Now with the center of mass and skewness for both spins, I plug them into the inverse error function and use the CDF again to skew two spins back to their PDF form such that each profile is symmetric over c_{Fx}.

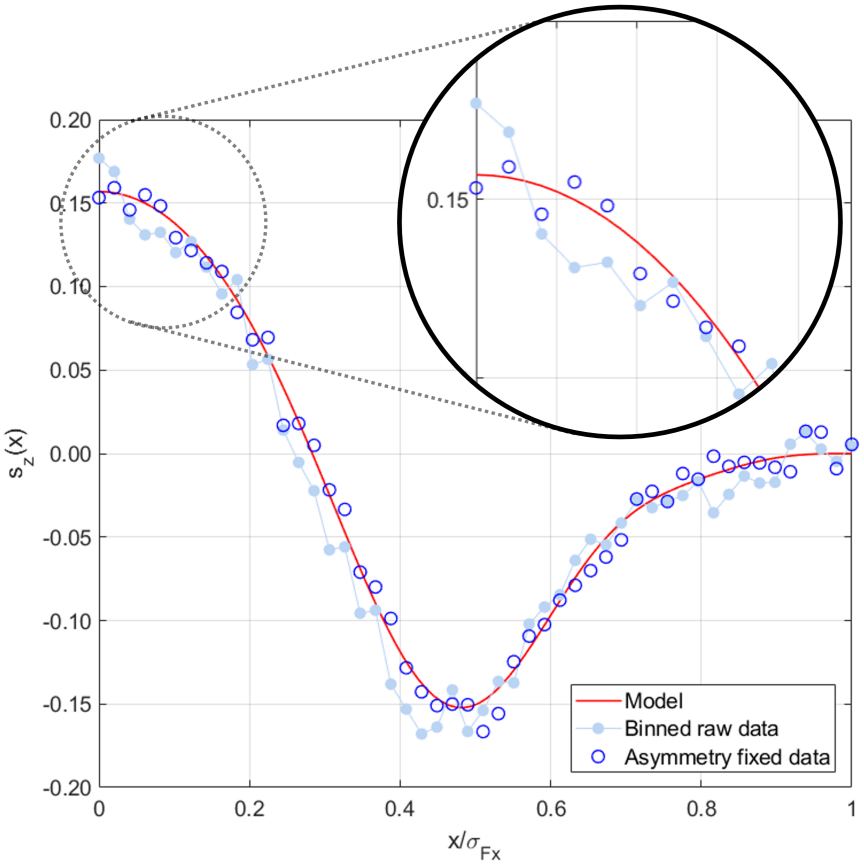

Figure A.3: Comparing $s_z(x)$ profile before (solid light blue dots) and after (bright blue circles) fixing the asymmetry using the method introduced in this section. Red curve is generated by the mean-field model using single-shot experimental parameters σ_{Fx} and N.

Fig. A.3 shows spin density profiles, $s_z(x) = (n_1(x) - n_2(x))/2$, before and after fixing the asymmetry problem. Solid light blue dots connected by lines are $s_z(x)$ obtained from simply folding and binning raw data, and bright blue circles are obtained by preprocessing using the method introduced in this section before regular folding and binning procedures. Red curve is predicted by the model using this single shot experimental parameters.

The asymmetry fixing procedure mainly improves the data quality at the center of the cloud, the circled area in Fig. A.3, where the structures are important for the purpose of studying central spin density evolution. Zooming into this area, it is obvious that the unfixed data shows a spike that is not predicted by the model. This is an artifact results in folding an asymmetric spatial profile. In contrast, the preprocessed data is rather smooth and fits the model better.

As shown in this figure, the asymmetry fixing method does not change the general features of the profile, it only reduces the effect of minor defects from the asymmetric cloud. However, for the spatial profiles with more complicated structures like shown in Ch. 6 and Ch. 7, this method is not applicable since it's not trivial to find a fitting sPDF for complex profiles, hence the skewness α cannot be found precisely in this case.

A.2.2 Spin-imbalance correction

While processing data, some obvious signs of undesired spin imbalance are observed. In the experiments with longer experimental cycles or larger magnetic field sweepings, there is a higher possibility that one or more of the RF pulses are slightly off resonance due to magnetic field changes, since the RF frequency is fixed for all pulses, but the magnetic field can fluctuate because of the limitation on the stability of auxiliary coils. Imperfect RF pulses result in spin imbalance.

For the Hamiltonian reversal (Ch. 5) experiments, where the system is not perturbed and z-component of the spin vector is observed, the total spin vector $S_z = 0$ is known. If the data suggests otherwise, it's because of the imperfect RF pulses. Therefore, for these two experiments, a manipulation to fix the spin-imbalance is reasonable, since the source of the defect is known.

Before trying to fix data, first I examine the degree of spin imbalance by calculating N_1/N_{tot} and N_2/N_{tot}. Ideally, these two numbers should be 50 %. However, In the experiment, these ratios fluctuate from 44 to 56 %. To balance them, I take asymmetry corrected, folded, and binned spatial profiles for each spin: $n_1(x)$ and $n_2(x)$, containing 50 data points in each profile, and then perform trapezoidal numerical integration to each of them, yielding estimated atom number for each spin N_1' and N_2'. Since in this interacting regime, the sum of spatial profiles for two spin states, $n_{tot}(x) = n_1(x) + n_2(x)$, is invariant during the experimental cycle, I simply

add equal and opposite offsets to the profiles:

$$n_1(x) \rightarrow n_1(x) - \delta\, n_{tot}$$
$$n_2(x) \rightarrow n_2(x) + \delta\, n_{tot},$$

where δ is calculated by numerical integrated N_1' and N_2':

$$\delta \equiv \frac{N_1'}{N_1' + N_2'} - \frac{1}{2} = \frac{1}{2} - \frac{N_2'}{N_1' + N_2'}. \tag{A.2}$$

This way, the total atom number and density profile remain the same before and after the adjustment.

Fig. A.4 is an example showing the difference between the spin density profiles before and after enforcing the spin balance. This data is an example from the quantum rewinding experiment at $5\,a_0$. Hamiltonian is reversed at $\tau_f = 400$ ms, and this shot is imaged at forward evolution time $t_f = 0$ ms while the corresponding reversed data total evolution time $t_b = 800$ ms, which means two spins should have identical profiles. Red circle is forward evolution data and blue circle is the corresponding backward evolution data. (a) shows the binned raw data, and (b) shows spin balance enforced data. In this example, the forward evolution data doesn't show spin imbalance, which means that the coherent excitation RF pulse is on resonance, and right after it, two spins have the same atom number. In contrast, in the backward evolution data in (a), the profile curves down below x axis and never comes above it, clearly, in this case, $S_z \neq 0$, which is a sign of spin imbalance. (b) shows the $s_z(x)$ profile after enforcing spin balance, giving $S_z = 0$.

In the perturbed quantum rewinding experiments, it is also observed that different spin imbalances in the model and data exist (although I don't manipulate data to fix it). In Fig. A.5, the regular model (red curves) assumes perfect stable magnetic fields, which means all RF pulses applied are on resonance perfectly. It is clear that the model still captures the shape and oscillation frequency of the data (blue dots) with an offset.

To include the different spin imbalance in the model, the predicted density profiles for the two spin states are adjusted the same way as described above, but with δ as fitted number instead of using the definition in Eq. A.2. Namely, take the outcome $n_{1,m}(x)$ and $n_{2,m}(x)$ from the model and scale them to $n_{1,m}(x) - \delta\, n_{tot,m}$ and $n_{2,m}(x) + \delta\, n_{tot,m}$, where $n_{tot,n}$ is a Thomas Fermi spatial profile. With this adjustment to the outcome of the regular model, the green curves in Fig. A.5 are obtained and fit the data much better.

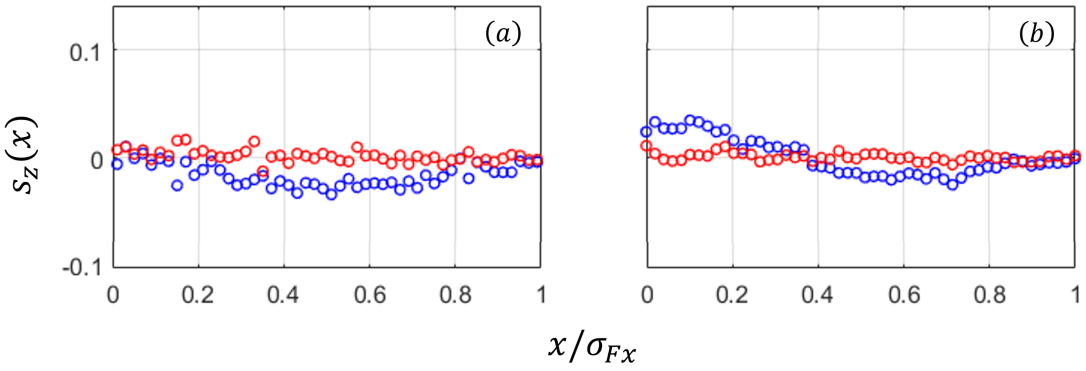

Figure A.4: Comparing spin density profile $s_z(x)$ (a) before and (b) after enforcing spin balance. This data is from quantum rewinding experiments done at $5\,a_0$ and reversal time $\tau_f = 400$ ms. This piece is imaged at forward evolution time $t_f = 0$ ms (reversed data total evolution time $t_b = \tau_f + \tau_f - t_f = 800$ ms), showing forward evolution data (red circles) and corresponding backward evolution data (blue circles).

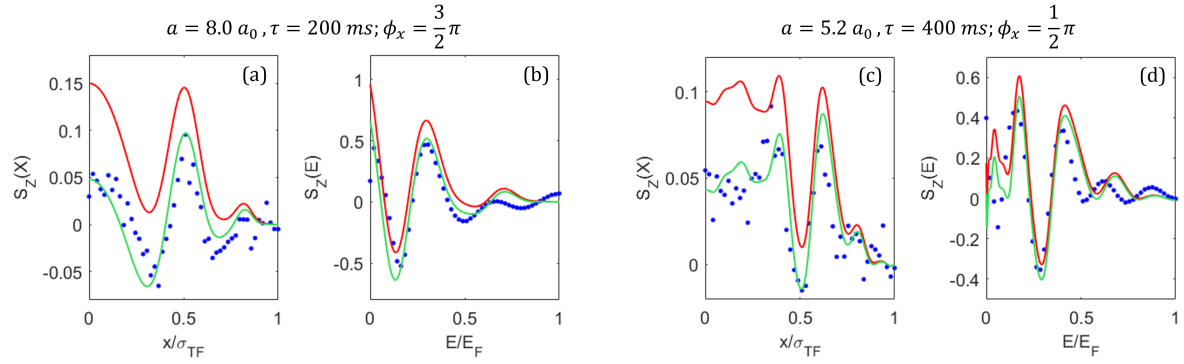

Figure A.5: Adjusting atom number ratio for two spin states in the model results in much better agreement with data. In (a)(c), blue dots are measured single-shot spin density $S_z(x)$ with 8.0 a_0, $\tau = 200$ ms, $\phi_x = 3\pi/2$ and 5.2 a_0, $\tau = 400$ ms, $\phi_x = \pi/2$ respectively, and red curves are generated by the model assuming the perfectly stable B-field. In this case, all RF pulses are on resonance. The green curves are after tweaking the spin imbalance of two spin states by changing the N_1 and N_2 determined from the initial uncorrected model, shown by the red curves, to $N_1 - \delta N_{tot}$ and $N_2 + \delta N_{tot}$. $\delta = 10\%$ for (a) and $\delta = 5\%$ for (c). (b)(d) are Abel inversion of (a)(c) with 12 cosine terms, and color coding is kept consistent with (a)(c).

APPENDIX

B

ABEL INVERSION

In this appendix, I will introduce a numerical solution of Abel-type integral equations using an improved method that was first presented in 1991 (Pretzier 1991). This method is applied to extract energy space spin densities from spatial profiles measured in the experiments presented in this dissertation. This Abel inversion solution is obtained by expanding the energy integral in a series of cosine functions whose amplitudes are calculated by least-squares-fitting from the measured spatial data. The number of expansion terms is determined by the complexity of the data. In this dissertation, I use 8-12 expansion terms to analyze data from spin segregation experiments (Ch. 4), unperturbed quantum rewinding experiments (Ch. 5), and correlation measurement for z-component of spin vector (Sec. 7.1). I use 14-20 expansion terms to analyze data from perturbed quantum rewinding (Ch. 6) and correlation measurements for transverse component of spin vector (most Ch. 7)

B.1 Formalism

Abel inversion is an optimum way to evaluate the energy distribution of a given spatial profile along the longitudinal axis, although it was first designed for the extraction of a distribution in the radial direction from a measurement of distribution in the axial direction. The Abel

transform has the form

$$h(y)=2\int_y^R f(r)\frac{r\,dr}{\sqrt{r^2-y^2}}, \tag{B.1}$$

where $h(y)$ is a measured physical quantity and $f(r)$ is an unknown function. To evaluate $f(r)$, it is expanded into n_{max} cosine terms (Pretzier 1991):

$$f(r)=\sum_{n=0}^{n_{max}} A_n f_n(r), \tag{B.2}$$

$$f_n(r)=\begin{cases} 0 & \text{, for } n=0; \\ 1-(-1)^n\cos\left(n\pi\frac{r}{R}\right) & \text{, otherwise.} \end{cases} \tag{B.3}$$

Using Eq. B.1 and Abel transform of Eq. B.2, define $H(y)$ as a summation of n_{max} terms:

$$\begin{aligned} H(y)&=2\sum_{n=0}^{n_{max}} A_n\int_y^R f_n(r)\frac{r\,dr}{\sqrt{r^2-y^2}} \\ &=2\sum_{n=0}^{n_{max}} A_n h_n(y) \end{aligned} \tag{B.4}$$

where y is the independent variable.

Assume that in each measurement, there are k_{max} values of y_k in total, forming set Y. Therefore, the corresponding measured value $d_k=h(y_k)$ has k_{max} values, too, forming set D:

$$\begin{aligned} h|_Y : Y\rightarrow D; \qquad & d_k\in D:\{k\in\mathbb{N}_1 :\, k\le k_{max}\} \\ & y_k\in Y:\{k\in\mathbb{N}_1 :\, k\le k_{max}\}. \end{aligned} \tag{B.5}$$

In this dissertation, the independent variable x for the spatial profile $s^{meas}(x)$ is scaled by the size of the cloud σ_{Fx} for each shot such that $x_k/\sigma_{Fx}\in[-1,1]$. Then the raw measured axial spatial profile $s^{meas}(x)$ is folded over the center of cloud where $x_k=0$, and binned into 50 points. After this process, $x_k/\sigma_{Fx}\in[0,1]$. It's convenient to use: $y_k\rightarrow x_k/\sigma_{Fx}$, thus $y_k\in[0,1]$ and $k_{max}=50$.

With this measurement, calculate the squared difference between expansion $H(y)$ and

measured $h(y)$:

$$\begin{aligned}\chi^2 &= \sum_k [h(y_k) - H(y_k)]^2 \\ &= \sum_k \left[d_k - \sum_{n=0}^{n_{max}} A_n h_{n,k} \right]^2\end{aligned}$$

and minimize it by $\frac{\partial \chi^2}{\partial A_n} = 0$

$$2 \sum_k \left[d_k - \sum_{n=0}^{n_{max}} A_n h_{n,k} \right] h_{m,k} = 0 \tag{B.6}$$

$$\underbrace{\sum_k d_k h_{m,k}}_{\equiv V_m} = \underbrace{\sum_n \sum_k h_{n,k} h_{m,k}}_{\equiv M_{mn}} A_n \tag{B.7}$$

$$\Rightarrow \qquad A_n = (M^{-1})_{nm} V_m. \tag{B.8}$$

With the values of coefficients A_n optimized, the expansion $H(y)$ will have a numerical form.

B.2 Real space and energy space

To apply the Abel inversion to obtain energy profile from spatial one, the correspondence between them needs to be understood. In this section, I will illustrate how to achieve the form shown in Eq. B.1 with correct dimensions.

Atom density in real space and energy space is connected by the density probability function:

$$n_\sigma(x) = \frac{1}{\pi} \int dE \, |\phi_E(x)|^2 \, n_\sigma(E). \tag{B.9}$$

A WKB approximation is applied to evaluate $|\phi_E(x)|^2$:

$$|\phi_E(x)|^2 \approx \frac{\Theta\left[\frac{2E}{m\omega_x^2} - x^2\right]}{\pi \sqrt{\frac{2E}{m\omega_x^2} - x^2}},$$

$$\Rightarrow n_\sigma(x) = \frac{1}{\pi} \int_{\frac{m\omega_x^2 x^2}{2}}^{E_F} \frac{dE \, n_\sigma(E)}{\sqrt{\frac{2E}{m\omega_x^2} - x^2}},$$

where $E_F = \frac{1}{2} m \omega_x^2 \sigma_{Fx}^2$ is the effective Fermi energy, and the cutoff σ_{Fx} is obtained by fitting a zero temperature Thomas Fermi profile to the spatial density of the sample.

For convenience, the variables are converted to dimensionless forms:

$$\tilde{E} \equiv \frac{E}{E_F}, \qquad d\tilde{E} = \frac{dE}{E_F}.$$

Then the upper and lower limits of the integral become:

$$\begin{cases} \text{upper limit} & \to 1 \\ \text{lower limit} & \to \frac{m\omega_x^2 x^2}{2}/E_F = \frac{x^2}{\sigma_{Fx}^2}. \end{cases} \tag{B.10}$$

$$\Rightarrow n_\sigma(x) = \frac{1}{\pi}\int_{x^2/\sigma_{Fx}^2}^{1} \frac{d\tilde{E}\, n_\sigma(\tilde{E})}{\sigma_{Fx}\sqrt{\tilde{E} - \frac{x^2}{\sigma_{Fx}^2}}}. \tag{B.11}$$

Now the spatial variable is changed to its dimensionless version:

$$\tilde{X} \equiv \frac{x}{\sigma_{Fx}}$$

$$\Rightarrow n_\sigma(\tilde{X}) = \frac{1}{\pi\sigma_{Fx}}\int_{\tilde{X}^2}^{1} \frac{d\tilde{E}\, n_\sigma(\tilde{E})}{\sqrt{\tilde{E} - \tilde{X}^2}}. \tag{B.12}$$

Eq. B.12 has the same form as Eq. B.1 by writting

$$\frac{r}{R} \to \sqrt{\tilde{E}},$$

and the expansion terms in Eq. B.3 has the form:

$$f_n(\sqrt{\tilde{E}}) = \begin{cases} 0 & \text{, for } n = 0; \\ 1 - (-1)^n \cos\left(n\pi\sqrt{\tilde{E}}\right) & \text{, otherwise.} \end{cases} \tag{B.13}$$

$h_n(y)$ in Eq. B.4 becomes:

$$h_n(\tilde{X}) = \frac{1}{\sigma_{Fx}}\int_{\tilde{X}^2}^{1} \frac{d\tilde{E}}{\sqrt{\tilde{E} - \tilde{X}^2}} f_n(\sqrt{\tilde{E}}). \tag{B.14}$$

Performing least-squares-fitting, as introduced in Eq. B.6, with data $d_k = n_\sigma(\tilde{X}_k)$ and Eq. B.14, will yield a numerical form of $n_\sigma(\tilde{E})$. In this way, the spin density in energy space is obtained.

B.3 Energy resolution

The imaging system in our lab has a spatial resolution $\delta x \approx 5\mu$m. This results in a finite resolution in energy space, δE_s. Since the energy is related to the spatial position,

$$E = \frac{1}{2} m\omega_x^2 x^2,$$

the resolution in energy space can be estimated by:

$$\delta E_s \approx \delta(\frac{1}{2} m\omega_x^2 x^2) = \frac{2x\delta x}{\sigma_x^2} E_F \approx 0.03\, E_F \sqrt{\tilde{E}}\,, \tag{B.15}$$

since x^2/σ_{Fx} scales as $\sqrt{E_i/E_F}$.

Furthermore, $n_\sigma(\tilde{E})$ has a finite resolution in energy space, δE_A, which is related to the maximum number of terms, n_{max}, adopted in the Abel inversion. From Eq. B.13, the n^{th} $(n>0)$ expansion term can be written as

$$f_n(\sqrt{\tilde{E}}) = 1-(-1)^n \cos\phi_n'(\sqrt{\tilde{E}}),$$

where $\phi_n'(\sqrt{\tilde{E}}) \equiv n\pi\sqrt{\tilde{E}}$. Then the resolution δE_A can be estimated by setting

$$\begin{aligned} 1 &\simeq \delta E_A \frac{\partial \phi_n'(\sqrt{\tilde{E}})}{\partial E}\bigg|_{n=n_{max}} \\ 1 &= \delta E_A \frac{\partial (n_{max}\pi\sqrt{E_i/E_F})}{\partial E_i} \\ \Rightarrow \delta E_A &= \frac{2}{n_{max}\pi}\sqrt{\frac{E_i}{E_F}} E_F. \end{aligned} \tag{B.16}$$

In the data analysis, $n_{max} = 12$ is applied to most of the data, yielding $\delta E_A \approx 0.06\, E_F \sqrt{\tilde{E}}$.